



Norwegian University of
Science and Technology

Detailed Study of LED Diffuse Back Illumination for Soot Measurements in an Optical Combustion Chamber

Mathias Solberg Olsen

Natural Gas Technology

Submission date: June 2017

Supervisor: Terese Løvås, EPT

Co-supervisor: Karl Oskar Pires Bjørgen, EPT
David Emberson, EPT

Norwegian University of Science and Technology
Department of Energy and Process Engineering

EPT-M-2017-63

MASTER THESISfor
Student Mathias Solberg Olsen
Spring 2017**Detailed study of LED diffuse back illumination for soot measurements in an optical combustion chamber.****Background and objective**

In order to meet recent legislation requirements for increased use of renewable biofuels in transportation, it is essential to ensure the safe and efficient operation of such fuels in the current and future fleet of compression ignition (CI) vehicles. Concerns have been raised on issues related to both operational problems and emissions. The experimental CI engine suite at The Department of Energy and Process Engineering is designed to provide this insight. The suite consist of three separate experimental rigs examining combustion and injection in CI engines.

The optical combustion chamber is currently in its installation and testing phase. One key element of this rig is a novel, L.E.D. illumination and high speed imaging system that will be used for light extinction experiments to determine soot volume fraction in the chamber during combustion. A first phase was completed during the Project thesis work and successful imaging of soot was performed using a Bunsen burner located in the chamber volume. In the following Masters project, the combustion chamber will be fully assembled with injection system and piston compression. The system requires extensive testing and completion. Testing needs to be conducted applying a variety of techniques to qualitatively and if possible quantitatively determine the suitability of the system to soot measurements and produce a suitable experimental protocol and post processing procedure.

The following tasks are to be considered:

- 1 Literature review of compression ignition engine, soot production and soot measurement, as well as optical measurement techniques, particularly using back lit illumination.**
- 2 Install the LED imaging system including carefully chosen optical devices for to examine beam-steering. Collect image sequences for verification of set-up.**
- 3 Post process image sequences of collected data to extract data for different set-ups. Draw conclusions about the system's ability to image soot and suggest protocol.**

-- ” --

Within 14 days of receiving the written text on the master thesis, the candidate shall submit a research plan for his project to the department.

When the thesis is evaluated, emphasis is put on processing of the results, and that they are presented in tabular and/or graphic form in a clear manner, and that they are analyzed carefully. The thesis should be formulated as a research report with summary both in English and Norwegian, conclusion, literature references, table of contents etc. During the preparation of the text, the candidate should make an effort to produce a well-structured and easily readable report. In order to ease the evaluation of the thesis, it is important that the cross-references are correct. In the making of the report, strong emphasis should be placed on both a thorough discussion of the results and an orderly presentation. The candidate is requested to initiate and keep close contact with his/her academic supervisor(s) throughout the working period. The candidate must follow the rules and regulations of NTNU as well as passive directions given by the Department of Energy and Process Engineering.

Risk assessment of the candidate's work shall be carried out according to the department's procedures. The risk assessment must be documented and included as part of the final report. Events related to the candidate's work adversely affecting the health, safety or security, must be documented and included as part of the final report. If the documentation on risk assessment represents a large number of pages, the full version is to be submitted electronically to the supervisor and an excerpt is included in the report. Pursuant to “Regulations concerning the supplementary provisions to the technology study program/Master of Science” at NTNU §20, the Department reserves the permission to utilize all the results and data for teaching and research purposes as well as in future publications.

The final report is to be submitted digitally in DAIM. An executive summary of the thesis including title, student's name, supervisor's name, year, department name, and NTNU's logo and name, shall be submitted to the department as a separate pdf file. Based on an agreement with the supervisor, the final report and other material and documents may be given to the supervisor in digital format.

- Work to be done in lab (Water power lab, Fluids engineering lab, Thermal engineering lab)
 Field work

Department of Energy and Process Engineering, 15. January 2017



Terese Løvås
Academic Supervisor

Research Advisor: David Emberson and Karl Oskar Pires Bjørgen

Abstract

An optical accessible compression ignition engine is under development at the engine suite at EPT, NTNU. The purpose of the new optical engine is to measure soot formation during the combustion process. In the search of alternative fuels for compression ignition engines, understanding and quantifying soot formation is an essential factor. The current simulation models available for soot formation are lacking in accuracy, especially for now high quality experimental data is still required quantify and properly understand soot formation from alternative fuels.

In this project, the goal is to test and investigate the rig and the optical systems ability to detect soot. The soot detection system consists of a high-speed camera and a light source used in a diffused, back-illumination, extinction imaging configuration. In this thesis, a preliminary experiment for soot detection is presented. Together with extensive testing of the engine as a part of the development and finalization of the optical engine rig. To process and analysis images and various sensor data, several MATLAB scripts are purpose written. From the various experiments, settings are suggested to optimize the accuracy of the soot detection method.

From the primary soot detection experiment, the KL factor from a soot rich propane flame can be predicted with an uncertainty of $\pm 4.1\%$ at 2σ confidence interval. With a new optical configuration, the uncertainty in KL factor can possible be further reduced as the conditions for light distortion is reduced. The preliminary soot detection test with a steady state flame shows that the system's ability to detect soot is better or comparable to similar experimental systems.

Sammendrag

Ved motorlaboratoriet på instituttet for energi og prosesseteknikk på NTNU er en dieselmotor med optisk tilgjengelig forbrenningskammer under utvikling. Hensikten med denne motorriggen er å måle sot-formasjon gjennom forbrenningsprosessen. I jakten på alternativ miljøvennlig drivstoff for dieselmotorer er det essensielt å forstå samt kvantifisere sotutslippene. De matematiske metodene tilgjengelige i dag for å beregne sot-formasjon i slike prosesser er ikke på et tilfredsstillende nivå, derfor er eksperimentell data av høy kvalitet svært verdifullt.

I dette prosjektet er målet å utføre tester for å undersøke systemets evne til å detektere sot og operasjonsforhold. Det optiske målesystemet for sot-deteksjon består av et høyhastighetskamera og en kraftig lyskilde, satt i konfigurasjon for å danne, diffuse bakgrunns-belyste eliminasjons bilder. For å analysere høyhastighetsbildene og annen sensor data er flere MATLAB skript skrevet. Gjennom flere runder med eksperimenter er målet å finne en tilnærming til de innstillingene og den optiske konfigurasjonen som gir de beste forholdene for sot-deteksjon i den optiske motoren.

Fra en innledende sot-deteksjonstest med foreslåtte innstillinger viser innsamlet data av en sot rik propanflamme at KL faktoren i flammen har en usikkerhet på $\pm 4.1\%$ ved 2σ konfidensintervall. (KL faktoren kan brukes direkte videre for å beregne mengden sot.) Sammenliknet med data fra andre eksperimenter der tilsvarende målemetode brukes viser de innledende eksperimentene at usikkerheten i KL faktoren fra dette systemet er bedre eller tilsvarende liknende systemer.

Contents

Introduction.....	1
Objectives	2
Chapter 1 Theory	3
1.1 Emissions and Soot Formation in Diesel Engines	3
1.1.1 Combustion Modes and Flames Types	4
1.1.2 Combustion Modes and Flames Types	7
1.1.3 Flame Propagation in a CI Engine	8
1.1.4 Pollutants from Diesel Engines.....	9
1.2 Soot Formation Fundamentals	11
1.2.1 Pyrolysis.....	11
1.2.2 Nucleation	12
1.2.3 Surface Growth	12
1.2.4 Coalescence and Agglomeration.....	12
1.2.5 Oxidation.....	12
1.3 The Optical Engine at EPT	13
1.3.1 In Cylinder Soot Detection	15
1.3 Light Propagation Through Inhomogeneous Media	18
1.3.1 Background.....	18
1.3.2 Diffused Light vs Collimated Light	23
1.3.3 Collimated and Diffuse Light Sources Interaction with Refractive Objects	24
1.3.4 Light Simulation of Interaction with a Refractive Object	25
Chapter 2 Method	27
2.1 Introduction to Experiments	27
2.2 Optical Method	29
2.3 General Setup.....	33
2.3.1 List of Equipment	33
2.3.2 General Setup.....	34
2.4 Camera	35
2.5 Data Processing.....	38
2.6 Experimental Process.....	40
2.6.1 Experimental approach	40

Chapter 3 Results and Discussion.....	41
3.1 Investigation of LED Stability	41
3.2 Investigate NDF Impact on Light Intensity	43
3.3 Exposure Comparison.....	45
3.3 Flame Illumination at Different Exposure Time.....	47
3.4 KL Map and Signal-to-Noise Ratio	48
3.5 From the Results in 3.1 and 3.2 Suggestion on Procedure and Filter Combination.	51
3.6 Conclusion on Soot Detection Ability	53
Chapter 4 Engine Tests and Thermal Characteristics	54
4.1 Heat Transfer in Perspective.....	54
4.2 Heat Transfer Modes.....	54
4.2.1 Convection	54
4.2.2 Conduction.....	54
4.2.3 Radiation	54
4.2.4 Heat Transfer Process	55
4.3 Heating System in The Engine Rig.....	56
4.4 Temperature Sensors.....	57
4.5 Overview of Engine Testing	58
4.6 Engine Sensor Data Analysis.....	59
4.6.1 Data Analysis Overview	59
4.6.2 Raw Pressure Data	60
4.6.3 Data Adjustment	62
4.6.4 Average Pressure Plot	62
4.6.5 Statistical Analysis of Average Pressure	65
4.7 Analyzed Data Sample.....	66
4.8 Result and Analysis of Window Torque.....	69
4.8.1 Max Window Torque.....	71
4.9 Temperature Characteristics	73
4.9.1 Passive Heating, Time and Settings Need to Reach 200°C.....	73
4.9.2 Engine Cooling	74
4.9.3 Thermal Response Running Engine.....	75
4.10 Analysis and Conclusion of Thermal Characteristics from Engine Testing.....	80

Chapter 5 Light Distortion, IODBIEI and DBIEI.....	81
5.1 Overview.....	81
5.2 Single-Mirror Coincident Shadowgraph.....	82
5.2.1 Setup	82
5.2.2 Alignment Procedure	83
5.3 Shadowgraph Experiment.....	85
5.3.1 Results and Conclusion from Shadowgraph Experiment	86
5.3.2 Image Background.....	86
5.4 Comparative Investigation IODBIEI and DBIEI.....	89
5.4.1 Introduction.....	89
5.4.2 Experimental Setup.....	89
5.5 Results and Discussion IODBIEI vs DBIEI	91
5.5.1 Discussion on Optical Configuration and Light Distortion	94
5.5.2 Further Work.....	95
Chapter 6 Summary and Conclusion of Experiments.....	97
6.1 Optical System for Soot Detection	97
6.2 Engine Characteristics	98
6.3 Light Distortion Experiments	98
Bibliography	99
Appendix A.....	102
Pressure Data Analysis Script.....	102
Soot quantification script	108
Appendix B.....	114
HSE Report	114

List of figures

Figure 1 Visual representation of experimental rigs used to characterize biodiesel in CI engines.	2
Figure 2 Large volume compression ignition engine. pp.33 Heywood [5]	3
Figure 3 Four stroke CI cycle. Figure is found in Heywood pp. 10 [5]	4
Figure 4 Sequence of events in a four-stroke spark ignition engine. Figure is from Heywood pp.18 [5]	5
Figure 5 p-V diagram for a four-stroke engine cycle. Heywood pp. 47	6
Figure 6 Diesel spray flame	7
Figure 7 Equivalence ratio (ϕ) effect on exhaust HC emission ([5], p625)	10
Figure 8 Pollutant formation mechanisms in a direct injection compression ignition engine ([5], p572)	10
Figure 9 Illustration showing the first five stages of soot formation from fuel in gas phase to a solid, A.K. Agarwal et al PP3281 [9]	11
Figure 10 Render of the optical engine rig at EPT from CAD environment	13
Figure 11 2D section view of optical engine	14
Figure 12 Isometric $\frac{3}{4}$ section view of optical engine	14
Figure 13 Isometric section view engine head across the combustion chamber	14
Figure 14 Optical design from Ghandi and Heim. [17]	16
Figure 15 Beam steering illustration from Thomson et al. [22]. In the images, the f_v represents the volume fraction and σ_{f_v} represents the standard deviation in the volume fraction region.	20
Figure 16 The figure shows extinction laser beam spot after passing through the engine. The dotted crosshairs indicate the center position of the beam with no deflection/beam steering.	21
Figure 17 Illustration from Schulz and Gronki [21], upper section of the image shows horizontal sections of varying intensity. In the bottom of the figure are the improved images.	22
Figure 18 Example of parallel and diverging rays.	23
Figure 19 Body with change in refractive index introduced to the parallel and diverging rays.	24
Figure 20 Light interacting with a large sphere with the refractive index of water. Section a) show collimated light and b) shows diffuse light.	25
Figure 21 Light interaction with a large sphere	26
Figure 22 Overview of experiments in the thesis. Three main sections of experiments.	28
Figure 23 Illustration showing how the background image is captured. The computer screen shows what is seen from the camera.	29
Figure 24 Illustration showing how a material can be introduced between the camera and the back-light source.	29
Figure 25 Time resolved KL factor with distance from the injector on the x-axis. Sampled across the center of the flame.	31
Figure 26 Soot volume fraction f_v axially across the flame at a 50mm distance from injector orifice.	32
Figure 27 KL factor from a single flame with dotted blue line. And and the average KL factor from 25 injections	32
Figure 28 Experimental setup.	33
Figure 29 Pixel sensor with a red color filter from an CMOS camera sensor [32].	35

Figure 30 CCD vs CMOS image sensor design [33].	35
Figure 31 Building blocks of images collected by the camera.	37
Figure 32 Extracted example from MATLAB script.	38
Figure 33 Illustration of work flow in MATLAB script.	39
Figure 34 The black graph illustrates average pixel value for each image. The green annotated “series (n)” arrow indicated start and end of an image series.	41
Figure 35 Continuous image series of 10 000 images. Plot show average pixel value over time.	42
Figure 36 Plot showing average pixel value for ND filters.	43
Figure 37 variation for each of the ND filters are given relative to, how many percentage two sigma impacts relative of the average for the image series.	44
Figure 38 LED exposure and light intensity from the LED over time. Signals are adjusted to fit in one illustration sizes are not to a definitive scale.	45
Figure 39 LED exposure and light intensity from the LED over time. It is show how a delay can be added to the output of the camera exposure to maximize the light intensity in the next images. The Signals are adjusted to fit in one illustration sizes are not to a definitive scale.	45
Figure 40 Signal delay sweep. The average pixel value vs image number in a series.	46
Figure 41 Flame impact at different exposure levels.	47
Figure 42, 2-D KL factor map Plotted scale where 0=black and 0.4=white	49
Figure 43 Same as Figure 42, blue bar illustrates how pixel values across the center used in further calculation	49
Figure 44, KL factor from extracted pixel values across the center of Figure 43	50
Figure 45 KL factor from extracted frame across center of image. On the figure section used for calculation of background noise and signal is annotated. The dashed lines illustrate the average value in each section.	50
Figure 46 Temperature profile across combustion chamber, from gas to cooling liquid. Illustration 12.1 from the book "Internal Combustion Engines" by John B. Heywood	55
Figure 47 Illustration radiant flux, radiant temperature, and heat release rate vs crank angle degree for various equivalence ratios.	55
Figure 48 Transparent engine head from CAD environment showing heating elements for pre-heating the head assembly. Heating elements are marked H1-H4.	56
Figure 49 Side view of engine showing the relative position of each temperature sensor on the engine assembly.	57
Figure 50 Zoomed in version of engine head assembly and temperature sensor position	57
Figure 51 Data collection process flow.	59
Figure 52 Data analysis simplified work flow.	60
Figure 53 Raw pressure data plotted in MATLAB with a blue line.	61
Figure 54 Raw pressure data, same as showed in Figure 53 but zoomed in around pressure peaks to illustrate the variation	61
Figure 55 Extracted MATLAB script for adjustment of decreasing average.	62
Figure 56 Illustration showing reference point (IVC) on pressure plots used offset the pressure data on the Y axis.	63
Figure 57 Pressure data after Y axis modification, the data section in this image is the same as shown in Figure 52 section 3. (lower right corner of Figure 52.)	63

Figure 58 Two sigma standard deviation plot. The plot show footprints from the method used for data alignment.....	64
Figure 59 Extracted section of pressure data from the dynamic pressure sensor in the engine chamber.....	65
Figure 60 Statistical analysis of a pressure data. The figure indicates	66
Figure 61 Histogram plot of pressure data, compared to the ideal normal distribution for the same dataset.	67
Figure 62 Quantile-quantile plot pressure data points marked with blue x symbols. The red line illustrated the ideal normal distribution function.....	68
Figure 63 Window retainer torque vs combustion chamber pressure.....	69
Figure 64 Peak pressure value for each window torque	70
Figure 65 Retainer and window in position in the engine head assembly.....	71
Figure 66 Passive engine heater curve. Blue line indicates the temperature sensor located in the combustion chamber wall. Red line the temperature of the far mounted head temperature sensor. The black represents the piston sleeve temperature sensor.	73
Figure 67 Cooling curve for the engine rig. Blue line represents chamber wall temperature, red line indicates far mounted engine temperature sensor, black line indicates cylinder sleeve temperature.	74
Figure 68 Cooling curve the first 20 minutes after heater shutdown.....	75
Figure 69, Temperature response running engine, cold inlet air. The three plots in section A, B and C represent respectively the temperature response from. A cold, B 60°C and C 100°C.....	76
Figure 70 Pressure plot cold run	77
Figure 71 Temperature response running engine test with inlet air heater on.....	78
Figure 72 Pressure plots from runs with air inlet heater on 100degC	79
Figure 73 Test objects for light distortion experiments.....	81
Figure 74 Optical setup for Single-Mirror Coincident Shadowgraph system. Simplified drawing seen from above	82
Figure 75 Light distortion objects. C: Quartz, B: Glass, A: Glass with gradients.....	85
Figure 76 Plain Background image seen in the left section marked with A. The right section marked B annotates the re occurring objects in the image. The yellow (I) mark show a concentration of light in the center of the image. (II) indicates dust spots on the camera lens. (III) is the injector tip in combustion chamber.	86
Figure 77 Object A.....	87
Figure 78 Shadowgraph of object B	87
Figure 79 Object B.....	87
Figure 80	88
Figure 81 Object C in chamber	88
Figure 82 Old IOBIEI setup.....	89
Figure 83 New optical DBIEI setup.....	89
Figure 84 Visual representation of an engineering diffuser. Figure by THORLABS [42]	90
Figure 85 Engineering diffuser layup. Figure from technical product datasheet for “EDC-15-15132” by RPC Photonics, Inc. [39].....	90
Figure 86 Background illumination old DBIEI vs new DBIEI setup.....	92

Figure 87 Pixel values for the old and new setup with glass beaker bottom in the combustion chamber.....	93
Figure 88 Ray diagram for a typical Fresnel lens.	94
Figure 89 Suggested modification to the DBIEI setup.	95
Figure 90 Suggested setup to obtain a diffuse background illumination. The image belongs to Thorlabs Inc, and is found in the documentation for application areas for aspheric condenser lenses [41]......	96
Figure 91 Overview of the three experimental section in this work.....	97

List of Tables

Table 1 Combustion in CI direct injection with a 4-spray injector with counterclockwise swirl. Figure from Heywood PP498 [5]......	8
Table 2 Relationship between pollutants and where they are formed.	9
Table 3 Parameters for the standardized “Spray A” flame classified by ECN.....	17
Table 4 List of equipment.	33
Table 5 Initial Camera settings	36
Table 6 List of experiments. [us] represents microseconds.....	40
Table 7 Average of series values and standard deviation for each series.	41
Table 8 Uncertainty elements in KL factor.....	51
Table 9 Presentation of formulas used for statistical calculations.....	65
Table 10 Summary of engine characteristics shown in prior figures.....	80
Table 11 Equipment list for the setup in Figure 74	82
Table 12 Mirror and LED alignment chart	84
Table 13 Camera settings.....	90
Table 14 Experiment matrix	90
Table 15 Result from light distortion experiments	91

Introduction

For the last centuries, the population on our planet has grown exponentially. The standard of living is on an increasing trend across the globe [1]. With increasing living standard comes an ever-expanding demand of energy. The availability of clean and affordable energy is central to a healthy life. Ideally people across the world should have access to stable renewable energy whenever desired. Unfortunately, this is not the reality yet. Currently we are in a transitional period where most of the world still will be depend on fossil fuels for decades to come.

A possible solution in the transitional period is to utilize existing infrastructure to reduce emissions that negatively impacts our environment. One specific area where existing fuels can be replaced to produce cleaner energy is for Diesel engines. Diesel or compression ignition (CI) engines has for a long time been a popular choice as powertrain in cars, due to its high-energy output and relatively low cost. In more remote location outside the power grid CI engines are commonly used for electric power production.

In the last decade, it has been found that pollutants from CI engines, and especially particulate matter emissions (PM) as soot, has shown far greater impact on health and environment than what was first believed [2] [3]. If existing CI engines are going to be used for decades to come it is important to find a sustainable way to reduce emissions. A possible solution is to substitute the traditional Diesel derived from fossil fuel with second generation biodiesel which can be sourced from biomass and cellulosic based matter [4]. In the CI engine laboratory at department of Energy and Process Engineering at NTNU three purpose built experimental rigs are under development to study the impact of the new generation of biofuel. With the three rigs listed below and seen in Figure 1 the goal is to characterize and study how new classes of biodiesel effect engine performance and emissions.

- The first rig consists of a fully instrumented engine which represents the bulk CI engines in operation Europe. Equipped with advanced exhaust gas analyzers.
- Second rig consist of a fuel injector characterization system to examine fuel sprays for a variety of fuels.
- The third rig is the subject of this project and is currently under development. It consists of a large displacement, one-cylinder optical accessible CI engine. The purpose of this rig

is to quantify soot formation during the combustion process by using a high-speed camera and a custom lighting system.

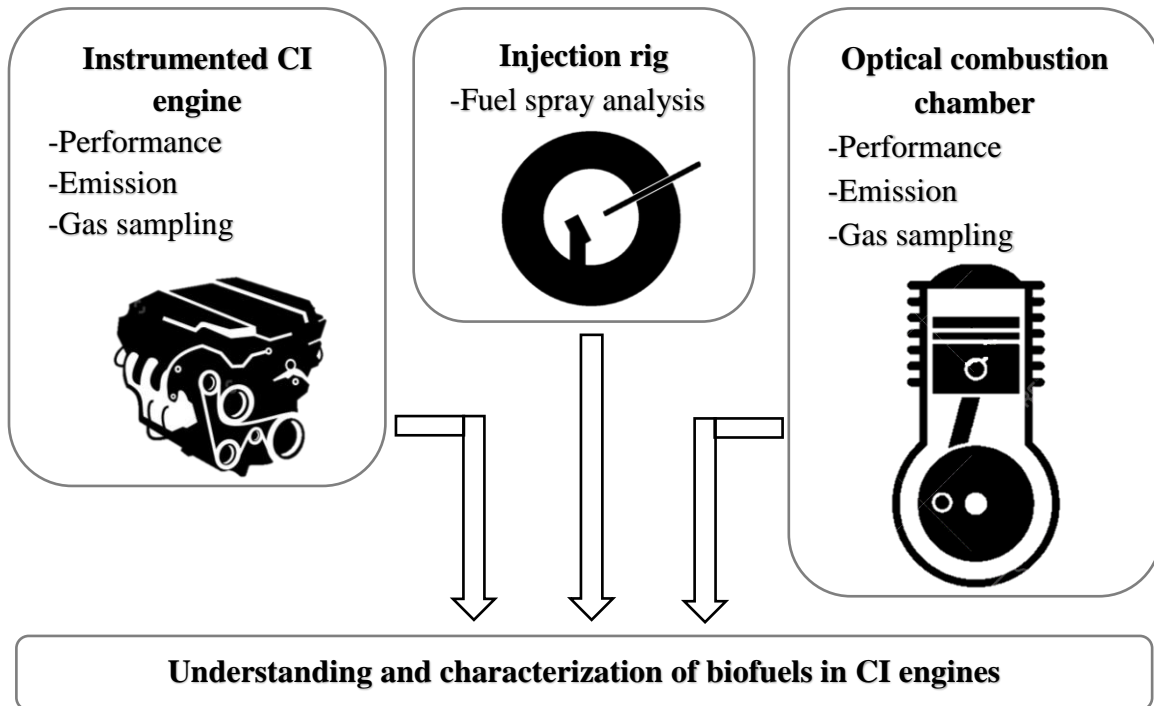


Figure 1 Visual representation of experimental rigs used to characterize biodiesel in CI engines.

Objectives

The purpose of this project is to extensively test, configure, and complete the back-light illumination and camera system that will be used to determine soot volume fraction during combustion. Furthermore, extensive testing on the engine temperature characteristics, and operational conditions for the engine will be investigated. In the first chapters of this thesis relevant theory on CI engines, emissions and the optical techniques used will be covered. The experiments conducted in this thesis is divided into three sections. First a preliminary soot detection study with an external steady state flame will be investigated. In the second section the engine temperature characteristics and pressure behavior is investigated. The third section of experiments investigates a new optical setup to mitigate the conditions for light distortion.

To analyze the data, from the various experiments, MATLAB scripts has been purpose written for each section. The MATLAB scrips are found in the printed and digital appendix

Chapter 1 Theory

1.1 Emissions and Soot Formation in Diesel Engines

The following section is inspired by the book “Internal Combustion Engine Fundamentals” by John B. Heywood [5].

The purpose of the internal combustion engine is to convert chemical energy in fuel to useful mechanical power. The first versions of the first spark ignition engines as we know it today was introduced by Nicholas A. Otto and Eugen Lange in 1867. Three decades later, in 1897 Rudolf Diesel described in a patent, what would become the basis of the modern compression ignition engine. Since their inception both engine types have been continuously improved as they have been used as the main power unit on most modes of transportation up until today. Both engine types have seen massive improvements with regards to efficiency, power, pollution, reliability, and cost. A modern large volume compression ignition engine can be seen in Figure 2. For further reading on the history and development of CI engines readers are advised to read “ *Internal Combustion Engine Fundamentals* ” by John B. Heywood [5].

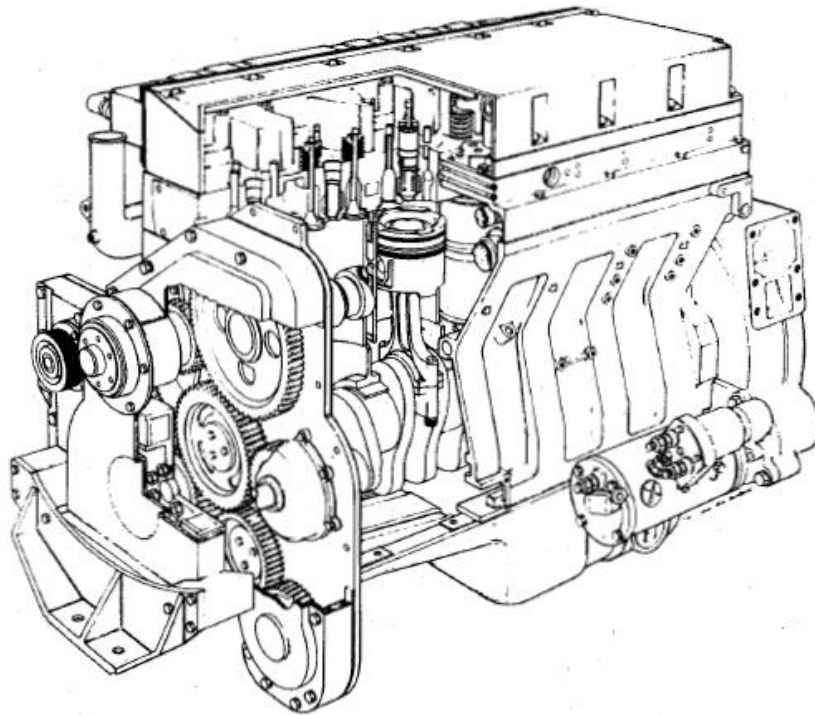


Figure 2 Large volume compression ignition engine. pp.33 Heywood [5]

1.1.1 Combustion Modes and Flames Types

A compression ignition engine is a reciprocating engine, rather than relying on a spark to trigger the combustion event as in spark ignition engine, the CI engine only rely on the compression of the air in the cylinder to produce sufficient temperature for the injected fuel to auto ignite.

The CI engine operates on four strokes for one complete combustion cycle. These four strokes are illustrated in Figure 3. The first stroke is the intake stroke where the inlet valve opens and air is drawn into the engine by the movement of the piston. The second stroke is the compression stroke. The inlet valve closes and the piston reduces the volume of the cylinder and compresses the air. Shortly before the piston reaches its top position fuel is injected into the chamber, the hot air and fuel reacts and combustion starts promptly before the piston reaches its top position. The third stroke is called the expansion stroke and this is where the engine produces energy. As the the expanding gases forces the piston downwards. During the expansion stroke the engine deliver around 5 times more energy than required to compress the air during the compression stroke. In the fourth and last stroke, the exhaust valve is opened as the piston once again approaches top center and the burned gases are pushed out of the cylinder. [5]

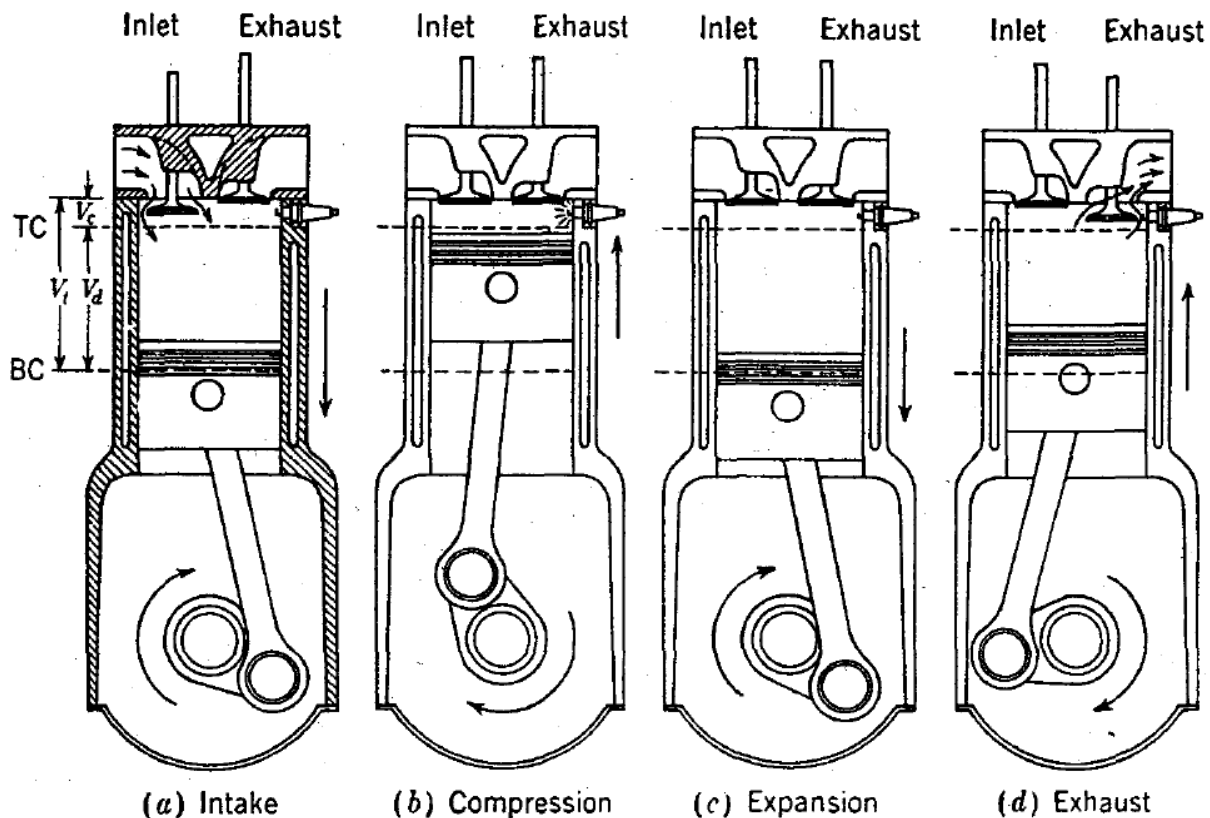


Figure 3 Four stroke CI cycle. Figure is found in Heywood pp. 10 [5]

During the four-stroke cycle in a CI engine the crankshaft rotates two full rotation i.e. 720° . To illustrate the cylinder pressure and the sequence of events that occur during the process Figure 4 shows two plots where the x-axis is the crank angle position from -360° to 360° .

The top section of Figure 4 shows the cylinder pressure and is annotated with the four strokes and where the inlet valves (IV) and exhaust valves (EV) opens (O) and closes (C). It is worth noting that Figure 4 represents a four-stroke cycle for a spark ignition engine and is used for illustration purposes only. Figure 4 is useful to show the cylinder pressure and the valve timing relative to the crank angle. The four-stroke cycle of a CI engine is similar to the process seen in Figure 4 other than the spark annotation can be replaced with fuel injection into the cylinder. The pressure curve in the top portion of Figure 4 has an alternate slope that is dashed, this dashed line represents the cylinder pressure for a motored compression i.e. no combustion.

The bottom portion of figure Figure 4 shows the relative cylinder volume V/V_{\max} and the line x_b that start at the point of combustion illustrates the mass fraction burned in the combustion process.

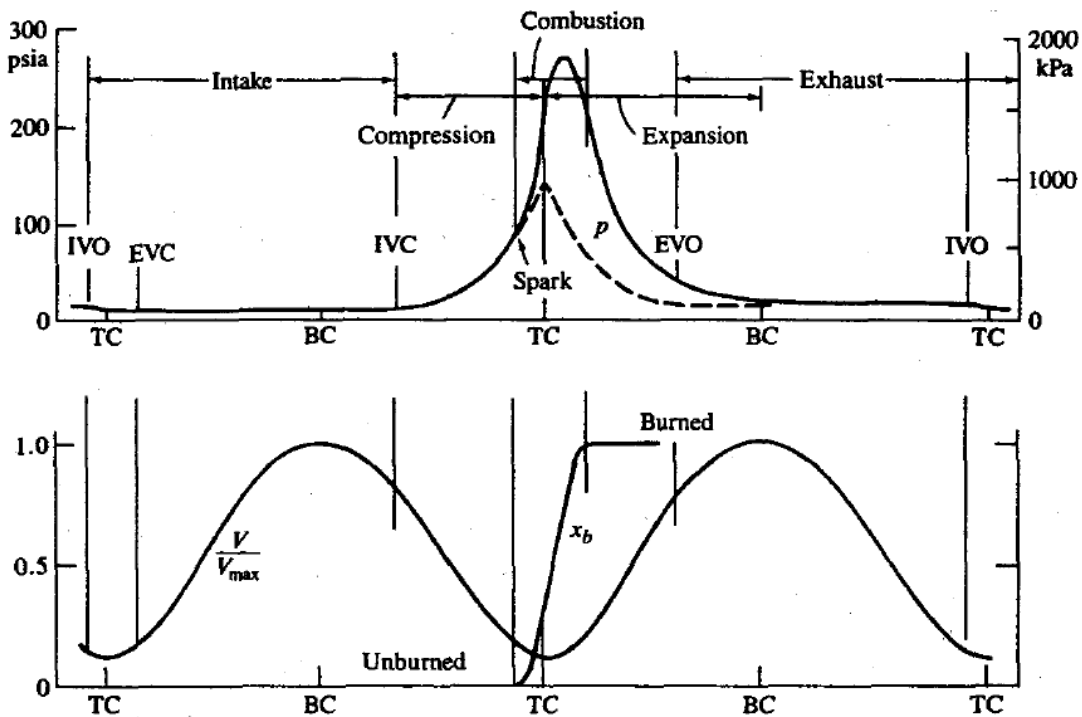


Figure 4 Sequence of events in a four-stroke spark ignition engine. Figure is from Heywood pp.18 [5]

To illustrate the change in internal energy (ΔU), Work done by the gas (W) and heat transferred through the process (Q) a pressure volume (p - V) diagram can be used to illustrate the four stroke combustion process.

In Figure 5 a typical p - V diagram for a 4 stroke CI engine is shown. On the x -axis is the cylinder volume, from top center (TC) to bottom center (BC) on the y -axis shows the cylinder pressure. From the p - V diagram the indicated work per cycle can be found by integration around the p - V curve.

For 4 stroke engine it is common to differentiate between gross indicated work per cycle $W_{C,ig}$ which is the work delivered over the compression and expansion stroke only. $W_{C,ig}$ can be found by integrating the hatched area A plus C in Figure 5. The other representation is net indicated work per cycle $W_{C,in}$ which is the work delivered to the piston over the whole four stroke cycle. $W_{C,in}$ is found by integrating area A plus C in Figure 5 and subtract area B plus C in Figure 5.

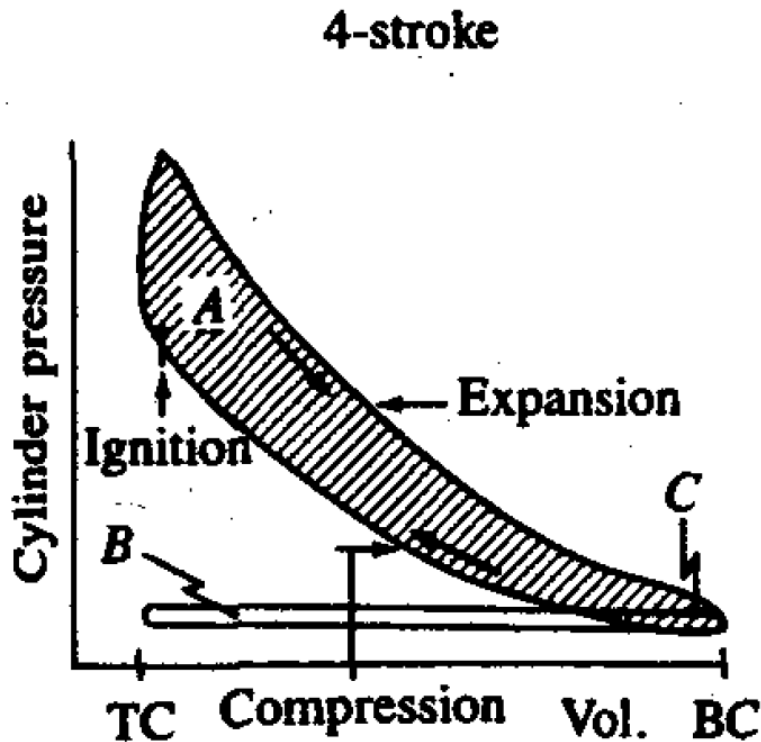


Figure 5 p - V diagram for a four-stroke engine cycle. Heywood pp. 47

1.1.2 Combustion Modes and Flames Types

In short combustion can be defined as a rapid oxidation process generating heat and light [6]. In a reciprocating engine, energy stored in chemical bonds is transformed to mechanical work through the combustion processes. There are two basic modes of combustion, either as a flame or a non-flame. A flame is divided into two categories; premixed or non-premixed. None-premixed is also known as a diffusion flame. In a diesel engine both premixed and diffusion flames occur in various degrees through the combustion process.

The combustion conditions in the engine are mainly determined by the injection system and the engine geometry. There are two main classes of injection systems; direct injection and indirect injection. In a direct injection engine, the fuel is directly injected to the combustion chamber. The direct injection is the simplest approach where the fuel and air is only partially mixed. This is sufficient for larger engines with high compression ratios. For smaller CI engines used in modern cars, mixing of fuel and air is critical to achieve combustion and reduce emissions. Therefore, a premixing chamber can be used to improve the mixing conditions. In the engine used for this project the engine is fitted with a direct injection fuel system. The geometrical design of the piston head, and the air inlets-outlets also plays an important factor to the flow pattern inside the chamber. A swirl pattern is desired to achieve good fuel-air mixing. Typically, fuel injectors have 4 or more holes injecting into the chamber. Figure 6 shows one such diesel injection spray flame. From Figure 6 it can be seen that the spray creates a flame front followed by a soot rich region. The driving forces in the soot formation processes will be discussed in the next section.

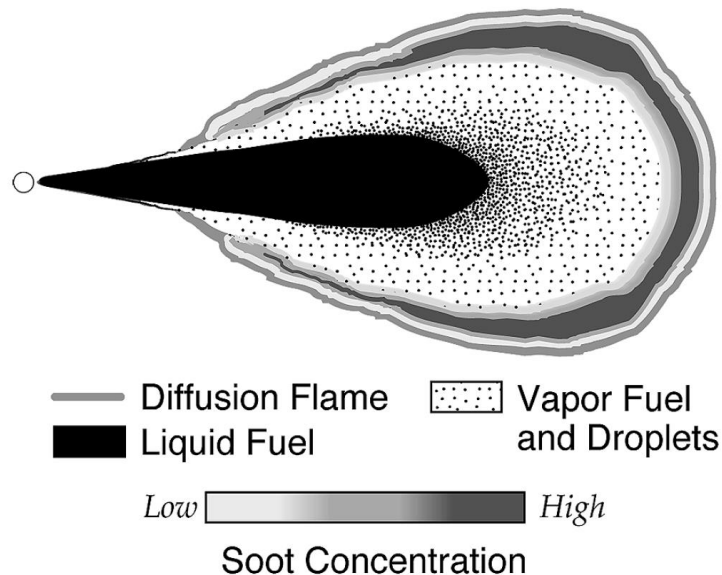


Figure 6 Diesel spray flame

1.1.3 Flame Propagation in a CI Engine

The combustion process in a compression ignition engine can be seen mainly as a turbulent unsteady diffusion flame. For an in-depth analysis, the combustion process readers are recommended to read chapter 10 in Heywood [5]. As a basic introduction to the subject, Table 1 shows high speed images collected from a compression ignition engine, from crank angle degree -7° to 30° .

At -7° the fuel is injected into the chamber. The fuel sprays are seen as dark jets from the injector located in the bottom center of the image. In the next frame at -3° the first ignition occurs. In each fuel spray a bright illuminating flame zone can be seen. The counterclockwise swirl is also clearly visible as the igniting sprays deflects counterclockwise the further away from the inject it gets. In the outside area of the bright spray flame region a weak greenish hue indicates the presence of a premixed flame. (The fuel is doped with a copper additive to create a green hue to visualize the premixed flame.)

At TC the flame propagates rapidly through the cylinder. At this moment, most of the flame is confined within a bowl shape in the piston. As the flame propagates further and the gases expand the flame expands over the piston bowl, and towards the cylinder walls. At 13° it can be seen a high concentration of soot in the dark and yellow regions of the flame. In the last frame at 30° the flame is retracting and the soot rich regions from the frame above are diluted as the particles mixes with the other gases in the chamber.

CAD	Combustion process images
-7°	
-3°	
TC	
13°	
30°	

Table 1 Combustion in CI direct injection with a 4-spray injector with counterclockwise swirl. Figure from Heywood PP498 [5].

1.1.4 Pollutants from Diesel Engines

The power density of CI engines comes at a price. The relatively high compression ratio implies a combustion process at extreme temperatures. This leads to a significant amount of unwanted emissions in the exhaust gas. The emission gases and particles in the exhaust is referred to as pollutant. The most common pollutants are Nitrogen Oxides (NO_x), Carbon Monoxide (CO), Particle Matter of which contains soot (PM) and unburnt Hydrocarbon (HC). CO₂ is often not referred to as a pollutant in this relationship, since CO₂ is an element that occurs in rather high concentrations in nature. Unlike the substances considered pollutant CO₂ does not cause local nor short-term health and environmental problems. CO₂ is an inevitable product of a combustion process. That being said CO₂ emissions are a significant threat the environment on a global scale. To structure the most common occurring pollutants in CI engines Table 2 gives a brief introduction to NO_x, PM, CO and HC. Looking into the formation factor, location in the flame and the hazards connected to them. NO_x formation occurs at elevated temperature in the outer region of the flame. The nitrogen content of the fuel governs the amount of NO_x formed. NO_x emission leads to smog and acidity in the atmosphere. PM consist of a large portion of soot, the soot particles are incepted in the fuel rich regions of the flame, soot is a significant contributor to smog and is dangerous to inhale. CO is the result of incomplete combustion, proportionally increases with higher stoichiometric fuel air ratio. CO is toxic, odorless gas that is lethal. Lastly HC is formed from unburnt fuel typically in the low temperature regions of the flame. HC is a contributor to smog according to Heywood pp.6 [5].

Pollutant	Governing factors for formation	Location of creation	Emission hazards
NO _x	-Formation of NO _x increases with temperature. -Abundance of nitrogen in the fuel will increase NO _x formation.	-Outer region of the flame where temperature is high	-NO _x emissions lead to increasing acidity in the atmosphere. -Smog
PM	-Soot is a large portion of the PM emission, particles incepted from fuel rich zones.	-Generally formed in the fuel rich zone of the flame. Surface growth continues throughout the combustion process.	-Significant contributor to smog. -Dangerous to inhale
CO	-Result of incomplete combustion. Surplus of fuel.	-Fuel rich zones towards the center of the flame.	-Toxic and lethal -Smog -Odorless
HC	-Unused fuel that does not take part of the combustion process.	-Low temperature, fuel rich regions of the flame.	-Big contributor to smog and the negative health effects that follows it.

Table 2 Relationship between pollutants and where they are formed.

There are various means of reducing and eliminating the pollutants from a CI engine. Amongst the most used active methods are tuning and optimizing air/ratio, injection timing and exhaust gas recycling. As an example, Figure 7 illustrates how air-fuel ratio affect HC emissions. As introduced by Table 2 HC emissions occurs due to abundance of fuel. Hence HC emission can then be reduced by running the engine on slightly lean mixture.

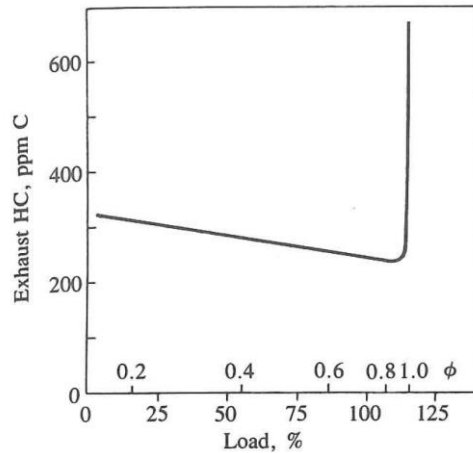


Figure 7 Equivalence ratio (ϕ) effect on exhaust HC emission ([5], p625).

To understand where in the cylinder the most common pollutants are formed Figure 8 is an addendum to Table 2. The figure shows the flame propagation after an injection in a CI cylinder seen from below. The left portion of Figure 8 shows the premixed phase during the combustion process in a shortly after ignition. The mixing of air and fuel can be seen to propagates from the injector nozzle. The edge of the spray is twisted counter clockwise due to the swirling air in the chamber. The lean region of the flame can be seen in the outer edge of the flame as the spray propagates. The right section of Figure 8 shows the combustion process at a later stage in the same combustion event where swirl-effects has had a greater impact and the flame is propagating through the chamber. The flame is quenched as it interacts with the chamber walls, the burned gases are shown with a hatched pattern. As the fuel injection stops the flame moves towards the center of the spray.

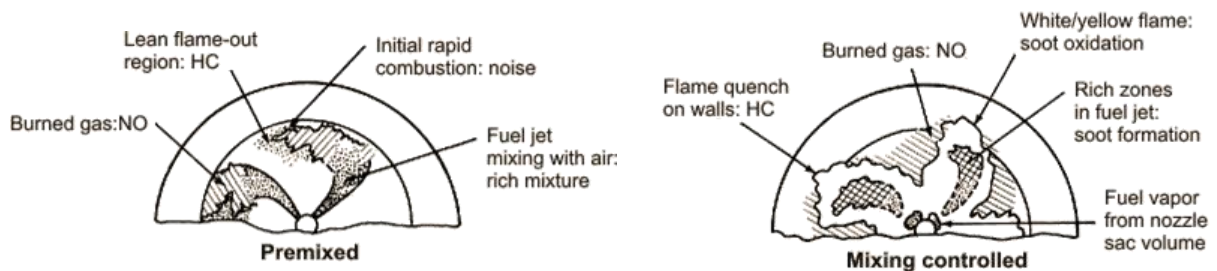


Figure 8 Pollutant formation mechanisms in a direct injection compression ignition engine ([5], p572).

1.2 Soot Formation Fundamentals

Soot is not strictly defined matter; its configuration varies in size and form. In general terms soot is a solid substance consisting of hydrogen and carbon. Right after formation soot can consist of the equal amount of carbon and hydrogen atoms, as time increase the soot particles are saturated with carbon atoms [7].

From CI engines soot usually appear as spherules with a diameter between 10 and 80 nm, and the mean diameter is reported to fall between 15-30 nm [5]. Individual particles tend to group into aggregates often refer to as agglomerates. These agglomerates again form bigger clusters or chains of particles in concentrations of up to as many as 4000 particles [5]. The density of soot is reported by Choi et al. to be 1.84 ± 0.1 g/cm³ [8].

In compression ignition engines soot is mainly formed from unburnt fuel, with nucleates from the vapor phase of fuel rich regions in the flame.

The soot formation process involves six commonly identified stages: pyrolysis, nucleation, coalescence, surface growth, agglomeration and oxidation. The five stages of soot formation are illustrated in Figure 9 below. Oxidation is not illustrated in Figure 9 as oxidation may occur at any time during the formation process. In the following section the five stages of soot formation seen in Figure 9 is further investigated.

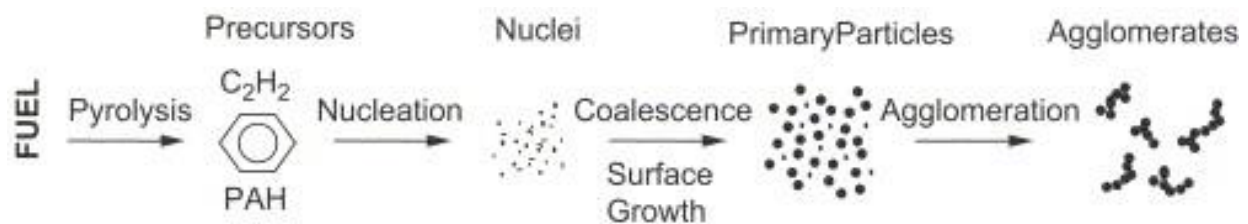


Figure 9 Illustration showing the first five stages of soot formation from fuel in gas phase to a solid, A.K. Agarwal et al PP3281 [9].

1.2.1 Pyrolysis

Pyrolysis is the thermochemical irreversible decomposition of the fuel at elevated temperature with absence of oxygen. Pyrolysis of fuel results partially in the production of species which are the foundation for soot to form. The amount of soot precursors produced is a balance between the oxidation of pure fuel oxidation and oxidation by the hydroxyl radical, OH. With increasing temperature both pyrolysis and oxidation rates increase, but the oxidation rate increase faster. This can be observed in premixed flames where oxygen is present, less soot is produced than in a diffusion flame, where little oxygen is present. During pyrolysis, all fuel compositions produce more or less the same species: unsaturated HC, polyacetylenes, polycyclic aromatic hydrocarbons and Acetylene. Haynes and Wagner [10] described that a decreased residence time in the pyrolysis zone reduced the soot formation in diffusion flames.

1.2.2 Nucleation

Nucleation of soot particles occurs from gas phase reactants within the flame. The observable soot nuclei formed has an estimated diameter of 1.5-2 nm according to Bartok and Sarofim [11]. Bartok and Sarofim suggest that particle inception process consist of radical addition of small, aliphatic hydrocarbons to larger atomic molecules. Reports observing nuclei inception claims that it occurred at local temperature from 1300 to 1600 K. Shortly after formation the nuclei particles does not contribute to a significant amount of particle with respect to the total soot in the flame. However, as time increases the nuclei acts as an inhibitor for further surface growth, and later in the process the amount of soot nuclei incepted has a significant impact of the total soot created [7].

1.2.3 Surface Growth

After the nuclei is formed surface growth is the continuous process of mass addition to the surface of the nucleated soot particle. The hot surface of the soot particles becomes highly reactive and will absorb hydrocarbons, mainly from ethylene in the gas phase. During the surface growth process soot particle gains the main body of mass. Interesting behavior has been reported by Bartok and Sarofim [11] where smaller soot particles grows faster than large soot particles, because small soot particles have more reactive radical sites.

1.2.4 Coalescence and Agglomeration

Further soot particle growth is usually caused by coalescence where two primary soot particles react and forms another spherical soot particle with the size as the sum of the input particles. Agglomeration is the natural process where primary soot particles is attracted to each other and often stick together in a cluster or as long strings.

1.2.5 Oxidation

Oxidation is a reduction reaction of hydro carbons to combustion product, as hydrocarbons are converted to CO, CO₂ and H₂O. The oxidation reaction can take place thru the combustion processes [9]. Various variables govern when the oxidation occur during the combustion phase. Amongst the most important variables governing the oxidation conditions are fuel composition and air-fuel ratio. In a study by Glassman [12] also indicated that soot particle oxidation occurs when the temperature is at least 1300 K or higher. Unlike the other soot formation processes introduced in chapter 1.2.1-1.2.4 the oxidation process is a soot reducing reaction. If carbon is partially oxidized to CO the hydrocarbon will not be converted to soot later in the process, even if it enters the fuel rich zone [9].

1.3 The Optical Engine at EPT

The CI engine used in this project is a generic large displacement, low RPM engine intended as a power producing engine. The cylinder head is modified with two windows to allow for the optical access across the combustion chamber. The combustion process is recorded with a high-speed camera, and a back-illumination system. With this setup, the goal is to obtain time resolved measurements for the soot formation and concentration through the combustion process. The optical engine rig is shown as the blue assembly in Figure 10. To the right of the engine an electric motor is connected through the yellow shaft hub.

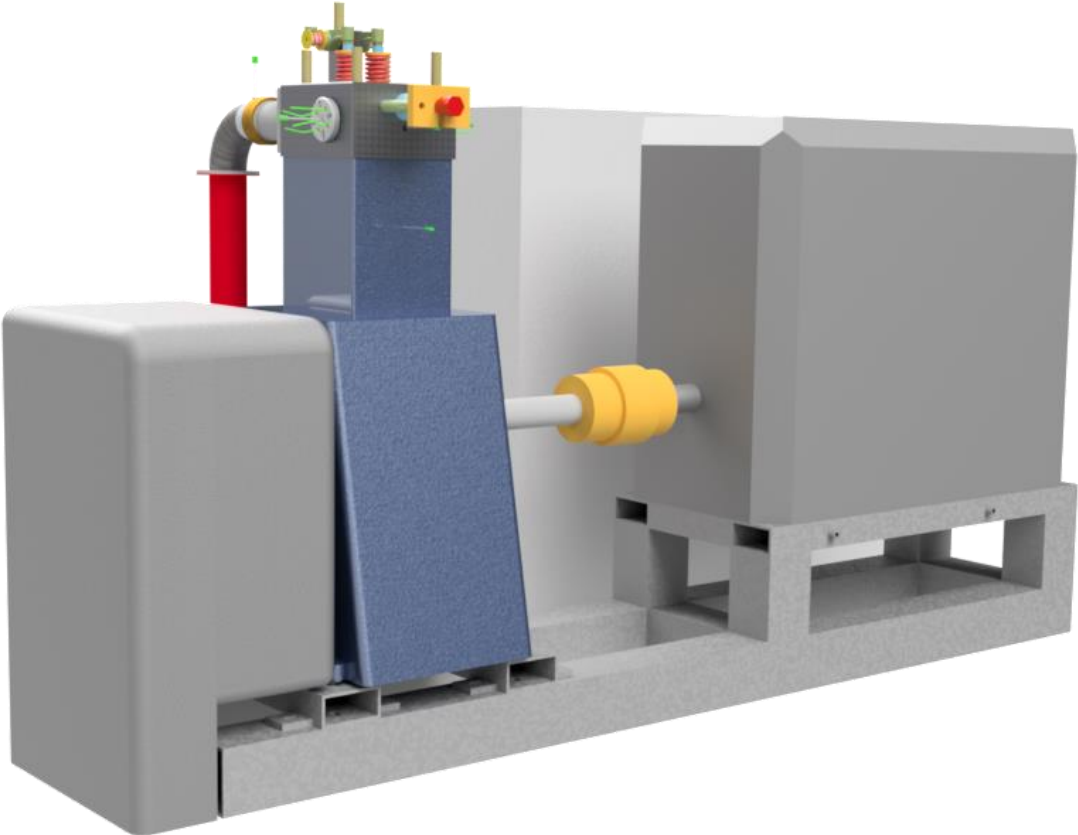


Figure 10 Render of the optical engine rig at EPT from CAD environment

In Figure 11 a split section view through the center of the engine is presented. The figure shows the location of the combustion volume, injector, valves, intake and cylinder to give the reader an introduction to the engine configuration. Figure 12 shows a ¼ section view through the combustion volume. the figure shows the location of the combustion volume and how the window are used to seal the optical combustion chamber. The yellow piston is seen in the cylinder sleeve and the red connection rod connected to the output shaft. In Figure 13 another section view of the engine head shows the optical combustion chamber with the quartz windows, gaskets and the window retainers. In the air channel between the piston and the optical combustion chamber a brass colored throat can be seen in Figure 13. This throat can be mounted or removed too have some adjustability with regards to the compression ratio.

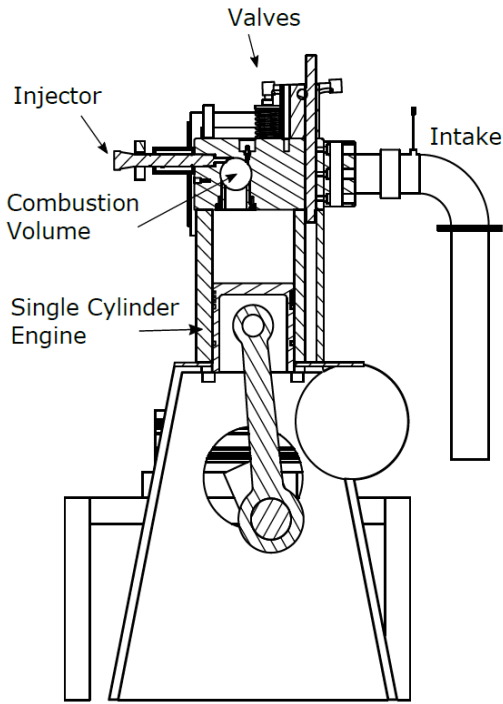


Figure 11 2D section view of optical engine

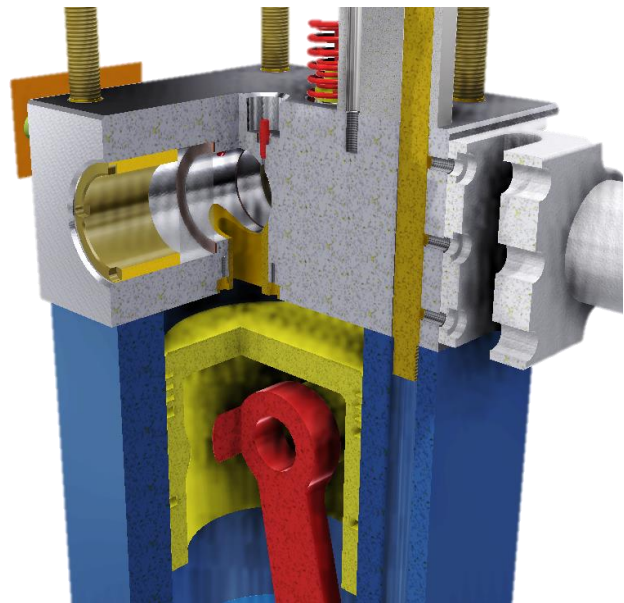


Figure 12 Isometric ¾ section view of optical engine

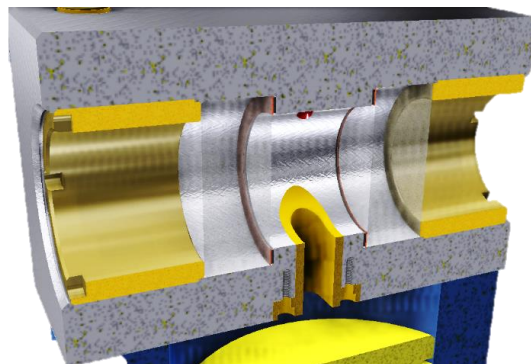


Figure 13 Isometric section view engine head across the combustion chamber

1.3.1 In Cylinder Soot Detection

A special interest for this project is to obtain time resolved soot measurements through the combustion process in the optical accessible CI engine. Due to the growing interest in clean energy, biofuel is an important green alternative to conventional diesel. Therefore, it is increasingly important to understand and characterize soot formation from biofuels in CI engines. The topic is researched across nations and scientific communities.

In 2008 the Engine Combustion Network (ECN) was established by a group of prominent researchers. The network is an initiative from Sandia National Labs (SNL), a private contractor for U.S. Department of Energy's National Nuclear Security Administration (NNSA) [13]. The goal of the network is to facilitate validation of computational models at conditions appropriate for engines [14]. Within ECN an emphasis is put on soot and particle formation in compression ignition engines.

Within ECN various experimental methods are used to capture in cylinder soot formation. Optical methods and quantitative gas sampling are the two methods mainly used. To understand soot and particle formation processes the optical methods are superior as time resolved formation processes can be studied, and provide valuable information to build models and further understand particle formation. The in cylinder optical methods can be used in various configurations. From relatively simple one-dimensional laser light scattering (LLS) experiments to more complex two-dimensional systems. A 2016 study shown that in cylinder soot measurements by endoscopy and CCD photography can also be a good alternative to light extinction methods [15].

Spatial time resolved optical methods (imaging) is preferred due to its non-intrusive nature and the potential for high time resolution. The alternative to the spatial imaging are native two-dimensional laser methods. Either by laser induced scattering (LIS) or laser induced incandescence (LII). LIS LII both requires a high-power laser, with precision optics to shoot a sheet of light through the flame while a camera is mounted perpendicular to the sheet of light [16]. While the image of the sheet of light results in precise measurements of particles in the flame the weakness of this method is the fact that only one cross section (sheet) of the flame can be imaged for each combustion cycle. As the combustion flame from a CI engine is highly turbulent this is a potential problem for using LIS and LII to create a full image of the soot formation and oxidation during a combustion event. As mentioned LIS and LII are accurate methods, but mainly due to its complexity and cost the method is not viable for this work. A cost-efficient design is chosen instead, based on a proven optical method that utilized a illumination optimized diffuse back-illumination extinction imaging (IODBIEI). Within ECN researchers from both SNL and Universitat Politecnica de Valencia (UPV) has utilize this method. The optical setup used at SNL and UPV consist of a high intensity, quasi-diffuse illumination source, bandpass filters, and a high-speed camera. This intensity optimized IODBIEI is based on an optical configuration presented by Ghandi and Heim [17] show in Figure 14.

The intent of the optical configuration by Ghandi and Heim is to create a setup for fuel spray imaging where the light intensity is optimized to supply enough light to the camera to capture high speed images. As the camera shutter speed approaches the order of single digit microseconds it can be challenging to supply sufficiently intense and stable light to saturate the camera sensor.

A critical component of the light optimized DBIEI configuration by Ghandi and Heim is the field lens seen in the center of Figure 14. The *field lens* is a Fresnel type lens. A Fresnel lens is a lens with large aperture and short focal length. As seen in Figure 14 the Fresnel lens is positioned downstream from the diffuser. When the diffused light source is placed at the Fresnel lens focal-length the Fresnel lens collects the light and directs it towards the test section. While the Fresnel lens allows for light towards the test section, the tradeoff is that the light going through the test section is no longer truly diffused. It is desired to have the most diffuse light as possible to reduce the light distortion effects when imagining the combustion event. Light distortion will be discussed in detail later. The intensity optimized DBIEI is then only expected to have a quasi-diffused light going through the test section. This intensity optimized setup is used as a basis for the soot detection tests as the setup is comparative to research at Sandia labs and UPV Valencia. A new optical configuration will be introduced towards the end of this thesis and a comparison will be made between the new and the old setup to determine if the effect of light distortion is reduced in the new setup. The latest progress review from ECN indicates a new and possibly better optical configuration for this use is under development at SNL [18]. This new design claims reduced perceived attenuation due to beam steering. However, the new design refers to a submitted but unpublished paper with the title: “Diffuse back-light illumination setup for high temporal resolution extinction imaging” submitted to “Applied Optics 2016” by Fredrik Westlye et al.

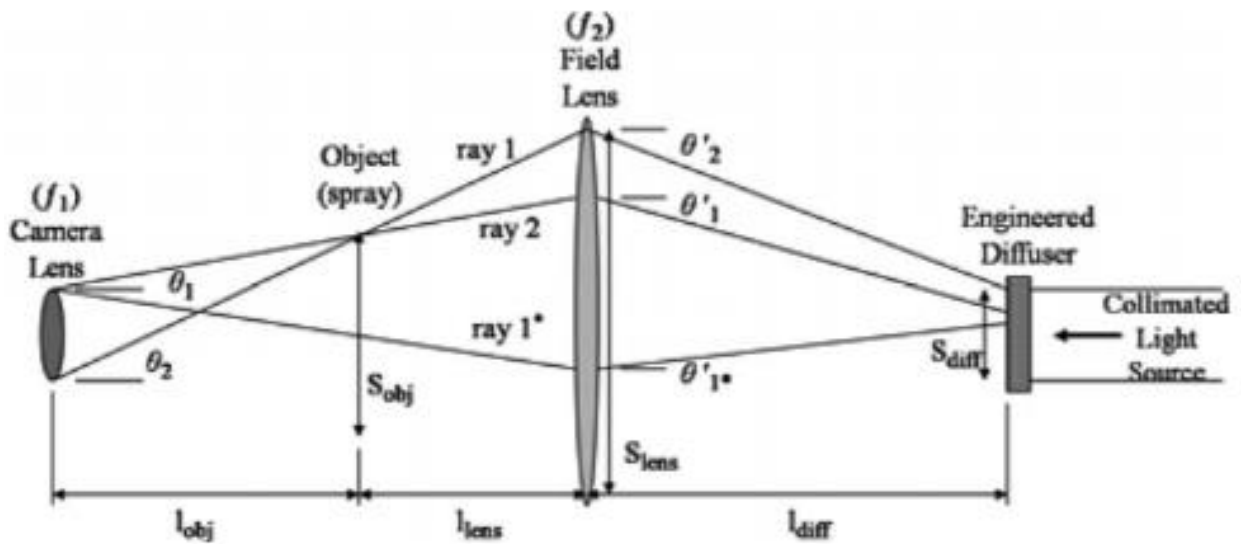


Figure 14 Optical design from Ghandi and Heim. [17]

The latest review from ECN summarizes particle formation from a specific flame. The flame is referred to as “Spray A” flame, and is described in Table 2. Based on recent Transmission Electron Microscopy (TEM) measurements it was observed that the mean soot particles size extracted from Spray A flames to be 20 nm which is consistent with soot formation theory from a laminar diffusion flame at atmospheric pressures [18].

Fuel	n-dodecane
Injection Pressure	150 MPa (1500 bar)
Orifice Diameter	90 μm (nominal)
Ambient Temperature	900 K
Ambient Density	22.8 kg/m^3
Ambient O ₂	15% vol.

Table 3 Parameters for the standardized “Spray A” flame classified by ECN

The soot properties found from the TEM analysis can serve as input parameters for the calculation of the wavelength specific excitation coefficient via the Rayleigh-Deby-Gans approximation for fractal aggregates. ECN has not yet concluded on the true nature of refractive index for in cylinder soot measurements.

Independent researches from both SNL and IFP Energies Nouvelles using different experimental setups obtained quantified soot measurements in the same range, serving as validation of the used methods [18].

1.3 Light Propagation Through Inhomogeneous Media

1.3.1 Background

Light is an essential element of reality as we know it. The theory of light is a topic for debate across scientific communities and disciplines. Our understanding of light is under constant development. This section of the thesis aims to give a brief introduction to light theory, to understand light propagation through inhomogeneous media. The arguments and theory in this section is based on Chapter 1 in the book; Fundamentals of Photonics and Physics by David L. Andrews [19]. And chapter 2, PP25-37 from in the book; Schlieren and Shadowgraph Techniques by Gary S. Settles [20].

In modern physics, it is a fundamental truth that light is based on elementary particles known as photons. Photons possess properties that exhibit particle and wave like attributes. This concept of dual behavior is called the wave-particle duality, and is central to how we understand light. In layman's terms the properties of a photons fits in some conditions with the wave model, and in other scenarios the particle model is needed to describe a photon accurately.

For this thesis, the subject of light theory that is most relevant is propagation of light through inhomogeneous media. This becomes relevant as the end goal of the optical engine rig is to capture real time combustion events. As high-speed back lit images are recorded through and engine cycle. The compressed air, the injected fuel and the combusting gas creates an environment with greatly varying density gradients that is severely inhomogeneous media.

As an analogy to how light propagates through various types of media starlight is often used as an example. Looking up at stars from the earth's surface the stars seemingly blink and glimmer. As light from a star travel through space, the light rays that reaches earth are essentially parallel to each other, and it could be expected that the star would be a near perfect point light source. The reason the stars twinkle is due to the light passing through the atmosphere that is highly none uniform. The atmosphere is full of disturbances caused by many effects like temperature variations, weather phenomena and turbulence. As the conditions in the atmosphere is continuously evolving the density and the refractive index in the air changes with time. As the ray of starlight interacts with the varying density in the atmosphere the rays of starlight are phase shifted and scattered. The wave model of light dictates that the wave front is perpendicular to its rays direction of travel. As a ray of light interacts with the changing refractive index in the atmosphere, it causes phase distortions in the light waves. It is these varying degrees of phase distortions and scatter that causes the stars on the night sky to twinkle

Refractive index (n) is based on the effect that light slows down through interaction with matter. Commonly known the speed of light in vacuum is c_0 is 3×10^8 m/s. The speed of light through other types of media (c) is used to define the refractive index n see in equation (1.1)

$$n = \frac{c_0}{c} \quad (1.1)$$

Density and composition of a gas are the factors that governs the refractive index. The relationship between gas density and refractive index can be seen in equation (1.2). Where the relative speed of light through the gas defined in equation (1.1). k represents the Gladstone-Dale coefficient. For air at standard condition k is approximately $0.23\text{cm}^3/\text{g}$.

$$n - 1 = k\rho \quad (1.2)$$

For most gasses the Gladstone-Dale coefficient, k varies roughly from 0.1 to 1.5. And for most common gasses, the refractive index n only varies with a small amount, usually in the third or fourth decimal place. As an example, air at 0°C and at 1 bar pressure has refractive index $n=1.000292$, when illuminated by light from the sodium-D spectral line at wavelength of approximately 598nm, that translates to orange light. For the same conditions helium has refractive index of $n=1.000035$. The variation in refractive index is seemingly small but the difference between refractive index in the gasses can clearly be seen with the schlieren and shadowgraph equipment. To put equation (1.2) in perspective we can see that a change in density (ρ) has a relative small effect on the refractive index. A change in density of air with two orders of magnitude only leads to a 3% change in refractive index n . This tells us that we need very sensitive optics and precise equipment to detect small changes in refractive index. The refractive index is dependent upon gas composition, temperature and density and the wavelength of the light used for illumination.

During the combustion event the gasses inside the chamber undergoes a highly compressible flow. In compressible flow density gradients are caused by high temperature difference and varying gas speeds. These effects are all factors that will lead to non-uniformity in the refractive index and result in distortion of the light passing through the optical combustion chamber

This brings us back to the reason propagation of light through inhomogeneous media needs to be addressed in the first place. For the optical engine rig the image technique used to capture the combustion event is essentially a high-speed shadowgraph image. As light from the light source travels through the combustion chamber and interacts with the turbulent gasses, atomized fuel, and the flame. With the theory on how light propagates through inhomogeneous media fresh it can be assumed that light which travels through density gradients and various media with vastly varying refractive index will experience some sort of deformation/distortion from its original path. The impact of light distortion through the process can be significantly large and the effect needs to be addressed and investigated for experimental setup. By addressing light distortion properly and taking the necessary measures/improvements the experimental results can be presented with greater confidence. In recent literature on the subject of light distortion in the field of the optical combustion analysis is often called *beam steering*. The term beam steering is seemingly used inconsistently as it in some papers appear as an umbrella term to describe artifacts and inhomogeneities in images caused by light distortions but also other effects [21].

The effect of light distortion is unfortunately scarcely presented with good data from studies on optical accessible combustion chambers, most likely due to a high degree of uncertainty and varying conditions. Light distortion effects on optical engines are more often presented with comparative data. In a study from 2008 by Thomson et al. [22] presents a comparison between two experimental setups. Thomson et. al shows how light distortion affects the uncertainty in a specific

optical soot measurement. Two different optical configurations were investigated. One setup where the light entering the test section is collimated and a setup with diffuse light entering the test section. The result of the two optical configurations from Thomson et. al [22] is presented in Figure 15. The two images to the left in the figure show collimated light, and the two right sections the diffuse light. f_v represents the volume fraction and σ_{f_v} represents the standard deviation in the volume fraction region. Both variables are plotted as a 2D map, blue; low concentration, to red;high concentration.

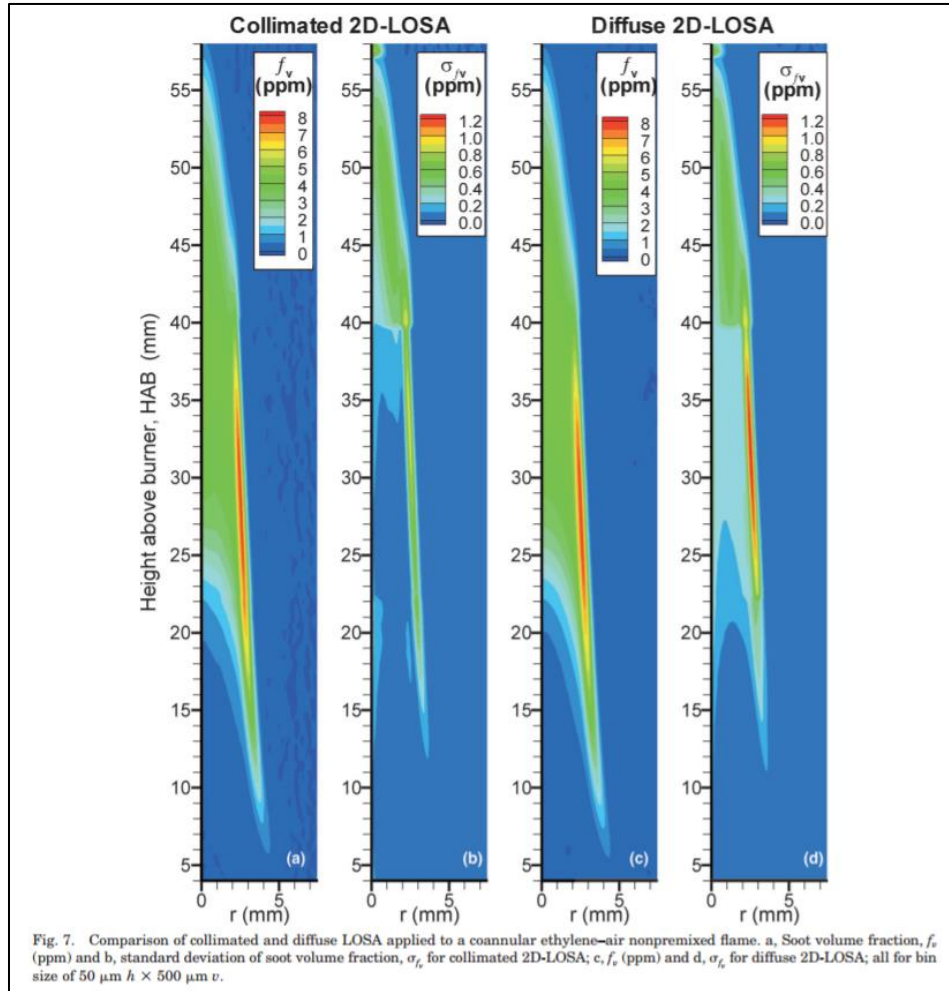


Figure 15 Beam steering illustration from Thomson et al. [22]. In the images, the f_v represents the volume fraction and σ_{f_v} represents the standard deviation in the volume fraction region.

From Figure 15 it can be seen from comparing the soot volume fraction, the uncertainty σ_{f_v} across the two 2D image shows that the uncertainty in the diffused setup is differing from the collimated setup. It is expected that the absolute uncertainty in the soot concentration σ_{f_v} should follow the soot concentration f_v . For the collimated setup in can clearly be seen that σ_{f_v} is almost non-existing towards the center of the flame region even though there is a concentration of soot detected there. With this logic, the relative uncertainty should follow the soot concentration. Therefore, the diffuse setup in Figure 15 shows improved prediction of soot concentration and a more probable

distribution of uncertainty in the measurements. Thomson et. al concluded that by diffusing the light before entering the test section, light distortion is drastically reduced.

A 2005 paper Musculus and Pickett [23] addresses and investigates the effect of light distortion on an optically accessible combustion chamber like the rig used in this project. By using a laser beam and a collection system they investigate how a beam of light is deflected in the engine when compressing air and when being fired.

The result of this 2-D beam deflection experiment is presented in Figure 16. The figure illustrates how the laser beam is deflected at various crank angle degrees. There are clear differences in ray deflection between the motored and fired. The fired show significantly larger spread and scattering of the laser beam.

This trend is expected as fuel is injected into the systems and through the combustion, various particles and temperature gradients drastically increase conditions where light distortion can occur. From this experiment, it was concluded that scattering through the high pressure fired diesel engine, beams diverged by more than 100mrad. The engine used in this study were reported to operate at max pressure between 50 and 70 bar. It is also given a clear indication that magnitude of beam deflection is dependent chamber pressure. As the engine used in this study operates at around 30 bar the deflection angle is expected to be smaller.

Musculus and Pickett also point out that the windows to the combustion chamber might add uncertainty due to varying refractive index caused by mechanical strain and thermal input, at last deposition on the combustion chamber windows also expectedly pointed out as an essential factor than add uncertainty.

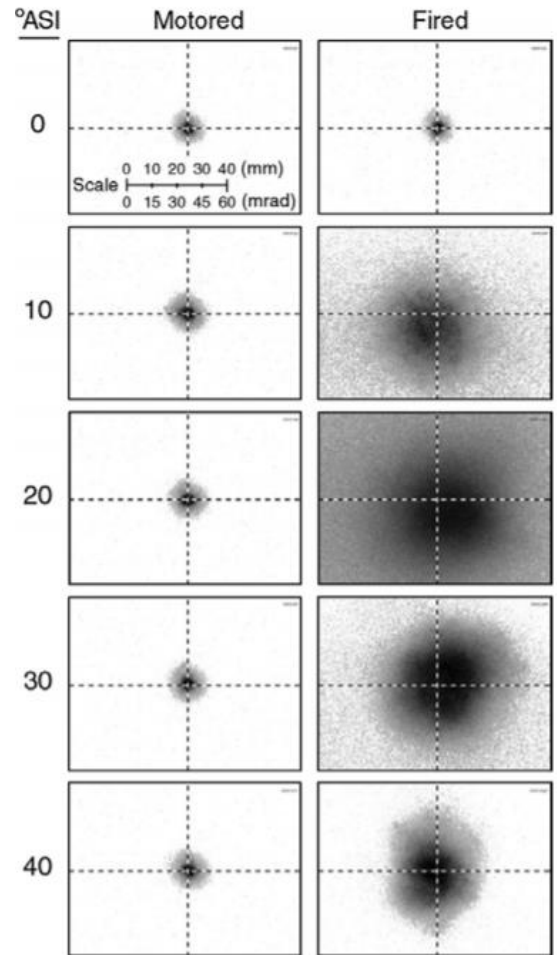


Figure 16 The figure shows extinction laser beam spot after passing through the engine. The dotted crosshairs indicate the center position of the beam with no deflection/beam steering.

In the 2004 study; *Multi-Species Laser-Based Imaging Measurements in a Diesel Spray* by Schulz and Gronki, the term beam steering is used to describe non-uniformity in the laser beam. [21] The non-uniformity in the laser beam is reportedly responsible for creating horizontal sections with varying light intensity due to the laser intensity. In the paper, an algorithm is suggested to adjust the images. The raw images are seen on the top of Figure 17 and the algorithmically improved images are shown in Figure 17. It can be seen that the resulting images have mitigated the horizontal intensity section by smoothing out the image intensity. In this thesis, this artifact in the illumination pattern caused by an un-even light source would not be considered beam steering or light distortion. Hence, this example is used to show that some articles uses the term beam steering liberally. For this work light distortion will be used as a term to describe effect caused by the light interaction with the various refractive gas through the combustion process. The effect reported in Figure 17 would be considered artifacts in the images due to inhomogeneous LED background illumination.

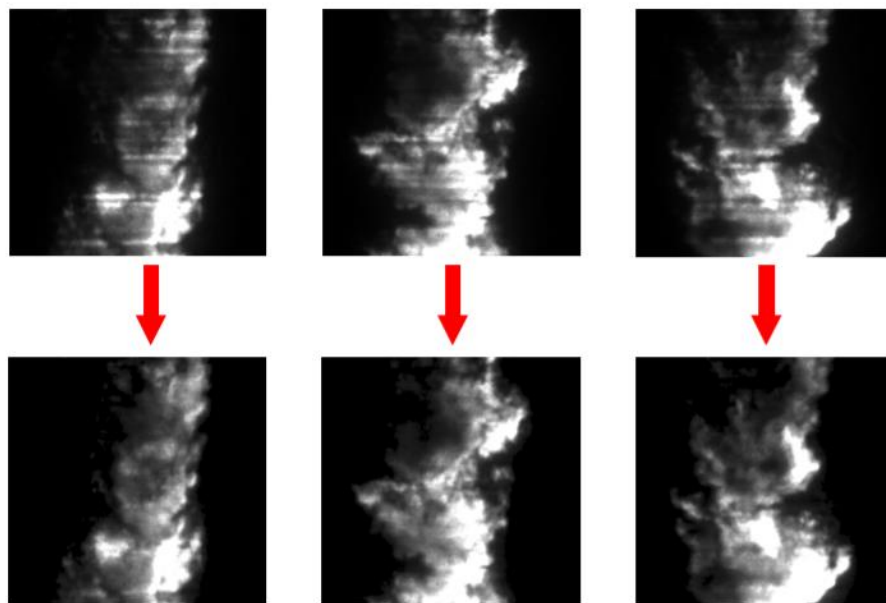


Figure 17 Illustration from Schulz and Gronki [21], upper section of the image shows horizontal sections of varying intensity. In the bottom of the figure are the improved images.

1.3.2 Diffused Light vs Collimated Light

In collimated light the rays are parallel to each other. In reality, collimated light sources emit light that is close to parallel, but not perfectly parallel. A point light is one such source. The light from a point light source can act as a collimated light source placed at the focal point of a collimating lens. Light rays from a collimated source is illustrated in the left section of Figure 18 annotated with *parallel light*.

Diffuse light on the other hand consists of diverging light rays. An example of diffuse lighting is shown in the right section of Figure 18. Most light sources emit light that is closer to parallel than diffuse. Collimated light can be diffused by interacting with a medium that scatter the light. To diffuse a light source many options are available. Diffusor is a term used for lenses that diffuses a light source. Many type of diffusors are available for scientific use. High precision diffusors with specific output angles are available. It is worth noting that when a diffusor is introduced to a system it is expected that some of the light will be absorbed and scattered away from the test section. This will cause the light intensity to drop. This can be compensated for by increasing the intensity of the light source if needed.

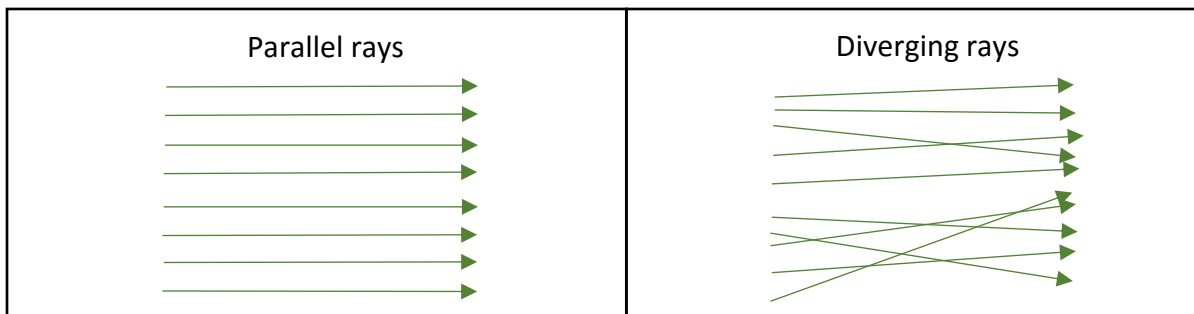


Figure 18 Example of parallel and diverging rays.

1.3.3 Collimated and Diffuse Light Sources Interaction with Refractive Objects

For the optical soot measurements, we are interested in quantifying the amount of soot through the combustion process. To obtain precise results it is important that the effects of light distortion is mitigated. As discussed earlier in the thesis there are many factors that can lead to light distortion in the combustion chamber. Density gradients in the compressed gas and atomized fuel are potential sources of extensive light distortion. Understanding how collimated and diffused lighting interacts with refractive objects can be used as a powerful tool when designing experiments to reduce light distortion.

In Figure 19 a body with higher refractive index than the remaining environment the rays of light travels through is introduced to the light path. The body with higher refractive index is introduced into the light path shaped as a triangle in Figure 19. The reader is advised that Figure 19 is a highly simplified example for illustration purposes only.

Looking at the parallel rays it can be seen that the light interacting with the blue body is distorted and leaves a “hole” in the column of light.

Looking at the right section of Figure 19 representing diffused light, it is eminent that the rays of light interacts with the body. But looking at the light column the same refractive body in the light path does not leave an empty section in the light column. Effectively this means that the cone of diffused light is less prone to distortion due to changes in refractive index.

As parallel light interacts with a change in refractive index all the rays enters from the same direction and angle. For the diffused light the rays of light interact with the refractive object from various angles and directions. The diffuse light will also be deflected by the interaction with the refractive object but since the diffuse light interacts with the object from various angles no clear pattern is defined such as for the parallel light where more or less all of the light is deflected in the same direction. This causes the diffused light to be less prone to distortion due to change in refractive index.

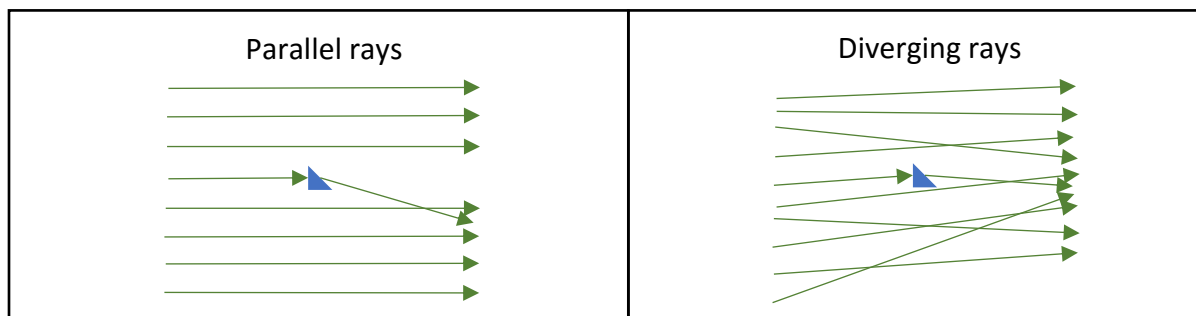


Figure 19 Body with change in refractive index introduced to the parallel and diverging rays.

1.3.4 Light Simulation of Interaction with a Refractive Object

Through a light simulation software an attempt is made to create an illustration of light interacting with a refractive object. The software used is named RayViz by Lambda Research corporation and is ray tracing extension to SolidWorks [24]. The program offers an array of adjustable variables that can be applied to 3D objects and light sources. In Figure 20 Light interacting with a large sphere with the refractive index of water. Section a) show collimated light and b) shows diffuse light. the images show ray tracing simulation for collimated light and diffuse light. The gray sphere seen in the light path is assigned the refractive index of water, where $n=1.330$ [25].

As seen in Figure 20 a) as collimated light interacts with a sphere, the cone of light is deflected in a rather uniform manner. This will result in a rather large shadow on the gray wall behind the sphere. The gray wall is defined as a black body and will not reflect any light. For the other case with diffuse light seen in Figure 20 b) no distinct shadow of the sphere appears on the wall. The rays of light that interacts with the sphere will still be deflected for the diffuse light, however since the diffuse light interacts with the sphere from a variety of input angles a much more uniform pattern is seen on the wall. It can be imagined that the wall is replaced with a camera, in this case the sphere will leave a large dark section with collimated light. And for the diffuse light it is expected some distortion but the sphere will not leave a distinct shadow as it does for the collimated light. The illustration in Figure 20 Light interacting with a large sphere with the refractive index of water. Section a) show collimated light and b) shows diffuse light. is far from ideal. Since the geometry in the two cases are kept identical the light cones interacting with the sphere will vary.

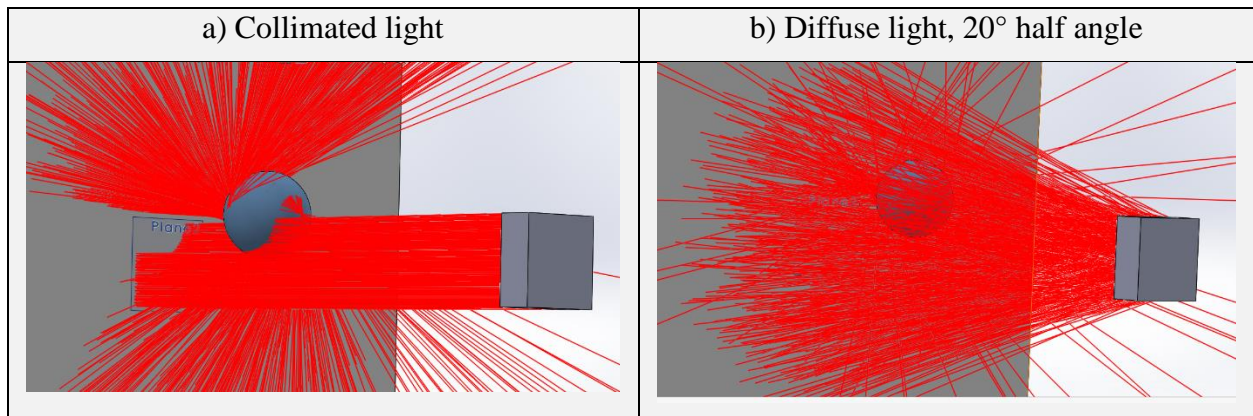


Figure 20 Light interacting with a large sphere with the refractive index of water. Section a) show collimated light and b) shows diffuse light.

Using the same technique as above Figure 21 shows 4 images of the interaction between diffuse and collimated light. In Figure 21 a larger sphere is used to cover the whole light cone for both light types. Once again, the left section of Figure 21 a) and c), shows collimated light and the light is distorted a significant amount. For the diffuse light the pattern seen in Figure 21 b) shows that the diffused light is distorted quite a bit. After the cone of light has passed through the sphere the a cone of light covers almost the same area as it did before entering the sphere, and there are no significant gaps in the illumination pattern. For the collimated light in Figure 21 a) and c), the light cone is twisted into a triangle like pattern. If a camera were to be placed downstream of the sphere pointing toward the light source. The collimated light would result in an image with a large dark section and a bright spot where the light is distorted and concentrated. For the diffuse setup the illumination pattern would be more uniform if a camera was in the same position for both light types.

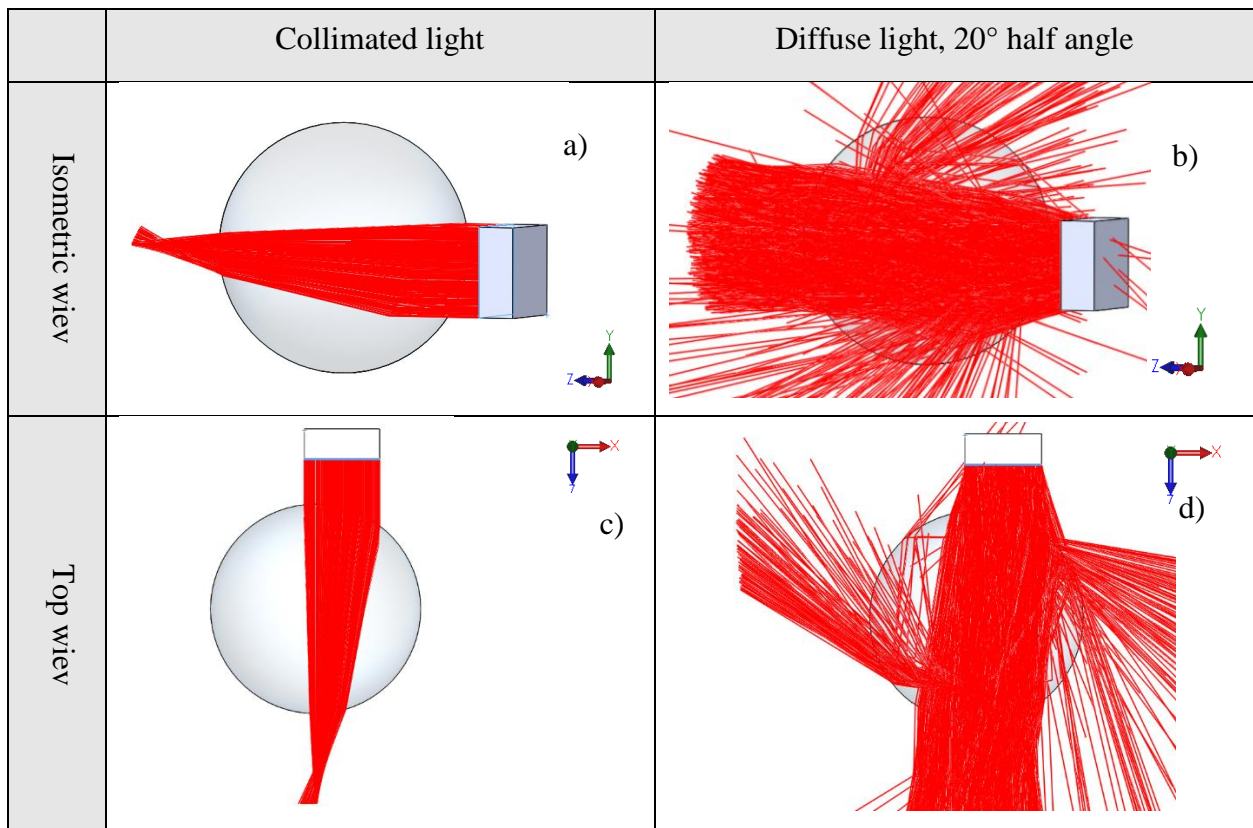


Figure 21 Light interaction with a large sphere

Chapter 2 Method

2.1 Introduction to Experiments

To test and verify the feasibility of the optical engine rig, three separate experimental rounds are conducted. First a series of preliminary experiments for soot detection and the optical light extinction setup will be tested. These preliminary soot detection tests are carried out in an early stage of the project with engine partially disassembled. The intent of this first experiment is to verify if the setup works as intended with acceptable accuracy. The experiment can uncover if new parts needs to be ordered or changed while the rest of the engine is being built and the control system installed.

The second section a series of experiments are conducted after assembling the engine to test the heating characteristics, required window torque to seal the optical chamber and chamber compression tests.

The third section consist of experiments to determinate the light distortion conditions in the engine and a comparative study of the light distortion conditions in the two optical configurations, respectively the IOBIEI and a new DBIEI.

For each of the three main experimental sections the results and analysis is presented consecutively. As each of the sections consists of various data types ranging from 2D images to simple thermocouple data. Each experimental section requires a certain amount of data processing that is conducted in MATLAB. The scripts purpose written for each data analysis job is mentioned in the experiment and found in the printed and digital appendix.

To aid the understanding of the experimental approach in this thesis Figure 22 shows the three experimental sections described in the text above. Within the three sections the sub goals of the experiments are listed.

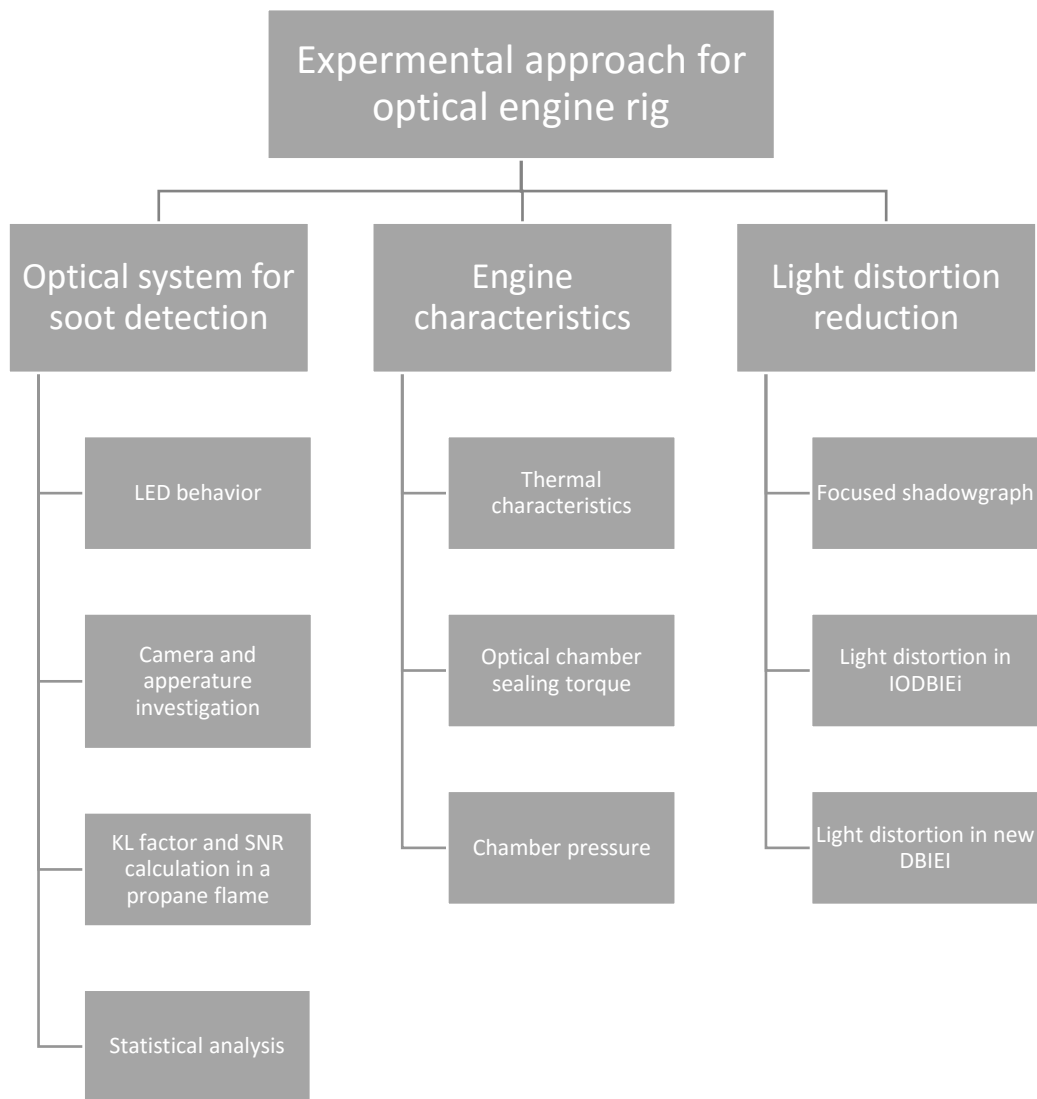


Figure 22 Overview of experiments in the thesis. Three main sections of experiments.

2.2 Optical Method

In the experiment, the optical setup is an intensity optimized diffused, back-illumination, extinction imaging (IODBIEI) system. The IODBIEI is used by other research groups for in cylinder soot measurements, due to its non-intrusive characteristics, high speed measurements and relatively low cost. [26] [18]. This will be the starting experimental setup for in cylinder soot measurements in this thesis.

With the IODBIEI method a background image is first established as a reference, by exposing the camera to a stable back-light source, without any obstruction of the light. This is illustrated in Figure 23 below. For the second image an unknown substance is introduced between the light source and the camera. The material between the light and the camera will reflect and scatter light from the source, resulting in a different image than the reference/background illumination level captured first in a sequence.

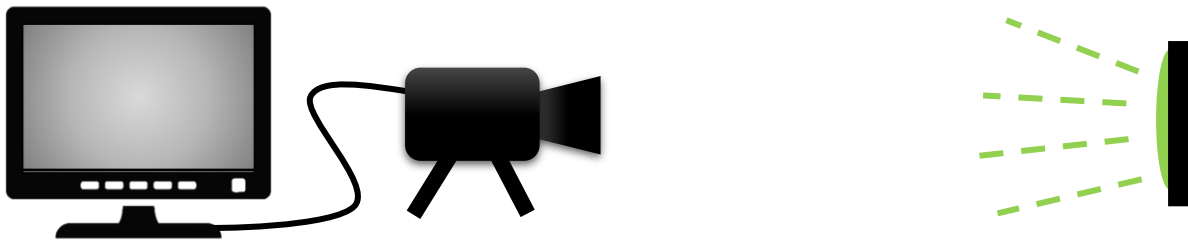


Figure 23 Illustration showing how the background image is captured. The computer screen shows what is seen from the camera.

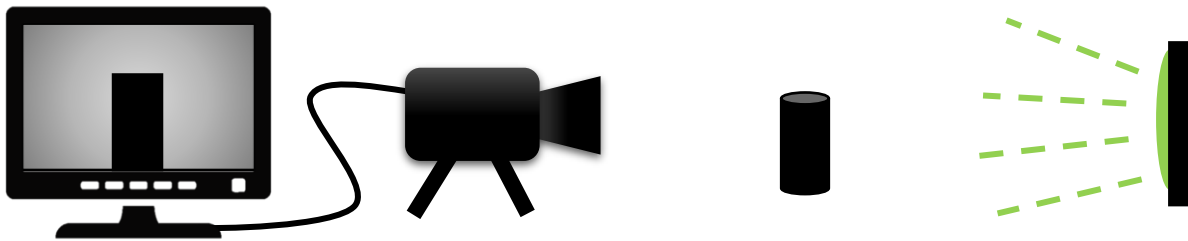


Figure 24 Illustration showing how a material can be introduced between the camera and the back-light source.

In the actual experiment, the black cylinder seen in Figure 24 is replaced with a soot rich flame, and an optical system to improve illumination of the image. When a flame is used as the medium between the light source and the camera, the flame will scatter and absorb some light from the source, and thereby resulting in a lower light exposure in certain regions of the picture. Effectively leaving a shadow image of the object, as seen on the computer screen in Figure 24.

The extinction method is based on light attenuation of medium and known methods of quantifying the light attenuation by particles can be applied. An accepted method in the field is to utilize Lambert-Beer's law to quantify the amount of light attenuated by a medium. Lambert-Beer's is

presented equation (2.1) [16]. This method essentially compares a reference illumination to a illumination level registered with a cloud between the light source and camera.

$$\frac{\Phi_t}{\Phi_0} = e^{(-\tau)} \quad (2.1)$$

In Lambert-Beer's law, Φ_0 represents the radiant flux present without any obstruction of light. And Φ_t is the radiant flux transmitted received with a cloud of particles attenuating light. The factor τ relates to the substance optical depth and absorbance. For soot measurements τ is generally divided into two descriptive factor K and L. Where K represents the mean extinction, coefficient implementing both scattering and absorption across the path length. L represents the path length of the soot cloud [27]. Equation (2.1) can be modified for soot quantifications, the specific form used in theory in the field is presented in equation (2.2).

$$\frac{I_t}{I_0} = e^{(-KL)} \quad (2.2)$$

As the KL exponent in (2.2) is an important quantity for further soot volume fraction quantifications in equation (2.2) and is often presented in the as seen in equation (2.3).

$$KL = -\ln\left(\frac{I_t}{I_0}\right) \quad (2.3)$$

- I_0 Incident light intensity. (No obstruction of light, image created as shown in Figure 23.)
- I_t Transmitted light intensity. (Material introduced, as seen in Figure 24.)
- K Extinction coefficient for a cloud of particles
- L Path length of the light beam through the particle cloud

The optical thickness KL can be directly quantitatively related to the amount of soot present in the flame. By applying Mie theory for small particles, the soot volume fraction (f_v) in the flame can be related to the KL factor as seen in equation (2.4) [28].

$$KL = \int_{-z_\infty}^{z_\infty} f_v(z) \frac{6\pi}{\lambda} (1 + \alpha_{sa}) E(m) dz \quad (2.4)$$

Where Z_∞ represents the integration cross section of the flame. λ is the illumination source wavelength and α_{sa} is the light scattering to absorption ratio. $E(m)$ is a function of the refractive index of soot (m), where $E(m) = -\text{Im} \left[\frac{m^2 - 1}{m^2 + 2} \right]$ and m is the refractive index of soot. Equation (2.4) can be rewritten with respect to soot volume fraction f_v . The rewritten expression is seen in equation (2.5) [28].

$$f_v = \frac{K \lambda}{k_e} \quad (2.5)$$

Where $k_e = (1 + \alpha_{sa})6\pi E(m)$. From empirical laser induced scattering experiments $(1 + \alpha_{sa})E(m) \approx 0,46$ however these values still include significant uncertainty but serves as governing value for ECN until more accurate data is presented [28].

These relationships can then be used to determinate the optical thickness across the flame and eventually an estimation of the soot volume fraction. An example of how the optical thickness of a diesel spray flame can be presented as seen in Figure 25, the top section of the figure shows the time average optical thickness (KL) factor across the center of the flame with distance from the injector. Figure 25 is found in Pickett and Siebers 2004 [28].

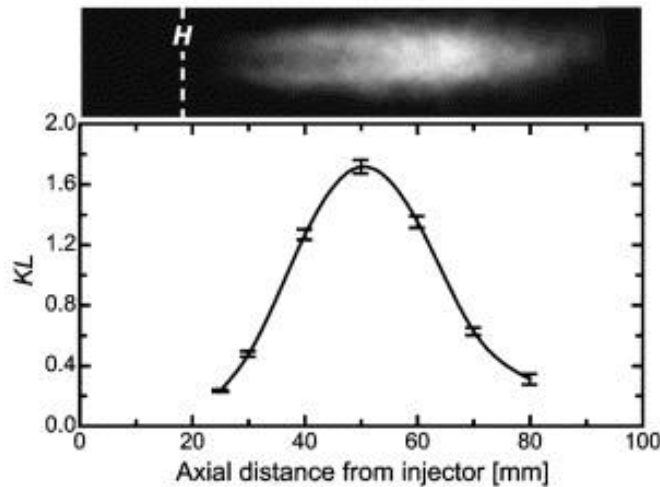


Figure 25 Time resolved KL factor with distance from the injector on the x-axis. Sampled across the center of the flame.

Pickett and Siebers 2004 [28] also presents soot volume fraction axially across the flame, i. e. at a fix distance of 50mm form the injector tip normal to the spray direction. This can be seen in Figure 26 where the soot volume fraction across the dashed line in Figure 25 is plotted. The measured soot volume fraction is plotted with distance across center of the flame.

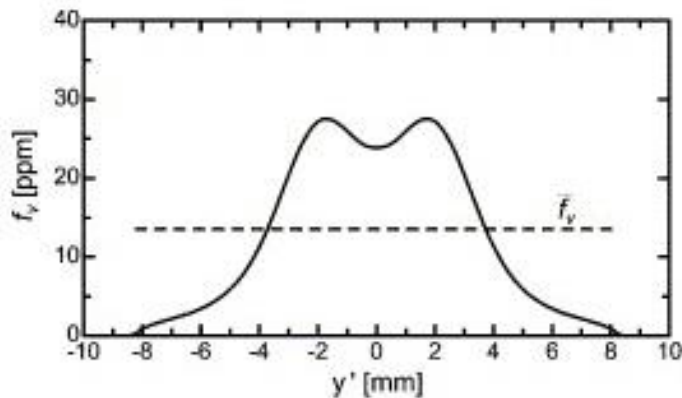


Figure 26 Soot volume fraction f_v axially across the flame at a 50mm distance from injector orifice.

Another figure from Pickett and Siebers 2004 [28] can be seen in Figure 27, this figure add insight to the data collection and the unsteady conditions yielding a relative high variation in soot concentration and optical thickness. In Figure 27 the top plots show a point measurements 50mm from the injector where the soot concentration is collected with time. The time axis is synchronized with start of injection. In Figure 27 the blue line is the KL factor from a single injection and the black show the average KL from 25 injections. There is a relatively high variation in KL from injection to injection as the process is highly unsteady.

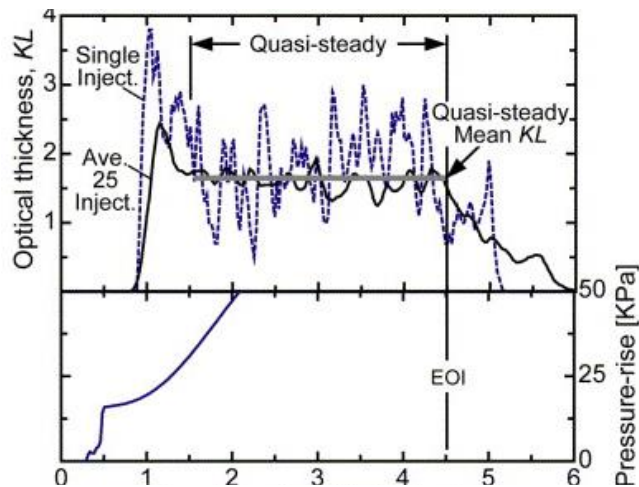


Figure 27 KL factor from a single flame with dotted blue line. And and the average KL factor from 25 injections

2.3 General Setup

2.3.1 List of Equipment

Camera	Photron FASTCAM SA1.1
Camera aperture	Nikon 50mm, 1:1.4D
Neutral density filters	Edmund Optics. OD 0.3-1.2
Engineered diffuser	RPC Photonics. EDC-15-15132.
Bandpass filter	Techspec, M62.5 x 0.75, CWL 524, FWHM 92.
Gate and oscilloscope	BitScope Micro Oscilloscope & Analyzer
Pulse generator	TTi TGP110 10Mhz
LED	Luminus, CBT-120 (green) LED
LED power supply	BK Precision, Model 1687B, 1-36V DC, 10A
LED switch power supply	Mascott, Model 719
Steady state burner	Bunsen burner
Gas supply	Commercial Propane
Pressure and flow regulator	N/A

Table 4 List of equipment.

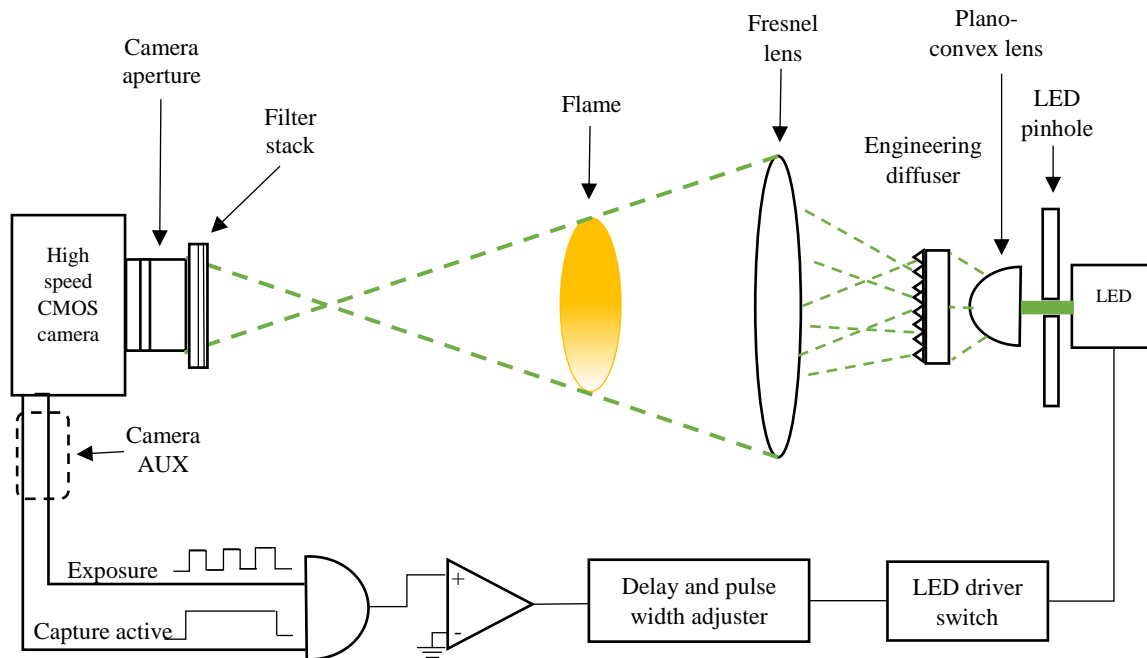


Figure 28 Experimental setup.

2.3.2 General Setup

The camera used is specifically designed for scientific high-speed measurements. The image sensor is a 20 μ m square complementary metal oxide semiconductor (CMOS). This sensor yields a ISO light sensitivity of 10 000, for 12-bit grayscale images, measured in accordance too ISO 12232 [29]. Electronic shutter time ranges from 16.6ms to 1 μ s.

The camera is equipped with programable output signals. In the experiment two of the programable outputs is used to trigger the LED in synchronization with the exposure of the camera. The camera outputs are standard coaxial signal cables. The Camera “general output 1” and “2” is connected to a “AND” gate. From the gate, a signal is generated only when the camera AUX General output 1 and 2 are both active.

The “AND” gate a coaxial cable is connected to a pulse generator. The pulse generator gives the option to manipulate the output signal with a specific period, delay, width, and amplitude. The output from the pulse generator is then sent to the MOSFET switch on the LED circuit, the switch controls when the LED is activated. Two separate power supplies drive the LED circuit. One variable supply to the MOSFET switch. And an individual power supply to charge the capacitors to drive the LED.

The LED chip design is based on configuration published in 2014 paper; “*Performance evaluation of an overdriven LED for high-speed schlieren imaging*” by Wilson and Gustafson et al. [30]. The design describes a high intensity LED with fast switching capability at a low cost.

Between the LED and the camera, a pinhole and series of lenses is introduced in order concentrate the light from the LED. The first element after the LED is a 2mm pinhole. The LED emitting surface is 4.6x2.6mm if higher light intensity is need the pinhole could possibly be changes to a larger dimension. Next in line is a planoconvex lens that collects light from the LED and expands it to cover the diffuser. The engineered diffuser breaks up the incoming light to oblique angles at maximum half angle 15°. Strictly speaking, the LED emits uncollimated light from the emitting surface. However, the light passing through the pin hole is somewhat collimated. The light is then diffused by the diffuser, but again collimated by the Fresnel lens, that’s why Ghandi and Heim’s setup is not thought of being ideal for light extinction. As we have seen the collimated light is prone to distortion due to varying refractive index in the flame [31]. The next component in the setup is a Fresnel lens seen before the flame in Figure 28. The Fresnel lens is a large objective in a compact design, this allows for a relative short focal length compared to its size. The function of this lens is to capture as much light as possible after the engineering diffusor has scattered it.

In Figure 28 the camera objective is Nikon 50D, 1:1.4D. It is also desired to eliminate all other light than the light emitted by the LED. To achieve this a bandpass filter is mounted on the camera lense, represented as a filter stack in Figure 28. A bandpass filter is mounted on this stack that allows light with wavelength from 478nm to 570nm to pass, i.e. only light in the green spectrum passes through the filter. To suppress the illumination from the flame neutral density (ND) filters are also applied to the filter stack. These filters are available in various configurations and it will be investigated what combination of filters will suppresses the flame, and allow sufficient exposure to the camera. The Nikon lens has adjustable focus and f-stop, which offers flexibility in image exposure.

The camera is connected to a windows computer running the camera supplier’s software, “*Photron Fastcam Viewer.*” From the interface in the camera software all parameters of the camera can be controlled. Such as shutter speed, resolution and color mode.

As a relatively stable source of soot a Bunsen burner on propane is used to supply laminar diffusion flame. A laminar diffusion flame with propane was chosen since it can supply and relatively stable soot rich flame for the short duration of an image sequence, and the it is cheap and available at the lab.

2.4 Camera

In the experiment, the *Photron Fastcam SAI.1* camera is the main sensor for data collection. The images captured by the camera is used for calculation of the KL factor in the flame. To understand how the images are threated in the data analysis it is important to understand how the images are recorded. A short review of the CMOS camera sensor is given to aid the understanding of how images are created and stored.

Modern camera sensor consists of arrays of semiconducting devices called photodiodes. The photodiodes convert the energy from a photon into a small current. The photon count on each photodiode is used to construct an array of values. Depending on the design and configuration of the image sensor the output image can either be represented on a grayscale image or as a color image. Grayscale image is the simplest of the two. For colored pixels in an image, three independent readings from a photodiode are needed. Where each photodiode has a bandgap filter to only expose the photodiode to photons with frequency corresponding to either red (R), green (G) or Blue (B) wavelengths. The combination of these three RGB values can be used to construct any color in the visible spectrum, a. In Figure 29 a CMOS pixel photodiode is illustrated with a red color filter.

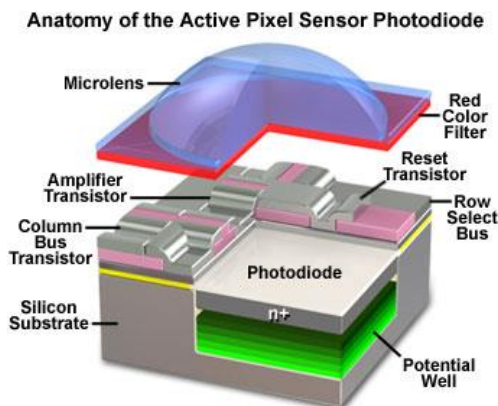


Figure 29 Pixel sensor with a red color filter from an CMOS camera sensor [32].

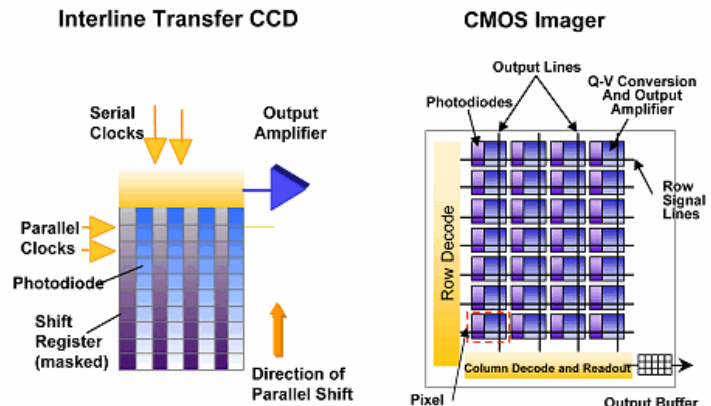


Figure 30 CCD vs CMOS image sensor design [33].

The two most used camera sensors technologies on the market today is the charge-coupled device (CCD) sensor and complementary metal–oxide–semiconductor (CMOS) sensor. The primary

difference between these two configurations is the way the data is transferred from the photodiode to the processor. On the CCD, each cell are analog photodiodes sending analog signals to the amplifier connected at the end of each row in the array. On the other hand, the CMOS sensor has an integrated circuit on each cell. Each photodiode has an analog to digital converter and sends the data directly to the processor. In Figure 29 and Figure 30 above, a CMOS and CCD sensor is respectively illustrated. The direct connection between the processor and each photodiode in the CMOS design gives it far superior speed compared to CCD.

The Photron FASTCAM SA1.1 used in this experiment has great flexibility when it comes to resolution, exposure time and frame rate. To study soot formation during a combustion process it is desired to achieve as high frame rate as possible and as low exposure time as possible. Since the high speed system is aimed towards the combustion process in the optical engine, high frame rate and low exposure time is essential to freeze each frame to end up with a sharp image. While at the same time keeping resolution at a reasonable level. The camera sensor has an electronic shutter, as framerate increases the resolution (the number of active photodiodes) has to decrease to handle the data processing.

The initial parameters for the camera is configured to the setting in Table 5.

Parameter	Value
Frame rate	54 000 fps
Resolution	256x256 Pixels
Color mode	Grayscale
Bit depth	2^{12}
Exposure time	3.37 μ s

Table 5 Initial Camera settings

To understand how the images are analyzed it is also important to understand how the information in the image is retained. The resolution of the camera at the current settings is 256x256, as seen in Table 5. Each pixel stores the light intensity that each photodiode detected on a grayscale. In Figure 31 A) shows a random image take from one of the data series collected in the experiment. If a small section of the image is magnified, as it has been in Figure 31 B) it can clearly be observed that each pixel has a defined value. Each of these pixel values are the light intensity detected by the photodiodes on the camera sensor. To store the light intensity detected by the photodiode, bins are used to structure data. At the current settings, the Photron FASTCAM SA1.1 output each pixel value with a bit depth of 2^{12} . This means that each pixel is assigned a value from 0 to 4096, where 0 is defined as no light detected/black. The maximum value is 4096, and corresponds to white or a fully saturated pixel. As seen in the bit depth example in

Figure 31. The higher bit depth a camera has greater numbers of bins it has to store the pixel values, which will yield a higher sensitivity and level of detail as more levels are available to construct an image.

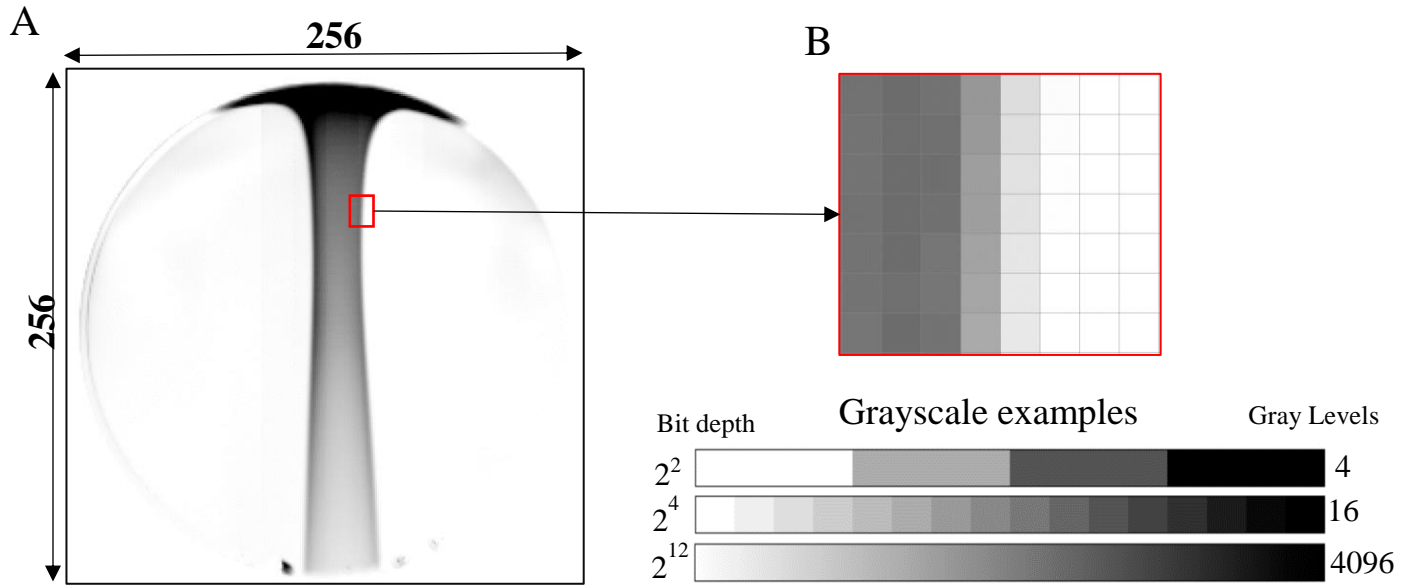


Figure 31 Building blocks of images collected by the camera.

2.5 Data Processing

To analyze the data collected in the experiment a MATLAB program is written. This section will give a short introduction to the program. The full MATLAB script written can be found in appendix A.

When the camera capture images, each image is accumulated into one large file, saved as *Tagged Image File Format* (TIFF) file. A MATLAB script is then used to load the images one by one from the TIFF stack. This is done with the MATLAB function *IMREAD*. The *IMREAD* function takes each image (k) from the series and converts each pixel value into an element in a matrix with corresponding dimensions to the image resolution. At the current settings, a 256x256 matrix is constructed for each image.

The way the data is collected each image series is collected with a sample size of 1000 images. The first 500 images are collected to establish background illumination I_0 , the following 500 images is captured with a soot rich flame present. The two events are the separated for convenient in later calculations. This is done by implementing the *IMREAD* function in a *FOR loop*. The data from the two events is separated and stores as cell arrays in the TIFF image sequence with n pictures that is imported is then stored in MATLAB as a cell array of matrices, with n number of cells. In Figure 32 the first section of the script is illustrated

```
%Input data, file path
fname = 'C:\Users\ \Prosjektoppgave\08_11_2016\example_file_path.tif'

%Get image info and number og pictures in series
info = imfinfo(fname);
num_images = numel(info);

%Inputs, decided later in the process
num_im_skip = 200;

%For loop to read images with imread one by one. And at the same time do
%statistical calulations for each frame.

num_sel_images = (num_images/2)-num_im_skip;

frame0 = cell(1,num_sel_images);      % initial image, no flame
frame = cell(1,num_sel_images);      % image with flame

for k = 1 : num_sel_images

    [emp0,map] = imread(fname, k+num_im_skip);
    [emp,map] = imread(fname,k+(num_images/2)+num_im_skip);
    frame0{1,k} = double(emp0);      %convert to from sigle 2 double to calculate avg.
    frame{1,k} = double(emp);
    temp0 = frame0{1,k};
    temp = frame{1,k};
    uavg0(k) = mean(mean(frame0{1,k}));          %Average value in each frame
    uavg(k) = mean(mean(frame{1,k}));

end
```

Figure 32 Extracted example from MATLAB script.

After the images are converted to matrixes we are free to conduct simple matrix calculations to compare images and determinate factors as the LED stability within a series of images and noise

can be calculated. As an example, the average light intensity for the images is used as a metric to compare the amount of light emitted by the LED from image to image.

In the result section, each of the parameters investigated will be discussed and corresponding data presented. Figure 33 show the work flow of the basis of the MATLAB script

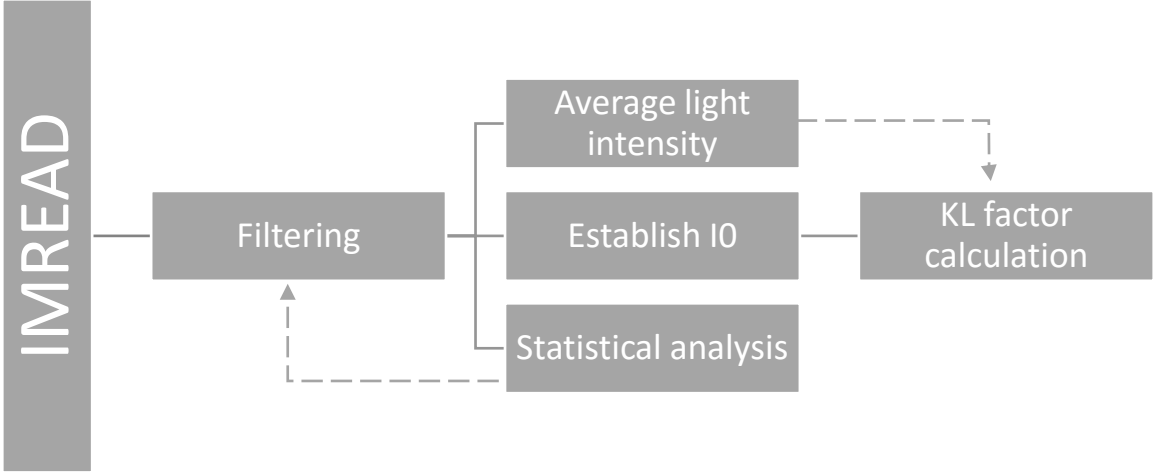


Figure 33 Illustration of work flow in MATLAB script.

2.6 Experimental Process

The goal of this experiment is to determine what configuration of the DBIEI setup will yield best results for in cylinder measurements of soot formation. Prior to this experiment initial test on the system was conducted to understand how changing the parameters affected the output image. To clarify what is emphasized as the “best output images”, it is intended to find the setting which soot can be detected and the variation between each image captured a steady state event are as equal as possible. To reduce the variation between images a key factor is to utilize the sensor range of the camera. By using more of the dynamic camera range we will increase the signal-to-noise ratio (SNR). An important factor to include to this relationship is the fact that the illumination from the flame needs to be eliminated. While trying to eliminate the flame luminosity with ND filters or adjusting the exposure time the overall light intensity of the image will be reduced. If it is needed to increase the light intensity level after finding a method to eliminate the flame, the LED gate voltage and power supply can be increased.

2.6.1 Experimental approach

Section	Variable	Process
3.1	LED behavior	Determine the LED stability within a series of images. 10 series, each consisting of 500 images is collected using initial settings for the camera. No parameters were changed between the series image series. Investigate if data quality can be increased.
3.2	ND filter	Collect image series with the different ND filter available. Analyze how they affect results, suggest a filter to use for further analysis.
3.3	Camera exposure	Investigate the three camera exposure times; 1.00us, 1.87us, 3.00us. Collect series of images at each exposure settings and compare the results, conclude on the suggested settings to use.
3.4	KL factor SNR	Collect a series of images at the settings found in the prior sections. Analyze SNR ratio within the 2D KL image.
3.5	Statistical analysis of KL factor	To determine the statistical accuracy of the KL factor 30 series of 500 images is collected to establish the variation in I_0 and I_t by using the settings found in the prior sections.

Table 6 List of experiments. [us] represents microseconds

Chapter 3 Results and Discussion

3.1 Investigation of LED Stability

In Figure 34 the average pixel value of the first 4 series consisting of 500 images each. The average pixel value is used as a metric for the stability of the illumination supplied by the LED. With the goal to determinate the stability of the background illumination across a typical image sequence. From Figure 34 it can be see that the first images in each series has consistently higher pixel values then the rest of the series. This behavior was consistent for all image series collected.

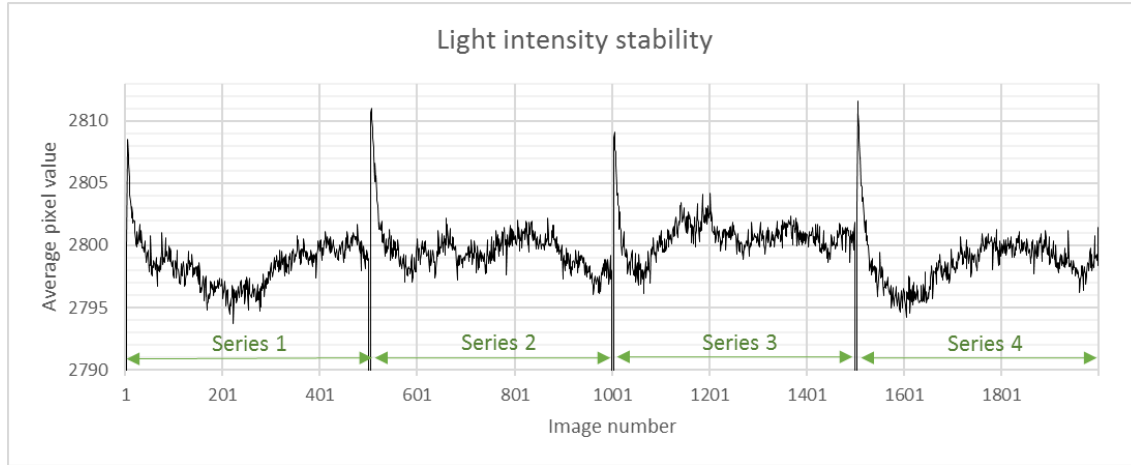


Figure 34 The black graph illustrates average pixel value for each image. The green annotated “series (n)” arrow indicated start and end of an image series.

To eliminate the spike in intensity observed at the beginning of each series, one possible solution is to filter out a specific number of images. Based on the behavior of the intensity a suggested limit is to filter out the first 200 images. Table 7 illustrates comparison between average pixel value and the standard deviation for the raw data and the statistical values after the first 200 images is filtered out.

	Raw data		Filtered data	
	μ	σ	μ	σ
series 1	2787.07	176.87	2798.36	1.70
series 2	2788.24	176.95	2799.39	1.28
series 3	2789.22	176.89	2800.69	0.76
series 4	2787.26	176.89	2799.41	1.01
Average value	2787.95	176.90	2799.46	1.19

Table 7 Average of series values and standard deviation for each series.

From Table 7 it is apparent that filtering of data will be beneficial to reduce the standard deviation. The choice to remove the first 200 images is chosen as a conservative estimate after inspection the data. The number of images to clip might be seem over conservative, but taken in consideration that it is easy to increase the number of pictures taken in a series this is suggested as a threshold of images to filter out. An alternative approach would be to filter out individual images over or under a specific threshold in light intensity. This could possibly cause image series of different

length, and extreme values from the event captured might get cut out. e.g. especially bright periods during combustion might unintentionally be filtered out.

LED behavior over a unrealistically long time sample for soot detection is collected and presented in Figure 35. The blue graph show how light intensity varies over a long continuous time sample. This sample might be unrealistically long compared to the actual length of series needed for this type of experiment.

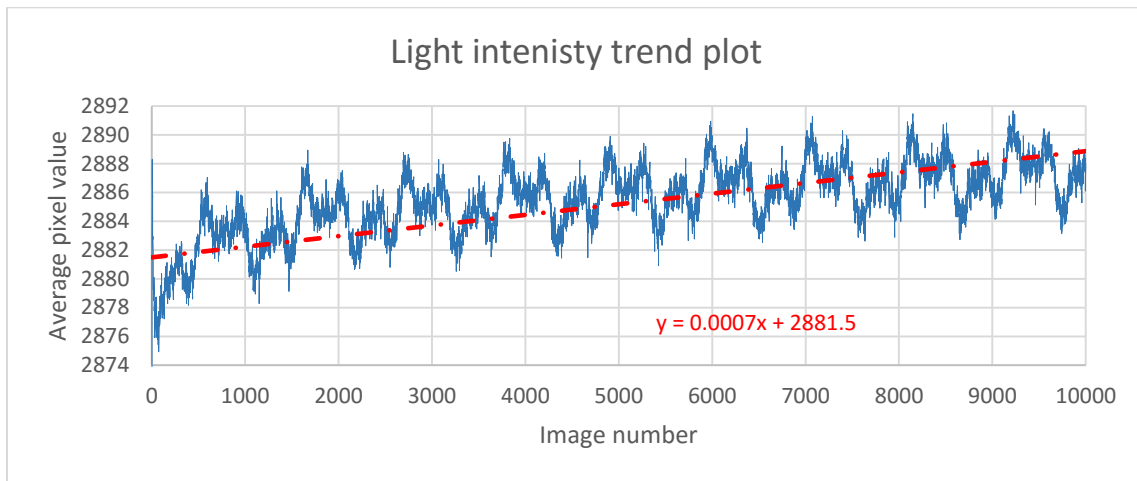


Figure 35 Continuous image series of 10 000 images. Plot show average pixel value over time.

The average pixel value varies periodically with an increasing average value. A linear expression for the increasing average is superimposed in Figure 35. The average image value appears to be a periodic pattern that repeats each 1100 frame. At 54,000 frames per second the average pixel variation corresponds to a frequency of ~49.1 Hz. The light intensity variation might be caused by the alternating current in power grid. The power in the grid in Norway is produced at 50 Hz.

3.2 Investigate NDF Impact on Light Intensity

In Figure 36 the colored lines illustrate average pixel value for a series of images for various ND filter combinations.

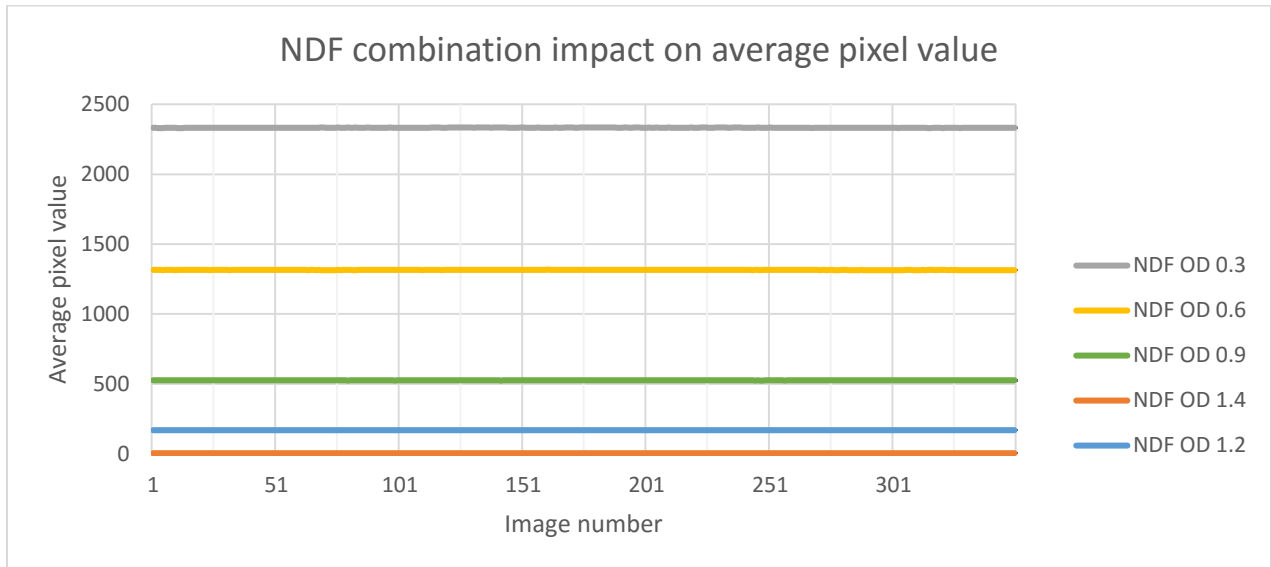


Figure 36 Plot showing average pixel value for ND filters.

From Figure 36 it is observed that light intensity is reduced proportionally with higher NDF OD numbers. This reduction in light intensity will cause the image series with high OD numbers to be recorded at the very bottom range of the camera sensor range.

Since the ND filters lowers the average pixel values in the images it is expected that the images sensors precision in recording pixel values might be affected by the change in sensor range for each ND filter. To investigate the uncertainty at the different ND filter combinations the uncertainty impact of each filter is presented relative to the percentage 2σ corresponds to the average for the image series. The resulting plot is seen on the next page.

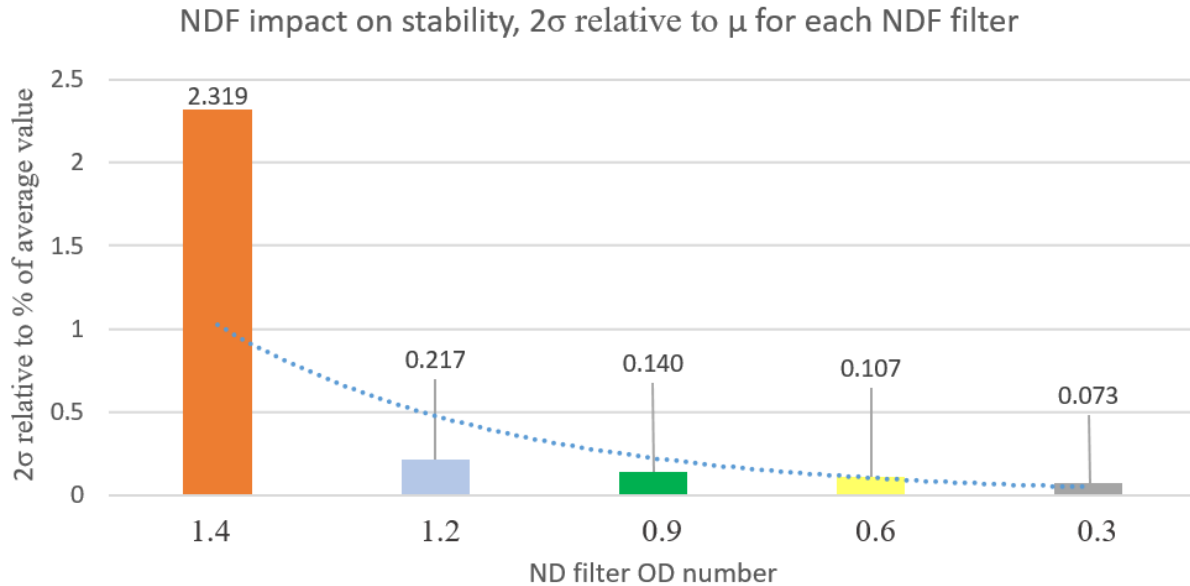


Figure 37 variation for each of the ND filters are given relative to, how many percentage two sigma impacts relative of the average for the image series.

In Figure 37 the uncertainty detected at each image series is presented. It can be seen that by operating at the low range of the image sensor the uncertainty in the images and hence the variation between pictures capturing the same event will increase.

From Figure 37 it can also be seen that the range of the camera sensor is proven to be relatively wide. This means that the camera is precise even at relatively low light exposure. The standard deviations relative size decreases rapidly and converges as saturation increases

From the data collected it is suggested that ND filters from OD 0.3 to OD 1.0 can be used and will yield relatively stable results. However, it is also seen that lower OD number is desired and to obtain the best results, hence for this experiment it is suggested to proceed with ND filter at OD 0.3.

If higher OD number is required for the actual experiment is it valuable to know the camera precision at various exposure levels as seen in Figure 37. If ND filters with OD numbers above 1.4 needed, the LED system needs to be modified to obtain higher light intensity and conserve accuracy in the experiments.

3.3 Exposure Comparison

Before comparing the different exposure times some modification of the system is required. At the current configuration, the 1 μ s exposure cannot be used because the delay from the camera output signal until the LED is illuminated is almost long as the exposure time itself. Without modifying the system images sampled at 1 μ s exposure will merely receive any light from the LED at all. Figure 38 illustrates the LED light intensity, the blue signal represents the camera exposure and the green signal represents the light intensity.

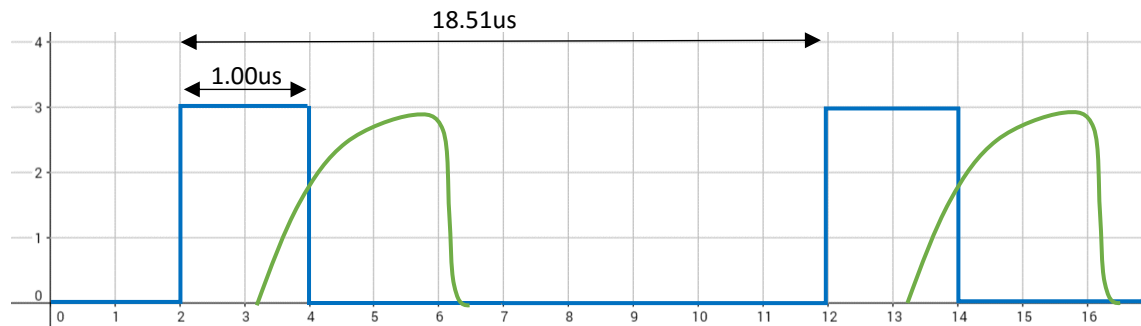


Figure 38 LED exposure and light intensity from the LED over time. Signals are adjusted to fit in one illustration sizes are not to a definitive scale.

To solve this problem a possible solution is to add a delay to the output signal for the camera exposure. The result will be that a preceding image in the series triggers the LED to illuminate the next image in the series. Thus, the first image in the series will be dark. But the consecutive image in the series will be sufficiently illuminated. As the first images in each series if filtered out this is considered a working fix. Figure 39 illustrates how the signal delay can be applied to achieve illuminated images at 1 μ s exposure time.

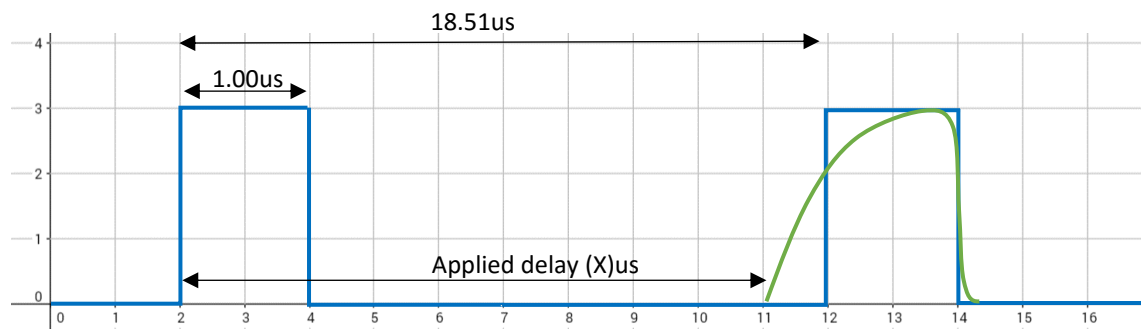


Figure 39 LED exposure and light intensity from the LED over time. It is show how a delay can be added to the output of the camera exposure to maximize the light intensity in the next images. The Signals are adjusted to fit in one illustration sizes are not to a definitive scale.

From an oscilloscope and a photodiode, the inherit signal delay between the camera exposure and until the LED was measured to be in the range around 0.2-0.4 μ s. This served as a starting point for a more precise series of data collected with the camera to determinate the signal delay that would

give the best results. A signal delay sweep from 17.5 μ s to 18.1 μ s at increments of 0.1 μ s was applied to the camera exposure that is used to trigger the LED. The signal delay is added in through the camera interface. The result from the signal delay sweep is presented in Figure 40.

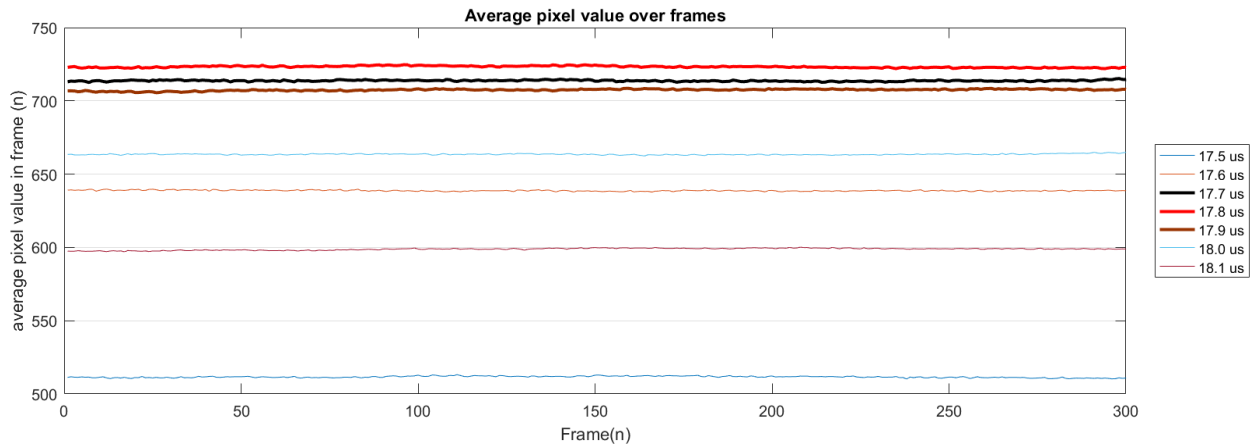


Figure 40 Signal delay sweep. The average pixel value vs image number in a series.

It is desired to find the delay which ensures that the LED illumination and the exposure occur at the same time as seen in the example in Figure 39. To measure where the two curves intersect, the average light intensity is used as a metric. From the signal delay sweep test in Figure 40 the signal delay which yields the brightest image which occur if a delay of 17.8 μ s is applied, as indicated by the red line in the Figure 40. A signal delay of 17.8 μ s will therefore be applied to the exposure output from the camera for all images taken at 1.00 μ s exposure.

3.3 Flame Illumination at Different Exposure Time

In this section the flame illumination's impact on the resulting images is investigated. It is expected that longer exposure time will allow for accumulation of more photons in each pixel and result in a higher output value. This was investigated by collecting 3 series of 300 images at each of the possible camera exposures; 1.00 μ s, 1.87 μ s and 3.37 μ s. No ND filter was used on the current configuration. The LED is not activated since we only want the illumination from the flame detected in the images. The Bunsen burner using propane as fuel served as steady state laminar diffusion flame. All parameters except the exposure where held at the same settings for the 3 series. The results from the 3 series is presented in Figure 41.

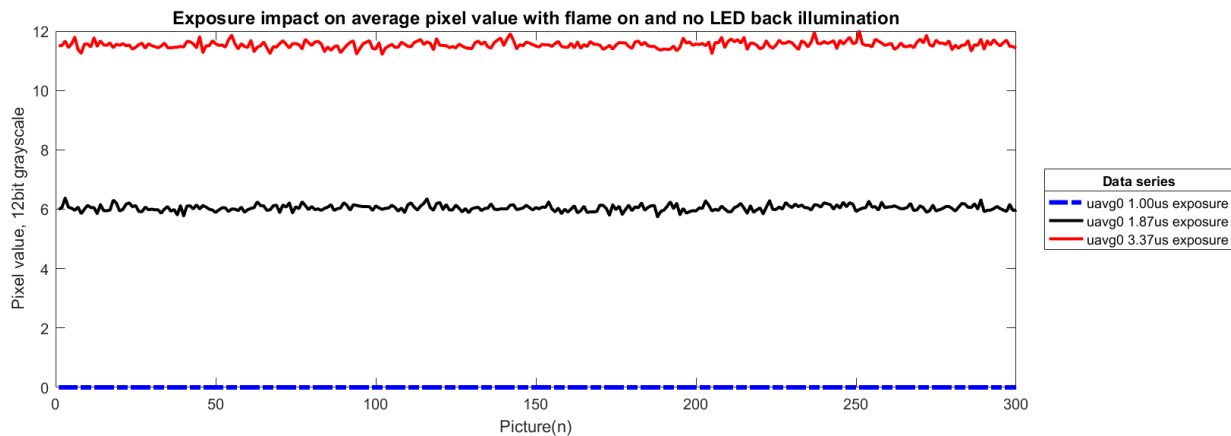


Figure 41 Flame impact at different exposure levels

From Figure 41 it can be seen that reducing the exposure time will significantly reduce the flame's impact on the resulting images. At the shortest exposure at 1 μ s the average pixel value from the series is exactly equal to zero for all images in the series. This was confirmed by collecting several separate images series and the result where the same. To obtain high quality images where the flames effect on the images is limited as much as possible, the shortest exposure time is highly recommended.

3.4 KL Map and Signal-to-Noise Ratio

From the settings found in the first part of the experiment, one images series of 500 images with the LED on was collected to establish I_0 . Then another 500 images with both LED and the flame present was collected to establish I_t . The settings used are the configuration suggested in the prior sections. ND filter: OD 0.3. The first 200 images are filtered out in post-processing of the data.

The expression for the KL factor with respect to I_0 and I_t is presented in equation (2.1), as introduced in equation (1.3). For a 2-D KL map I_0 is calculated as the average background image created with the LED activated and the flame absent. I_t is defined as the instantaneously light intensity for each picture captured in the second series with both the flame and LED present. I_t is not calculated as the average over the image series because the final goal of the rig is to have time resolved KL factor during the combustion process.

$$KL = -\ln\left(\frac{I_t}{I_0}\right) \quad (2.1)$$

The resulting 2-D KL map is shown in Figure 42. The KL ratio is plotted on a scale where 0.0 equals black and 0.4 is white. The I_t image used to create Figure 42 is a random image number from a series of images after the first 200 images is filtered out. Image series used for further KL factor estimation was collected on 08/11-2016. The image sequence used can be found in the digital appendix¹. Image number 36 in the I_t series is used for KL illustration.

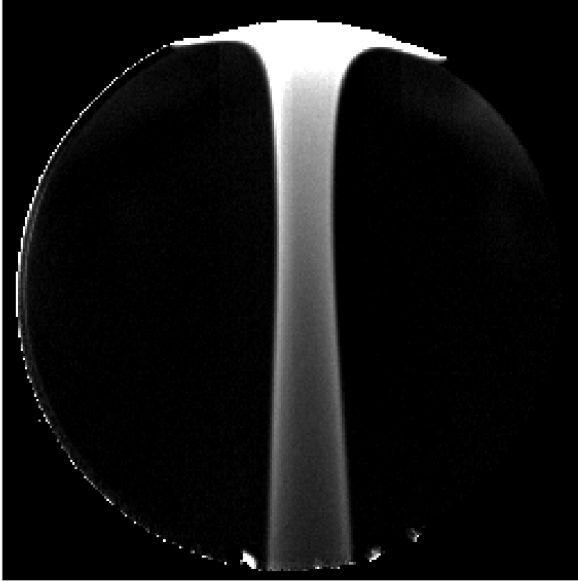


Figure 42, 2-D KL factor map Plotted scale where 0=black and 0.4=white

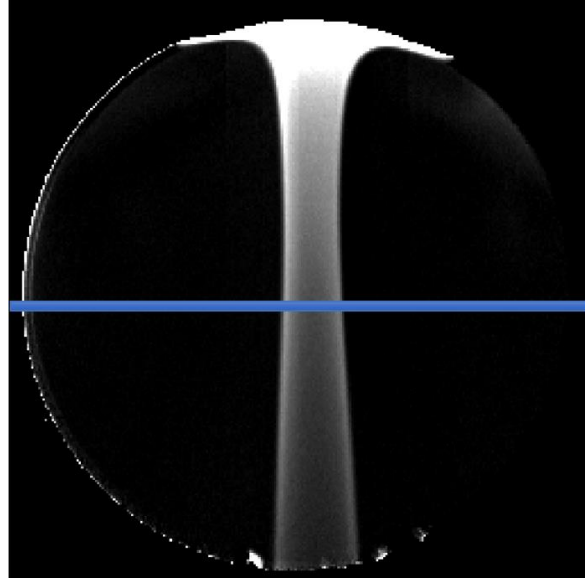


Figure 43 Same as Figure 42, blue bar illustrates how pixel values across the center used in further calculation

From Figure 42 it can be seen that the KL factor is higher in the soot rich region of the diffusion flame. At the top of the image the KL factor is increasingly high as the soot is deposited where flame collide with the cylinder top. Carbon particles that has fallen from the cylinder top can also be seen in the bottom of the image. The white halo seen is most likely due to the hot gas escaping the cylinder through the circular inspection holes.

A representation of the signal to noise ratio in the KL factor in a specific image can be found by extracting the pixel values across the center of the image. The center of the image is chosen because the KL factor in the region is representative for the average KL factor in the flame. The goal is to obtain the ratio between the noise in the background and the actual impact soot has on the KL factor. This is done by extracting the pixel values across the center of the image. This is illustrated by the blue bar in Figure 43. By plotting the KL factor versus pixel position from left in the image equals to 0 and the right edge of the image where pixel number equals to 256, the KL factor across the center of the image is plotted in Figure 44.

¹ Filename: flame_LED_exp1us_NDF_OD03_f14_15V_Gate4_8V_flame in_center.tif
This file is the TIFF sequence used illustrate KL factor across the image in Figure 42 and Figure 43.

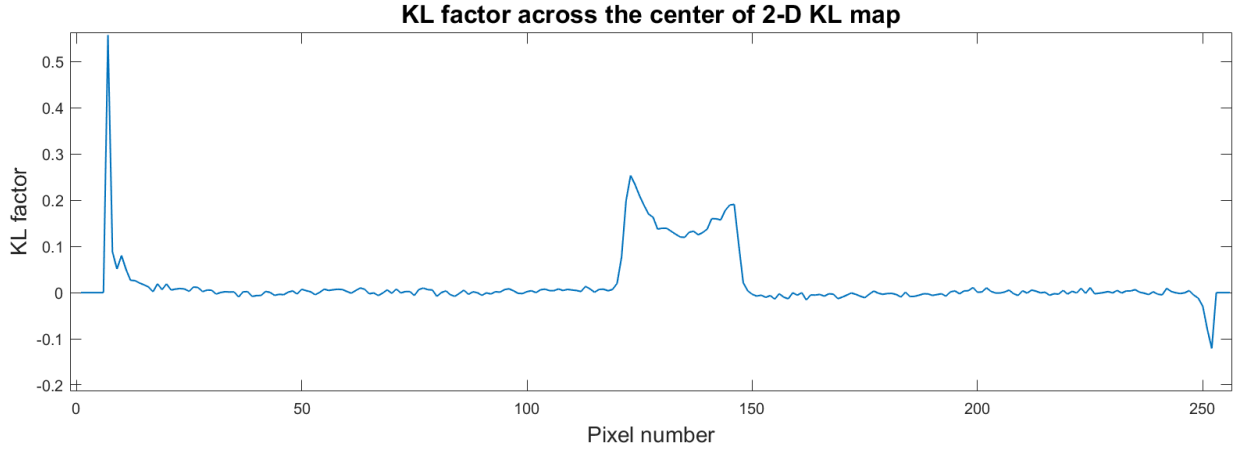


Figure 44, KL factor from extracted pixel values across the center of Figure 43

To quantify signal to noise ratio across the center of the KL plot. The average value of the pixels from 20 to 115 is calculated as a representative region for the background noise. The average value of the signal is calculated as the average value from frame 122 to frame 147. The extracted regions are illustrated in Figure 45.

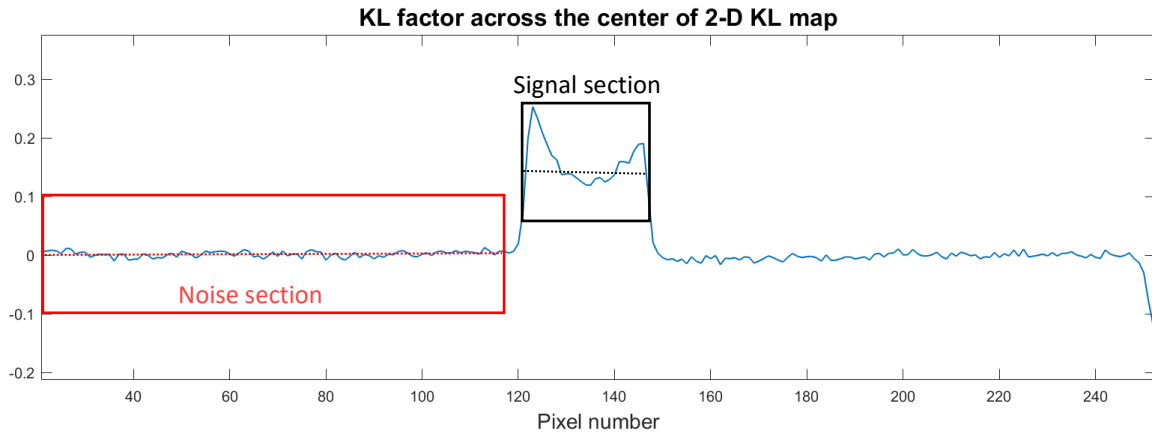


Figure 45 KL factor from extracted frame across center of image. On the figure section used for calculation of background noise and signal is annotated. The dashed lines illustrate the average value in each section.

The signal to noise ratio is calculated from the standard deviation in the noise section, given the notation σ_{noise} . It is assumed that this is the noise found in the noise region is representative for the noise across the whole array. The average signal is assigned μ_{signal} . The signal to noise ratio (SNR) within the image is described by equation (2.2). To calculate SNR, the values for σ_{noise} and μ_{signal} are calculated in MATLAB as the average for each section., where $\sigma_{\text{noise}} = 0.0047$ and $\mu_{\text{signal}} = 0.1571$. With these values inserted in equation (2.2), the $\text{SNR}=33.5575$

$$\text{SNR} = \frac{\mu_{\text{signal}}}{\sigma_{\text{noise}}} \quad (2.2)$$

From the specific image in Figure 42 used to illustrate the 2-D KL map, the signal to noise ratio is approximately 33.6. This signal to noise ratio appear to be at a satisfactory level to distinguish between the signal and the noise. According to the old Rose criterion images needs at least signal to noise ratio equal to 5 or higher to differentiate signal from noise [34]. Furthermore, in accordance to ISO 12232, standard for determination image quality suggest that SNR ratio of 10 corresponds to acceptable image quality. And SNR of 40 corresponds to excellent image quality [30]. With these two arguments in mind the image quality seems to be good.

3.5 From the Results in 3.1 and 3.2 Suggestion on Procedure and Filter Combination.

From the suggested configuration found in the previous sections of this experiment 30 Images series of 500 images are collected. The suggested ND filter to use is OD 0.3 and the first 200 images are filtered out in post-processing of the data.

As seen in equation (2.3) the KL factor dependent on two measured values, the two terms adding uncertainty to the KL factor are I_t and I_0 . From the data series collect uncertainty in both factors are calculated. The error in I_0 is affected by the varying tendency of average pixel value for each series. I_0 calculated as the standard deviation of the average pixel value of these 30 samples. I_0 can be visualized as the precision in the system's ability to detect the same average for each image series. Within each series uncertainty in I_t is established by calculating the average standard deviation inside each series.

Symbol	Value
μ_{I_0}	2 788.31
σ_{I_0}	8.51
σ_{I_t}	1.25

Table 8 Uncertainty elements in KL factor

According the to the propagation of error formula the combined uncertainty in KL factor can be calculated from (2.3)

$$S = \sqrt{\left(\frac{\partial f}{\partial x}\right)^2 s_x^2 + \left(\frac{\partial f}{\partial y}\right)^2 s_y^2} \quad (2.3)$$

To calculate the standard deviation of the KL factor for a 95.45% confidence interval, then the following values can be used in the calculation; $\partial I_t = 2\sigma_{I_t}$ and $\partial I_0 = 2\sigma_{I_0}$

$$S_{KL} = \sqrt{\left(\frac{\partial(KL)}{\partial(I_t)}\right)^2 \partial I_t^2 + \left(\frac{\partial(KL)}{\partial(I_o)}\right)^2 \partial I_o^2} \quad (2.4)$$

$$S_{KL} = \sqrt{\left(-\frac{1}{I_t}\right)^2 \partial I_t^2 + \left(\frac{1}{I_o}\right)^2 \partial I_o^2} \quad (2.5)$$

$$S_{KL} = \sqrt{\left(-\frac{1}{2698.79}\right)^2 2.49^2 + \left(\frac{1}{2788.31}\right)^2 17.02^2} \quad (2.6)$$

$$S_{KL} = 0.00617 \quad (2.7)$$

From a steady laminar diffusion propane flame from the Bunsen burner the average KL factor in the flame is estimated at ~0.15 from the plot in Figure 45. The KL factor can then be present with ± 0.00617 as found from the calculations of propagation of error. At the current confidence interval, the uncertainty in the KL factor is 4.1% of the signal. If the KL factor is assumed to be around 0.15 with the same optical setup as above the KL factor can be present in the following way; $KL = 0.15000 \pm 0.00617$, at 2σ confidence interval.

The KL factor used in the example is calculated for a propane flame. When the experimental setup is used for the intended purpose KL factors for a diffusion Diesel flame it is expected to be between 0.8 and 1.3 [16]. This will result in a smaller error % relative to the signal.

3.6 Conclusion on Soot Detection Ability

The optical system with the camera and LED used for back illumination is a relatively complex system. Many variables can be changed to manipulate the output images. From the experiment conducted the following procedures are suggested:

- Filter out the first 200 images from each image series collected
- ND filters used at the current LED settings is suggested to be at OD equal to 1 or below, preferably the lowest number OD number that sufficiently eliminates the flame.
- One microsecond camera exposure with 17,8 microsecond delay added to the LED trigger signal is suggested to eliminate the flame luminosity and to freeze event captured and obtain clearer images.

With the settings above that the signal to noise ratio for an KL image is around 33.6 in an arbitrary soot rich propane flame. The same propane flame yields a KL factor in the soot rich section of the flame of; $KL=0.15000 \pm 0.00617$ at 2σ confidence interval. The uncertainty of $\pm 4.1\%$ in the KL factor seems to be in a reasonable range. A 2013 study by Manin et al. [26] reported uncertainty in KL factor to be below 10% using a similar measurement method.

Chapter 4 Engine Tests and Thermal Characteristics

4.1 Heat Transfer in Perspective

In compression ignition engines, thermal management is critical for stable operation. The temperature of the engine affects emissions, performance, and efficiency. During the combustion phase, the chamber walls experience heat flux that can reach ten megawatts per square meter. [5] During the non-reactive periods of the cycle there is essentially zero heat flux to the walls. This high intensity localized energy transfer can cause fatigue-cracking on chamber walls and piston. Poor thermal management is detrimental for an engine and will lead to an array of problems and eventually breakdown. For convention engines, a rule of thumb for engine design is to keep cast iron components below 400degC, and keep the cylinder sleeve below 180degC to prevent deterioration of the lubricant oil film.

The engine used in this study with an optical combustion chamber will not require cooling but heating. The engine is driven by an electrical motor, and the intent of the engine is to only observe isolated single combustions cycles with high speed images of the combustion event. Proper heating of the engine is crucial to ensure sufficient conditions in the chamber for combustion of the fuel in the chamber. The following sections will give an insight to the modes of heat transfer in a conventional 4 stroke CI engine

4.2 Heat Transfer Modes

4.2.1 Convection

Heat transfer between a fluid and a solid due to relative motion. Convection is conveyed in either two methods; either driven by gravity or forced convection driven by an external force. In a naturally aspirated engine, we have forced convection due to the pressure difference created by the rapidly moving piston. The convectonal heat transfer will continue through the engine wherever the turbulent air and gas interact with engine components. (Intake manifold, valves, cylinder, piston, and chamber wall.)

4.2.2 Conduction

Heat transferred by molecular motion in fluids and solids in static conditions, due to an internal energy gradient in the medium. Fourier's law defines heat transfer by conduction defined in equation (1.1).

$$\dot{q} = -k\nabla T \quad (1.1)$$

Where \dot{q} is the heat flux density, ∇T is temperature gradient and k is conductivity of the material.

4.2.3 Radiation

Unlike convection and conduction, radiation occurs through the absorption and emission of electrons through electromagnetic waves. In an engine, the radiative heat transfer is usually separated into two section. First radiation high temperature burned gas and radiation from the soot

particles conceived in the combustion process. In a CI engine heat energy transfer from to radiation is significantly larger than in a SI engine. Since the combustion temperature is higher.

4.2.4 Heat Transfer Process

Figure 46 illustrates the heat transfer profile from the gasses in a combustion chamber. The heat flux from the gas to the wall is driven by radiation and convection. Through the combustion chamber wall the heat flux is conducted through the metal. Then the heat flux is convected to the cooling liquid.

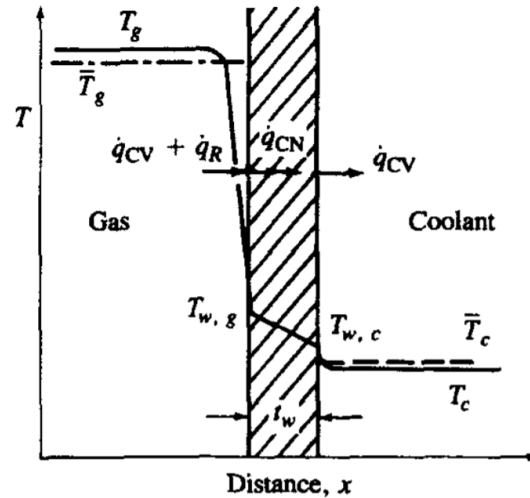


Figure 46 Temperature profile across combustion chamber, from gas to cooling liquid. Illustration 12.1 from the book "Internal Combustion Engines" by John B. Heywood

In Figure 46 the temperature profile across the heat transfer process indicated by T with subscript g for gas, w for wall and c for coolant. Overlined values indicate averaged values through the combustion process. \dot{q}_{CV} , \dot{q}_{CN} and \dot{q}_R indicate heat flux driving modes of heat transfer at heat position respectively; convection, conduction, and radiation.

To illustrate the heat flux through at various crank angle degrees Figure 47 represents radiant flux, radiant temperature, and heat release rate vs crank angle degree for various equivalence ratio, fuel/air ratio. From Figure 47 it is apparent that the highest radiant flux occurs at the peak of combustion. It can also be seen that at higher fuel/air ratio release more heat as could be expected.

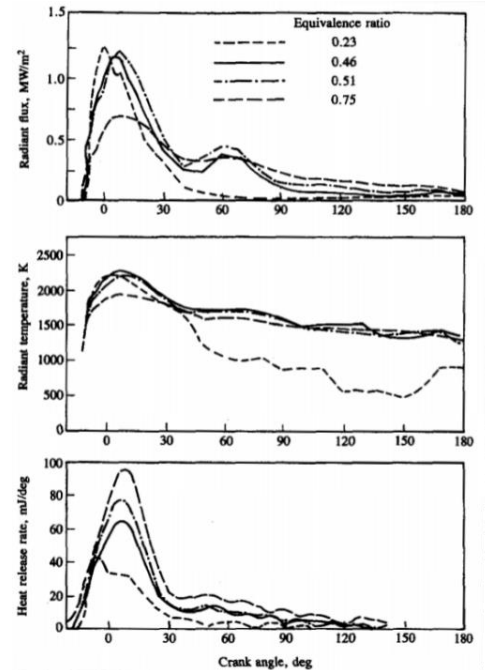


Figure 47 Illustration radiant flux, radiant temperature, and heat release rate vs crank angle degree for various equivalence ratios.

4.3 Heating System in The Engine Rig

The engine is currently equipped with several heating elements. Figure 48 shows a CAD model of the engine. The engine head block is transparent in this illustration to show the internal components of the engine head assembly. The two aluminum cylinders in Figure 48 annotated with *H1* and *H2* are heating blocks used for preheating the engine prior to experiments. The cylinder sleeve originally had a cooling system that is now modified to be used for heating. There are several heating elements mounted in the cylinder liner annotated as *H4*, in Figure 48.

In order improve the condition to achieve combustion a heating element is mounted in the airflow downstream of *H3* in Figure 48 .

The two heating options that is accessible under operation of the engine is the inlet air heater (*H3*) and cylinder sleeve heater (*H4*). Each heating elements is accompanied with one or more strategically placed temperature sensors. The heating elements are controlled with PID controller in the LabVIEW using the temperature sensor data as set-points and the duty cycle/effect as an input parameter.

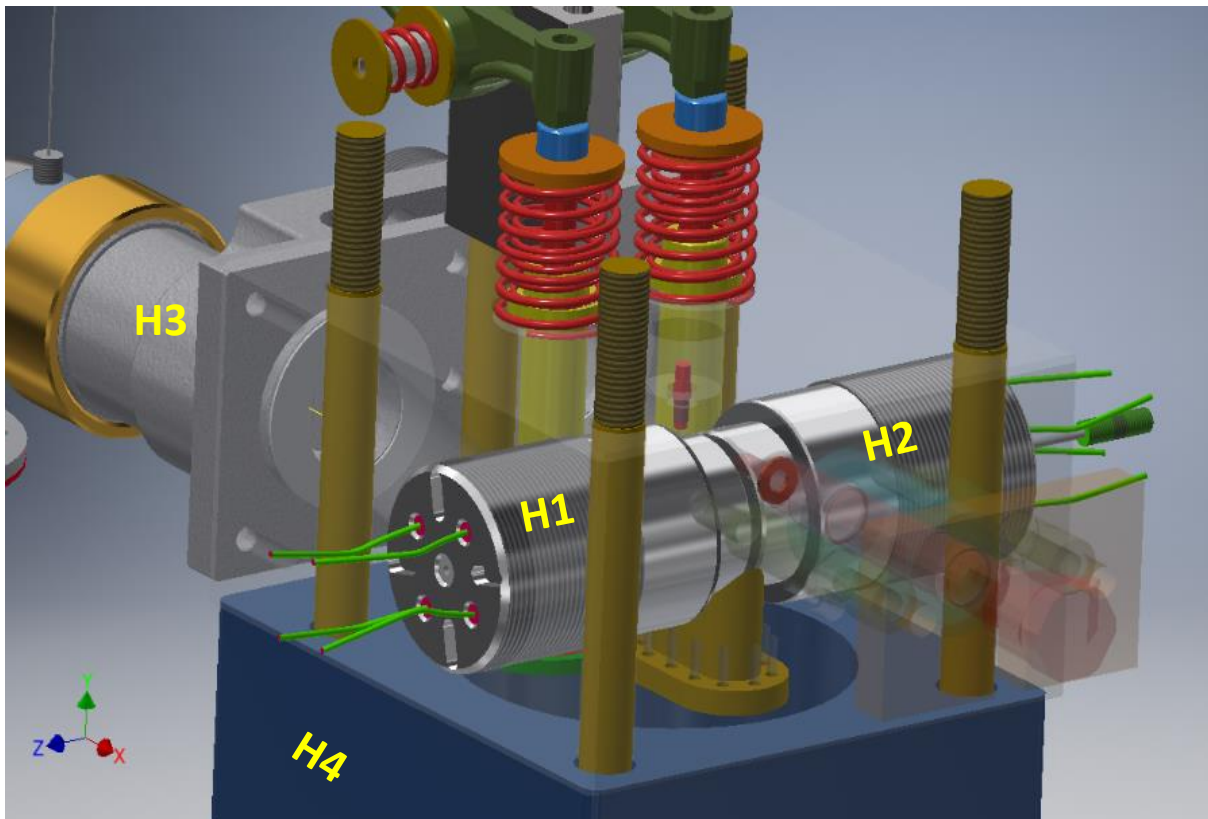


Figure 48 Transparent engine head from CAD environment showing heating elements for pre-heating the head assembly. Heating elements are marked H1-H4

4.4 Temperature Sensors

To monitor the thermal characteristics of the engine rig, several thermocouples are strategically placed. As mentioned in the section above, the temperature sensors are used for both monitoring and as *reference points* for the PID controlled heating elements. In Figure 49 the position of each temperature sensor is described. Figure 50 gives a zoomed in view of thermocouple A to C. The yellow rings in Figure 50 indicates the endpoints of thermocouple A to C

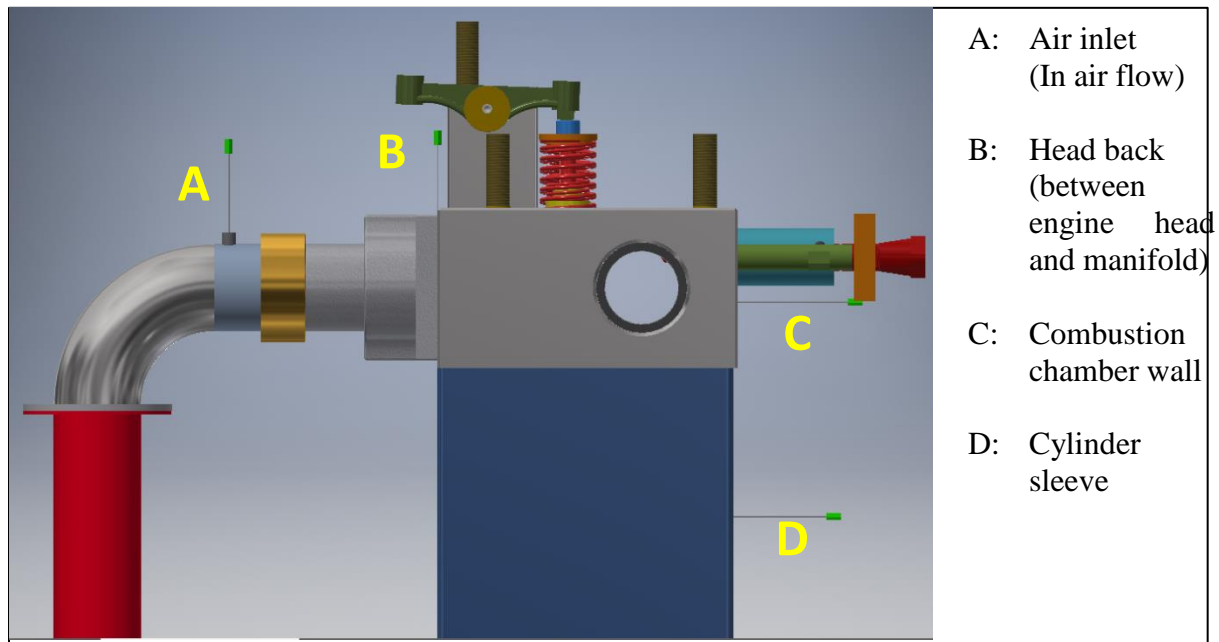


Figure 49 Side view of engine showing the relative position of each temperature sensor on the engine assembly.

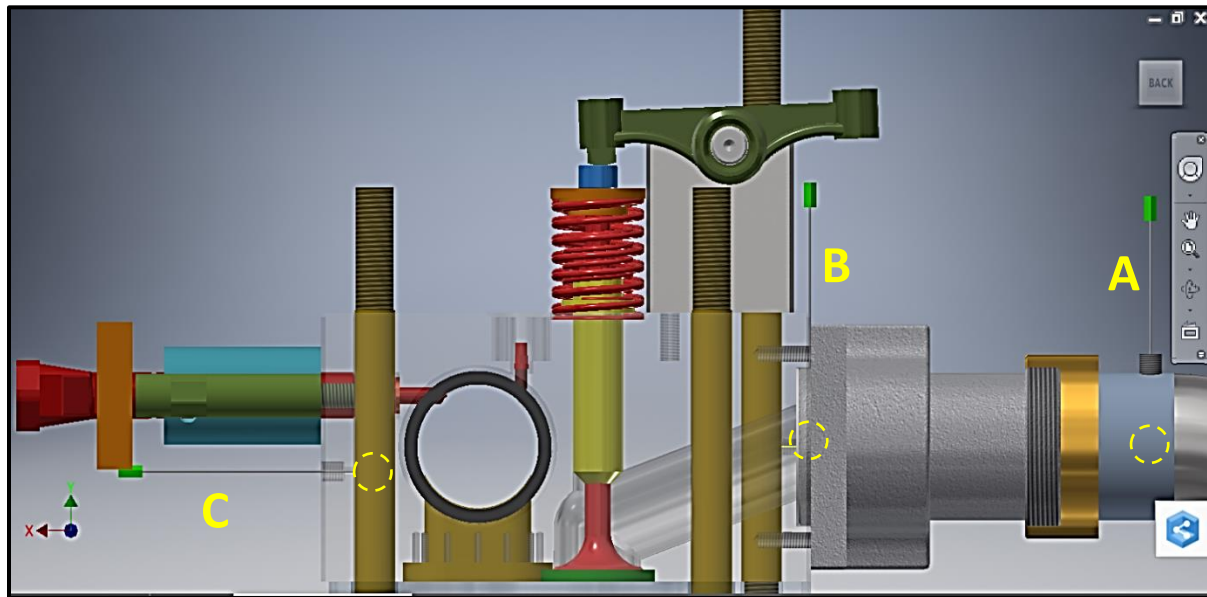


Figure 50 Zoomed in version of engine head assembly and temperature sensor position

4.5 Overview of Engine Testing

The following tests was conducted to better understand the characteristics of the engine rig.

1. Running engine test
 - a. Investigate minimum window torque required to retain pressure in the combustion chamber.
 - i. Conduct engine tests with window retainer tightening torque sweeping from 5-24NM.
 - ii. Determinate minimum torque that seal the chamber.
 - b. Temperature and pressure behavior from engine running 4 minutes
 - i. Start points for running tests:
 1. ~25°C
 2. ~60°C
 3. ~100°C
 - ii. Present temperature trend over 4-minute run
 - iii. Present pressure plot from sample recorded at the end of the run
 - c. Inlet air heater ON, recreate experiment 1B: temperature and pressure behavior from engine running 4 minutes
 - i. Start points for running tests:
 1. ~25°C
 2. ~60°C
 3. ~100°C
 - ii. Present temperature trend over 4-minute run
 - iii. Present pressure plot from sample recorded at the end of the run
2. Non-running engine test
 - a. Heat the engine from cold conditions only by heating elements
 - i. By only using heating elements find setting to reach 200°C in the combustion chamber
 - b. Engine cooling curve
 - i. Turn heating elements off and record cooling curve.

4.6 Engine Sensor Data Analysis

The data is collected following the process flow is illustrated in Figure 51. The sensor on the engine rig is connected to a data acquisition system and forwarded to system control computer running LabVIEW to control the whole system.

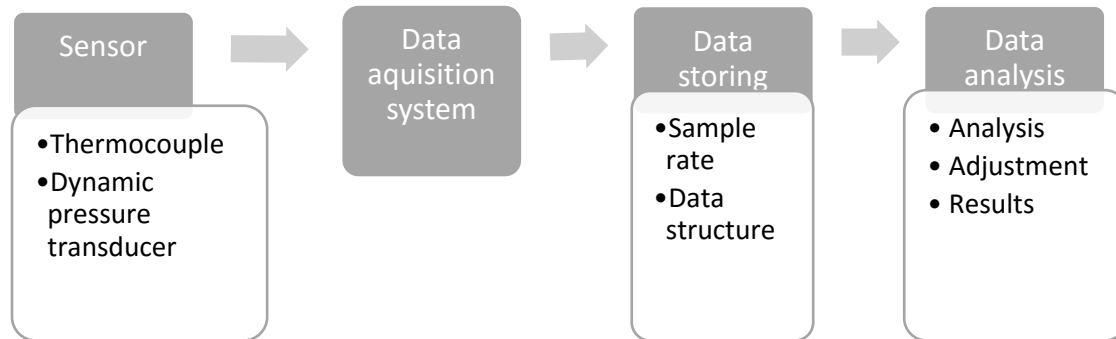


Figure 51 Data collection process flow.

To ensure that the size of the collected data stay in a usable range, data logging has been separated into two categories: high speed (HS), which has been set a sampling rate of to 100000 Hz, and low speed (LS) at 500ms. From LabVIEW, all of the data from a session is logged in one TDMS file. For further data processing and analysis, the TDMS data is imported to MATLAB.

4.6.1 Data Analysis Overview

The following sections will give a description on a suggested MATLAB processing procedure to analyze the pressure data. In Figure 52 an overview of the data work flow is given. First the pressure data is adjusted and each compression cycle is isolated by locating the pressure peaks. Incomplete pressure vectors are filtered out and the pressure data is offset on the y-axis to represent absolute values. Each individual pressure curve is fitted with a smoothing function and the average pressure plot for the data sample is created. At last a statistical analysis of the uncertainty in the average pressure plot is presented.

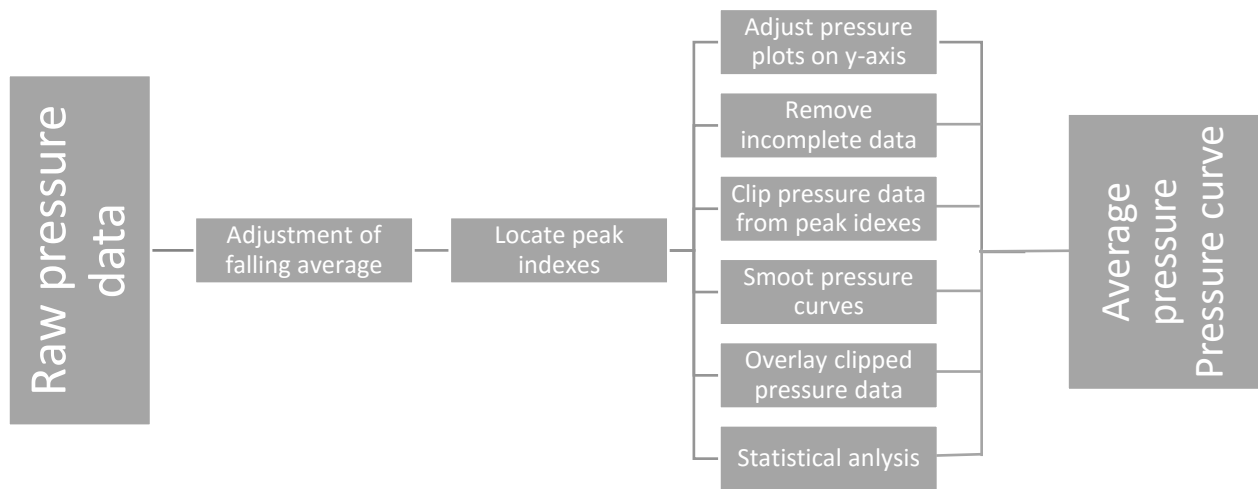


Figure 52 Data analysis simplified work flow.

4.6.2 Raw Pressure Data

The imported raw pressure data is stored as a vector containing all pressure values for a sampled data series. In Figure 53 a vector containing a series of high speed pressure data is plotted as the blue line. The goal of this data analysis is to create an accurate average pressure profile for the given conditions using data series collected. The desire to create an average pressure plot for a given condition is motivated by the variation observed between each compression cycle. The peak pressure in the combustion chamber varies for each cycle, this effect can be seen in Figure 54 on the next page. The variation in peak pressures is most likely due to small changes in the speed of the compression which is controlled by the dynamometer powering the engine rig. Other factors as hysteresis and natural variation in the chamber pressure are affecting the peak pressure as well. To compare data across datasets with varying conditions it is important to have confidence and quantify the quality of the data. To mitigate the variation inside each data, sample the average pressure plot is a valuable representation.

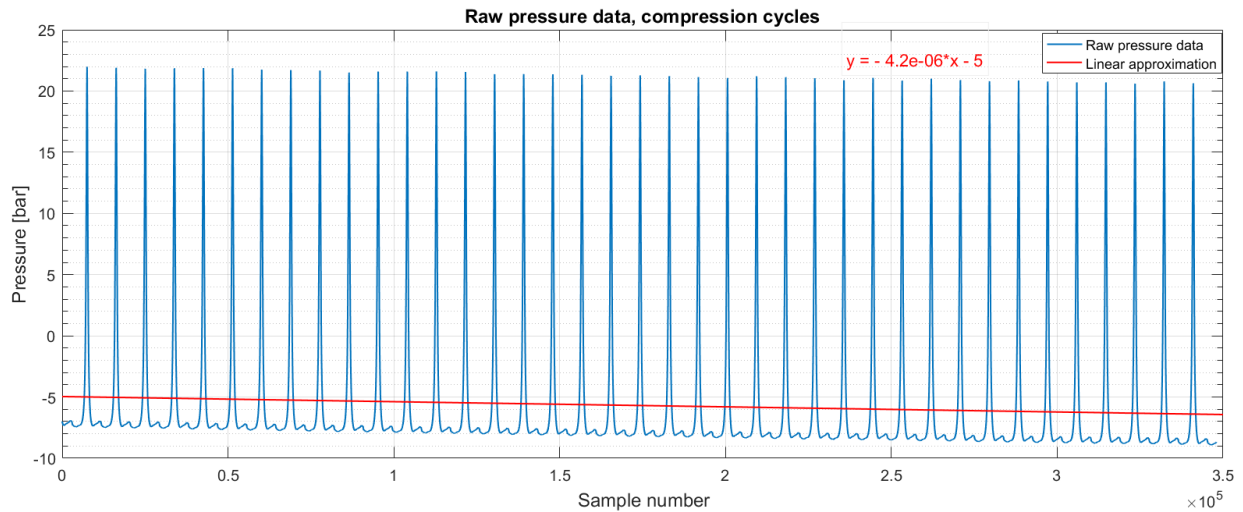


Figure 53 Raw pressure data plotted in MATLAB with a blue line.

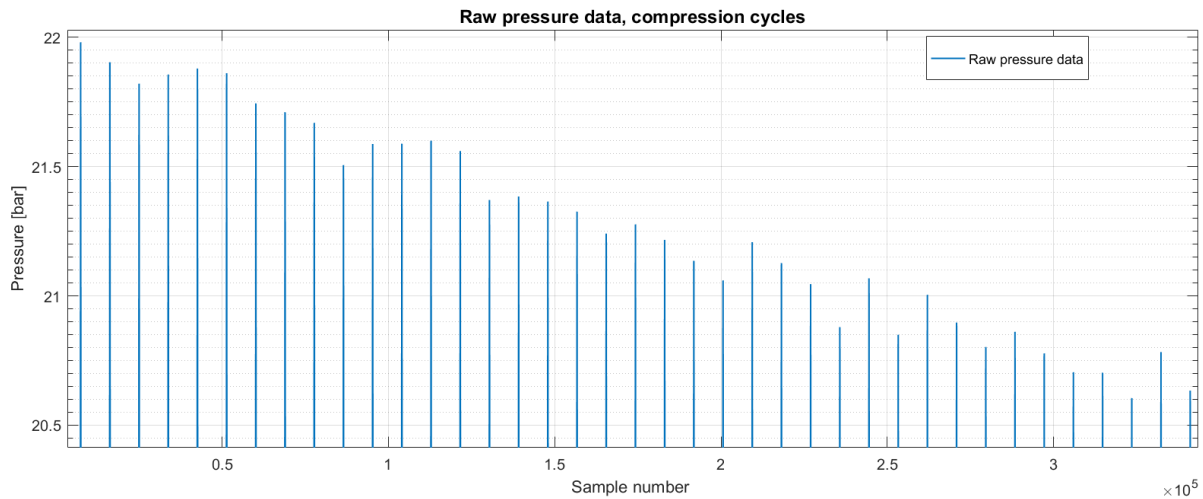


Figure 54 Raw pressure data, same as showed in Figure 53 but zoomed in around pressure peaks to illustrate the variation

The Kistler pressure sensor used is intended for dynamic pressure measurements. From the dynamic sensor, it is assumed that relative values in a compression cycle are comparative representation of the pressure inside the cylinder. E.g. one pressure measurement cycle can be compared with any of the other cycles within the same data series given that the conditions are the same and that the data is normalized. Based on the following assumptions a MATLAB script is written to adjust, analyze, and create an average pressure curve for the data seen in Figure 53. The data analysis script can be found in full text in appendix D.

4.6.3 Data Adjustment

To straighten out the falling average trend of the raw data shown with the red line in Figure 53, a POLYFIT function is used to create a linear approximation of the pressure plot, and extract the descriptive coefficients A and B. To adjust the actual pressure data a for loop is utilized to adjust each pressure value with the A and B. Figure 55 shows how this is done in the script.

```
p = polyfit(time_vector,pressure,1);
%From polyfit extracted variables: Y=Ax+B
A=p(1,1);
B=p(1,2);
%center y axis adjustment
for f = 1 : length;
pressure_adjusted(f,1)=(pressure(f,1))+(-A*f)+(-B+0);
end
```

Figure 55 Extracted MATLAB script for adjustment of decreasing average.

4.6.4 Average Pressure Plot

While creating the average pressure plot many methods can be used. A stable reference point is needed to correctly place the pressure curves to establish the average value. The initial plan for the experimental rig was to use a high-speed shaft encoder to track the engine output shaft position and thereby know the exact piston position during the compression cycle. Two such sensors were broken under installation and rendered this method unavailable. The pressure response in the chamber measured by the sensor is a direct response the change in volume caused by the piston travel in the engine. The maximum pressure in the engine without combustion will be recorded when the piston is at top dead center. This characteristic is used as the reference point to extract and align the pressure data. Each pressure peak is found using the function “findpeaks” where a prominence factor of two is used and a smoothing function is used increase the chance of extracting the true peak value. The function returns the peak values and the corresponding vector indexes. The location of the peak values is then used to extract each pressure cycle and create a new variable containing each cycle as a vector in a matrix. In the code incomplete vector and zero values are removed to avoid errors in the script. Another considerable concern before creating the average pressure curve is to ensure that all of the pressure vectors are placed correctly on the Y axis. In other words that the pressure plots are located at the correct position to indicate absolute pressure. This is achieved by finding another consistent reference point.

Promptly before the intake valve closes the pressure converges before there is a relative distinct jump in pressure when the valve closes. In order to establish a reference value 260 Y values prior to inlet valve closing are used to establish an average pressure promptly before intake valve closing. Figure 56 show the reference data marked as Ref. data in black text and inlet valve closing in blue. The figures show a plot where all of the isolated pressure vectors are plotted in the same figure. Note that the data in Figure 56 is not yet correctly placed on the y axis. It is assumed that right before inlet valve closing there is equilibrium between chamber and ambient air, and therefore the absolute pressure is considered 1 bar at inlet valve closing.

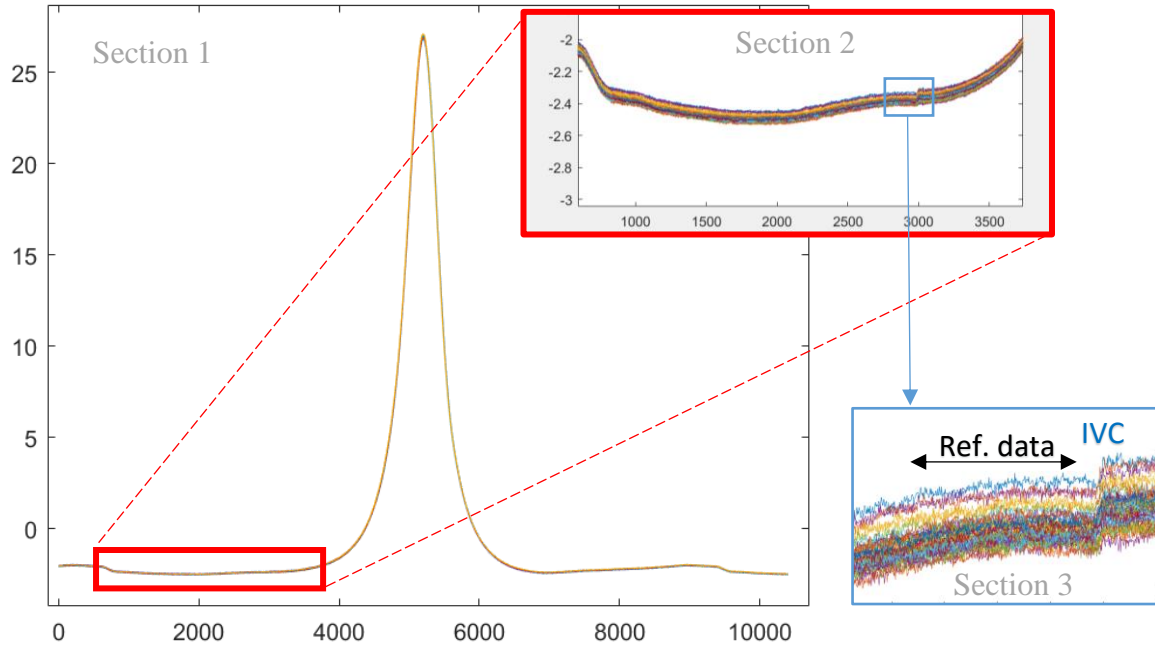


Figure 56 Illustration showing reference point (IVC) on pressure plots used offset the pressure data on the Y axis.

After adjusting each pressure plot according to the method describe above, and setting the reference pressure to 1 bar and the inlet valve closing the result is the data presented in Figure 57

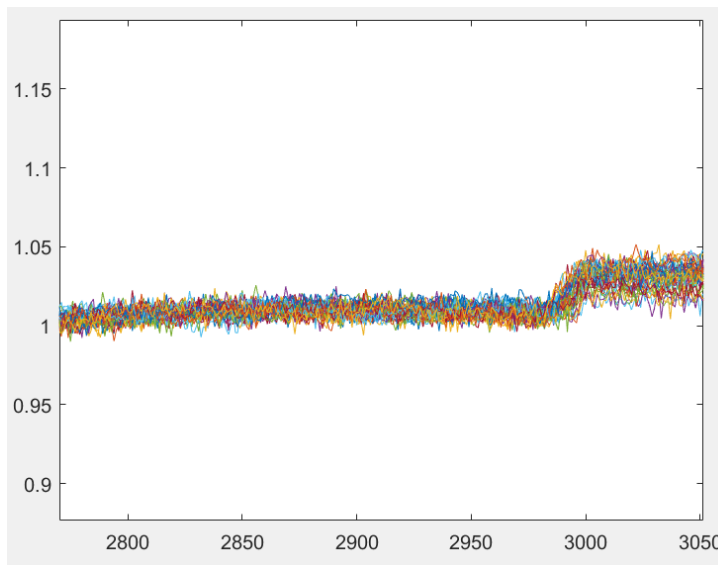


Figure 57 Pressure data after Y axis modification, the data section in this image is the same as shown in Figure 56 section 3. (lower right corner of Figure 56.)

The average pressure plot can then be created by taking the mean value across each row of the matrix containing the pressure data. The standard deviation for each Y value can be found by calculation the standard deviation of each row. The results in a standard deviation plot showing the standard deviation across the pressure plot. This standard deviation plot can be seen in Figure 58.

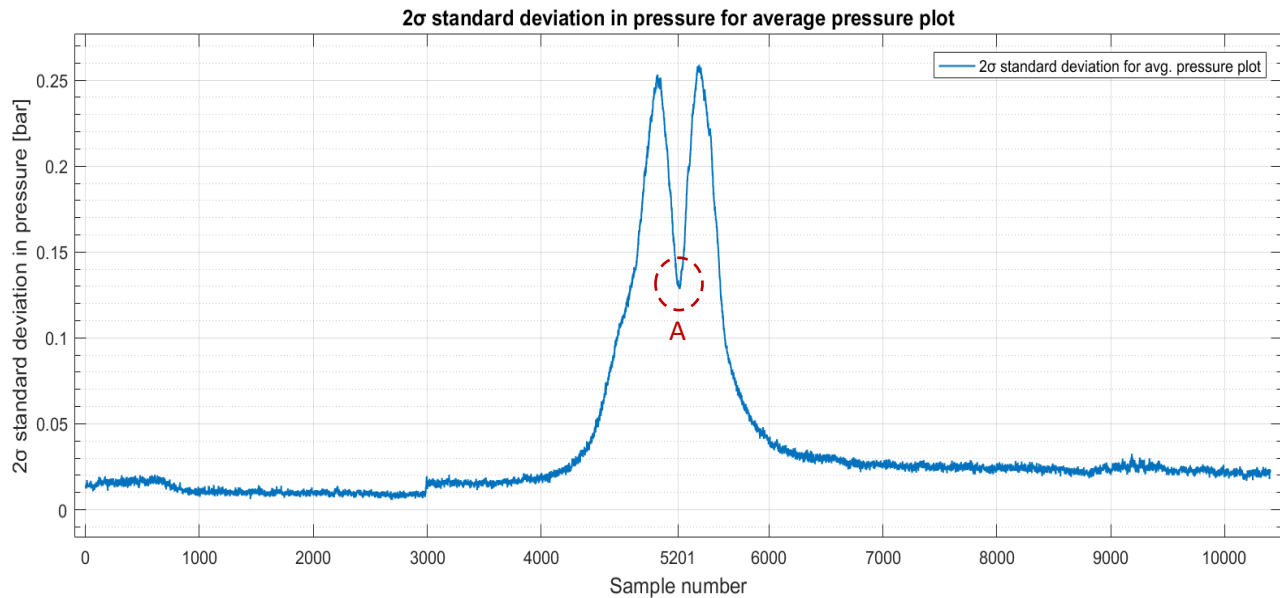


Figure 58 Two sigma standard deviation plot. The plot show footprints from the method used for data alignment.

The maximum uncertainty in Figure 58 from the average pressure plot shows that the specific pressure plot has a maximum uncertainty at two sigma confidence interval, (confidence level 95.44% [35]) corresponds to 0.26 bar, in the same region where the uncertainty is highest the average pressure is around 25 bar. A quick estimation shows us that the maximum uncertainty induced by the creation of average pressure plot data is around $\pm 1\%$.

In Figure 58 there is a drop in the uncertainty exactly at $x=5201$, indicated by a red circle marked with A. This decrease in uncertainty can be traced back to the method used to align the pressure data to create an average pressure plot. Remember the average pressure plot consists of several isolated pressure curves. As the average curve is created the peak value from each pressure curve is used as a reference point. Therefore, the uncertainty will be lower in the peak location than in the nearby sections since each pressure curve has a slight different slope and peak.

4.6.5 Statistical Analysis of Average Pressure

Knowing the statistical behavior of the data collected is essential to have confidence and draw conclusions based on the results. Figure 59 show a sample of 100 pressure data points extracted from a static region of a long series of pressure data. The sample analyzed consist of 100 data points, that is used to generalize the behavior of pressure sensor to the whole population of pressure data. Further statistical analysis is based on chapter 6 in book “Introduction to Engineering Experimentation” by Wheeler and Ganji [35].

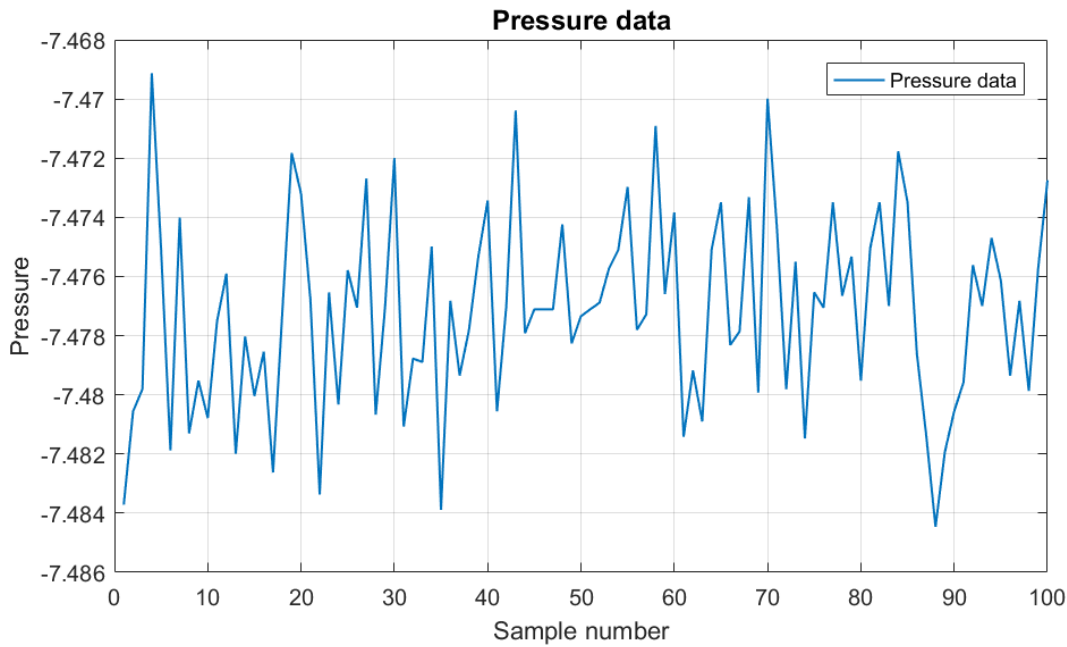


Figure 59 Extracted section of pressure data from the dynamic pressure sensor in the engine chamber.

Variable	Symbol	Formula
Mean	\bar{x}	$\bar{x} = \sum_{i=1}^n \frac{x_i}{n} \quad (1.2)$
Standard deviation	S	$S = \sqrt{\sum_{i=1}^n \frac{(x_i - \bar{x})^2}{(n-1)}} \quad (1.3)$

Table 9 Presentation of formulas used for statistical calculations

The data presented in Figure 59 is analyzed using general statistical analysis presented in Table 9.

4.7 Analyzed Data Sample

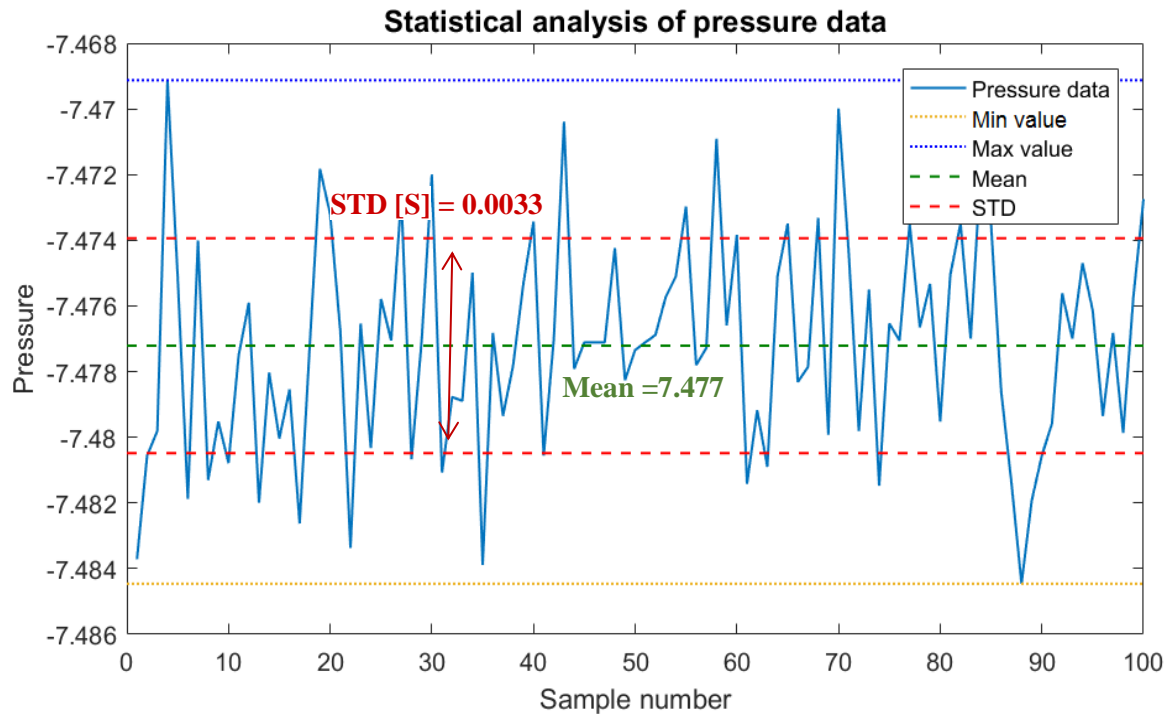


Figure 60 Statistical analysis of a pressure data. The figure indicates

After implementing the general statistical analysis of the data sample from the pressure sensor the results are presented in Figure 60. The standard deviation of the sample is $S=0.0033$ bar, and the mean $\bar{x} = 7.477$ bar. The important value from this analysis is the standard deviation as this value can be generalized from this sample to the whole population of pressure data [35]. In other words, the total uncertainty of the pressure data will have an addition from the natural variation in pressure values measured by the sensor. If the data is presented at the standard two sigma confidence level, the uncertainty from the raw pressure sensor data is 0.0066bar. However, this presentation is only valid if the data is normally distributed. The next section will investigate the distribution of the pressure data.

4.7.1 Distribution of Pressure Data

The pressure data can be sectioned into bins and plotted vs the frequency that the bins occur. This type of histogram plot is a useful graphical tool to categorize the distribution of a dataset. Figure 61 shows a histogram plot of the pressure data, with the curve in red representing the ideal normal distribution for the same dataset. From Figure 61 it can be observed that the histogram closely resembles the shape of the bell curve for the normal distribution function and reinforces the probability that the sensor data follows the normal distribution.

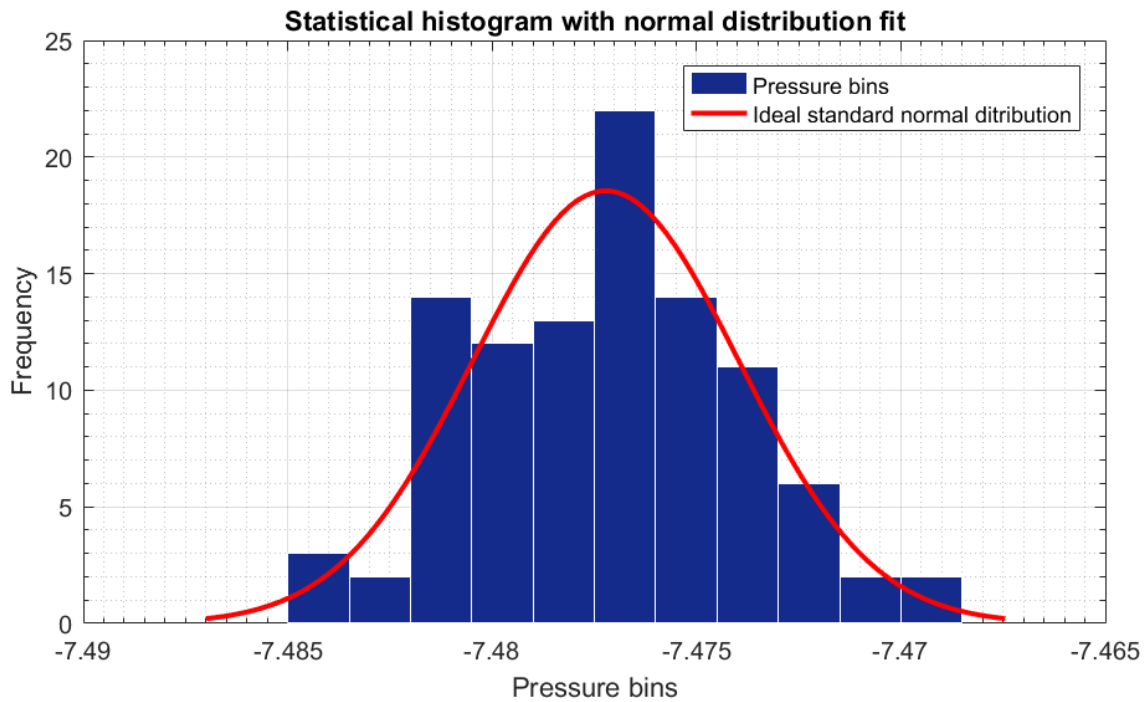


Figure 61 Histogram plot of pressure data, compared to the ideal normal distribution for the same dataset.

Another tool to categorize the distribution of the dataset is a quantile-quantile (QQ) probability plot. A QQ plot compares two probability functions by plotting their quantiles against each other. In Figure 62 a QQ plot shows the quantile of the pressure data marked with blue x symbols vs the quantile of the normal distribution illustrated with the linear red dotted line. We can observe that the pressure data point aligns close to the normal distribution function. The results from the QQ plot further emphasize the histogram plot in Figure 61 and it is concluded that the pressure data is assumed a random stochastic variable that follows the normal distribution function.

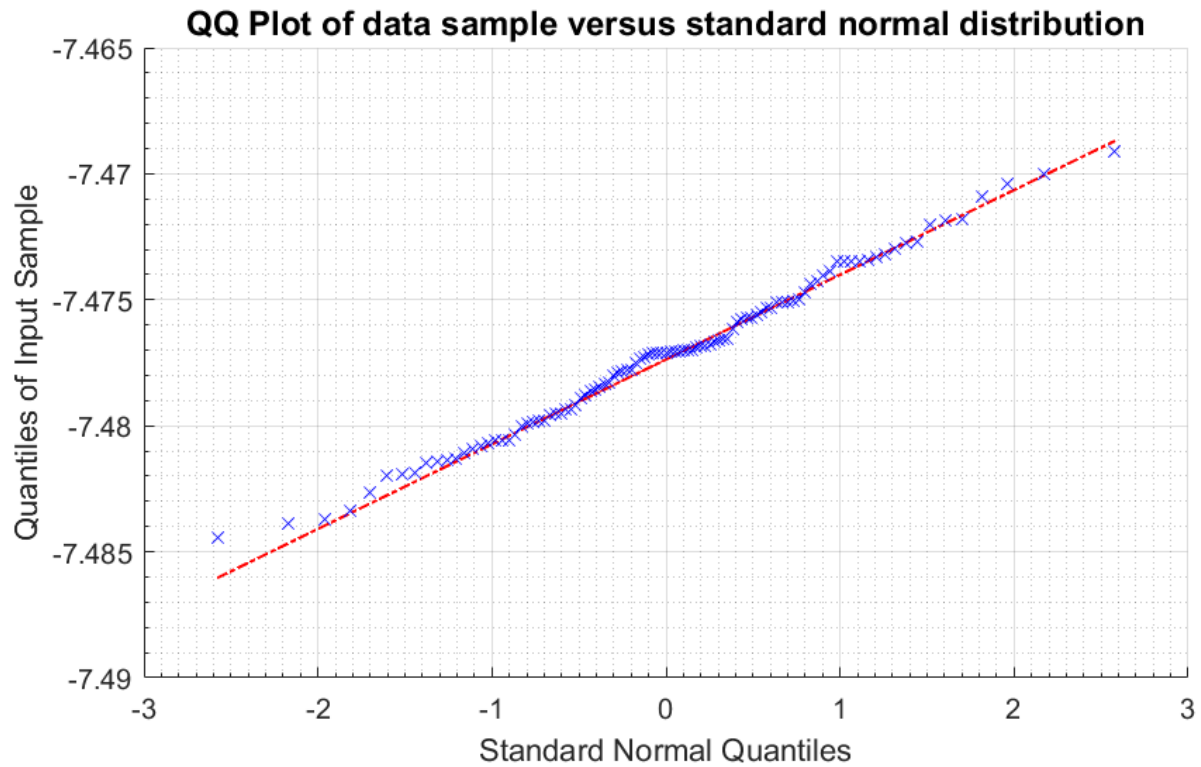


Figure 62 Quantile-quantile plot pressure data points marked with blue x symbols. The red line illustrated the ideal normal distribution function.

4.8 Result and Analysis of Window Torque

The window retainer torque sweep is conducted from 5Nm tightening torque on the window retainer until 24 Nm, at 2 Nm intervals from 5 Nm to 24 Nm. In Figure 63 the average pressure curve for each of the torque level is presented in Figure 63.

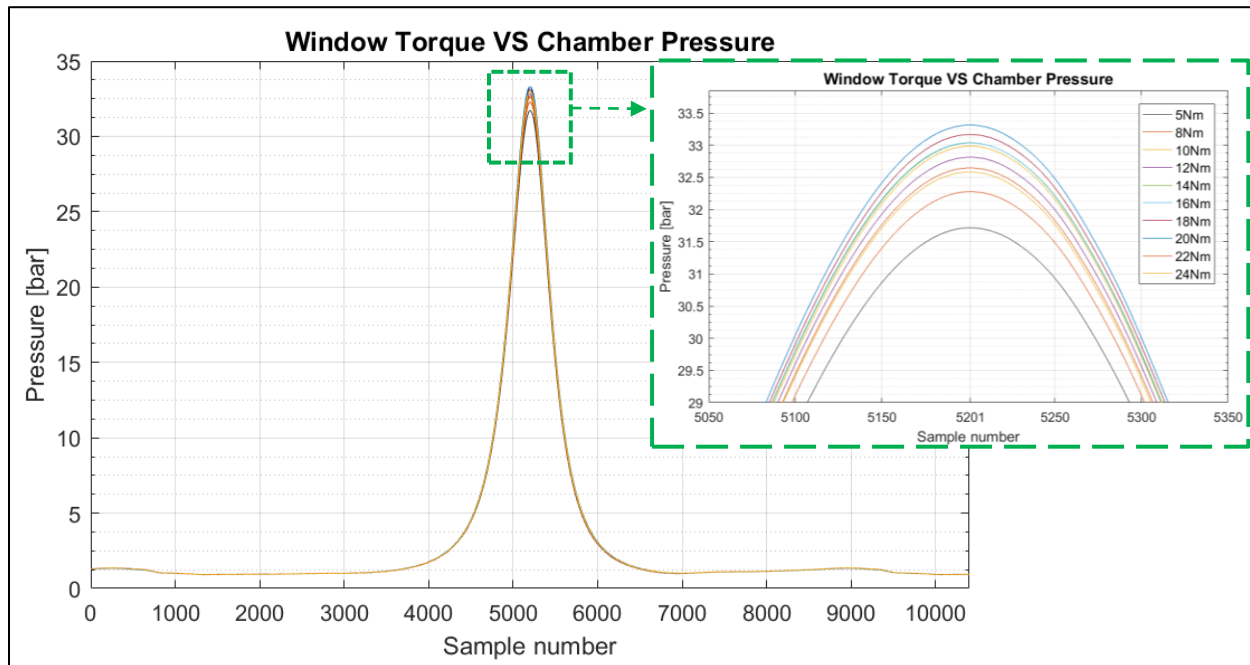


Figure 63 Window retainer torque vs combustion chamber pressure.

The trend between the chamber pressure and the window torque can easily be observed by extracting the peak pressure values for each window torque. The peak pressure for each torque level is presented in Figure 64 below.

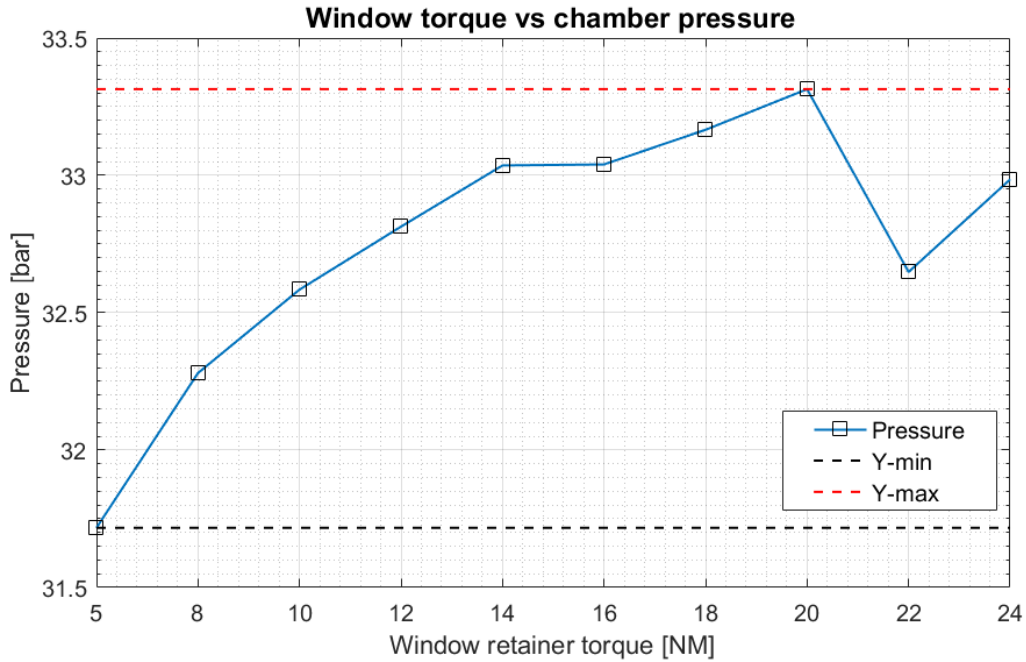


Figure 64 Peak pressure value for each window torque

From Figure 64 it can be observed that there is a clear relation between the window torque and the pressure sustained within the chamber. Already from 5 Nm the chamber sustains a relative high pressure of around 31.7 bar. As the window retainer tightening torque increases the pressure between the window, -the seal and the sealing surface increases and the connection can hold a higher pressure inside the chamber. At around 14 Nm there is a plateau in the increasing pressure from increasing window torque. From 14Nm and until the max torque tested at 24Nm the chamber pressure fluctuates with increasing torque. Part of the fluctuation can likely be traced back to variations and uncertainty induced by computing the average pressure plot for each setting.

4.8.1 Max Window Torque

As the window retainer is torqued into the head assembly, the torque applied results in an axial force acting on the quartz window, this section will show quick calculation to show the stress applied to the quartz window. A heuristic method for calculating the relationship between the applied torque (T) and axial force (F) to bolts is seen in equation (4.1) [36]. k is the torque coefficient for the specific thread and material and d is the outer diameter of the bolt.

$$T = kFd \quad (4.1)$$

To solve with respect to the axial force F , equation (4.1) can be rewritten to (4.2).

$$F = \frac{T}{kd} \quad (4.2)$$

The window retainer can be treated as a hollow bolt with dimensions M65X2 made from stainless steel. The torque coefficient k , for metric threads from steel-steel k is approximately equal to 0,15 [36] and $d=65\text{mm}$. At the max torque applied in the pressure test $T=24\text{NM}$, equation (4.2) results in an axial force $F=2461.54\text{N}$. The window retainer is seen as the brass colored hollow cylinder in Figure 65. The engine head is transparent and the quartz window is blue in Figure 65. The force $F=2461.54\text{N}$ spread across the surface where the retainer intersects with the window.

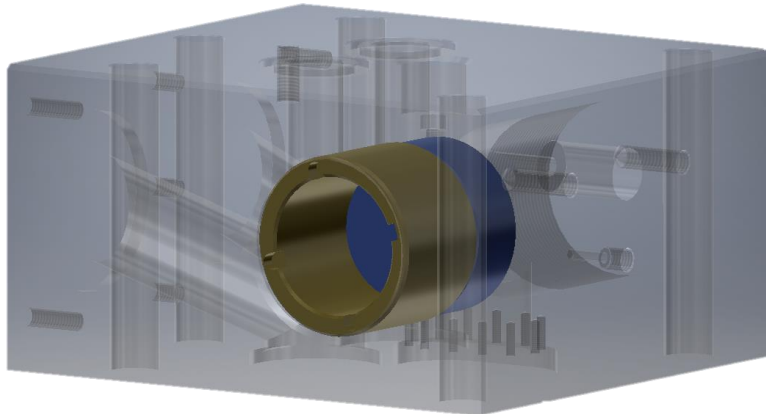


Figure 65 Retainer and window in position in the engine head assembly

The intersection surface where the force is applied is inspected to be 976mm^2 . The axial force F results in a pressure across over the intersection surface as seen in equation (4.3).

$$P = \frac{F}{A} \quad (4.3)$$

The pressure exerted to surface of the quartz window can then be calculated to be approximately 2.52MPa . The quartz window has a reported tensile strength of 50MPa [37]. This simplified calculation shows that the force applied to quartz window from the window retainer is far below the tensile strength of the material. In an ideal case where all the force is applied directly to the quartz window the window should withstand a torque of 475.8NM . This is an unrealistic and unpractical torque figure for this type of assembly, but it shows us that the quartz window should

be able to withstand a lot more force than what it is subjected to with the window torque at 24NM. The real danger as the retainer torque increases are particles stuck between that retainer and the window. This can cause chipping and crack growth of the brittle quartz.

4.9 Temperature Characteristics

4.9.1 Passive Heating, Time and Settings Need to Reach 200°C

The passive engine heating curve represents the thermal characteristics of the engine while adding heat through the heating elements. In Figure 66 the thermal response in the engine to passive heating is presented. In Figure 66 the blue line represents temperature sensor located in the combustion chamber wall. The red line represents the far mounted sensors on the engine head. The black line represents the cylinder liner sleeve temperature. The goal of this section of the experiment was to find out how long it takes to heat the combustion chamber to 200°C and what heater settings is needed. The blue line in figure shows three annotated points A, B and C. These three points in Figure 66 represents the sections where the set-points of the pre-heating blocks is gradually increased to reach 200°C in the chamber. In point C the set-point temperature is increased to 231°C. This is the temperature needed to reach 200°C in the combustion chamber temperature sensor.

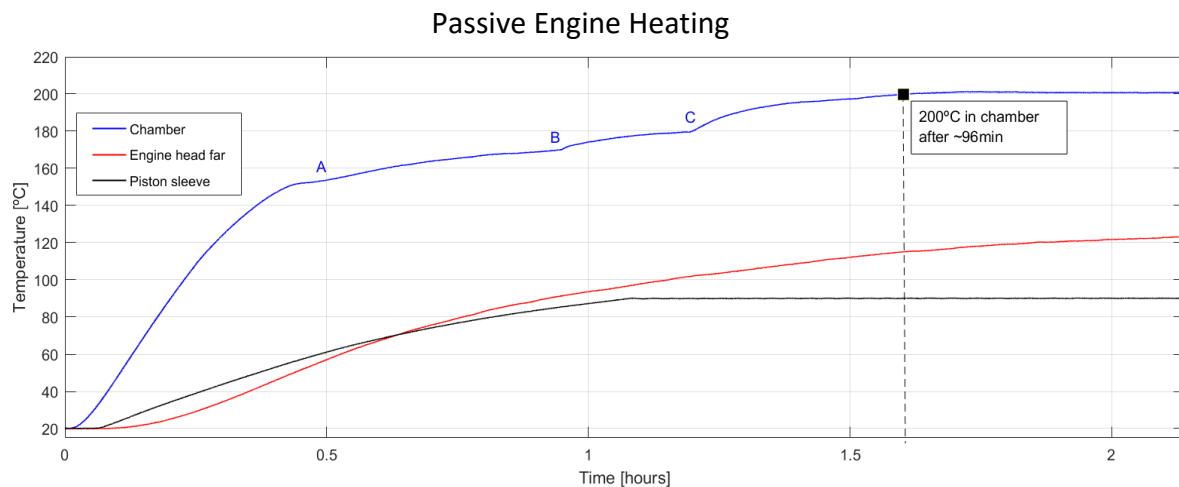


Figure 66 Passive engine heater curve. Blue line indicates the temperature sensor located in the combustion chamber wall. Red line the temperature of the far mounted head temperature sensor. The black represents the piston sleeve temperature sensor.

All places where inlet air intersects with the engine there should ideally be constant uniform temperature. This is a real case however and the engine is not capsuled in a thermal chamber.

For passive engine preheating the suggested heating settings to reach 200°C in the combustion chamber in approximately one hour is:

Suggested Preheating settings:

- Heating blocks:
 - Set-point: 231°C
 - Heat load/duty cycle 50%
- Sleeve heater
 - Set-point: 90°C
 - Heat load/duty cycle 50%

4.9.2 Engine Cooling

From the cooling curve, we can see that the temperature exponentially declines. The heating blocks needs to be replaced with windows, seals and retainers before the engine can be started. Therefore, it is important to know how fast the temperature declines the first minutes after turning the heat of.

The Engine cooling data was collected directly after the passive heating test. Consequence the cooling curve picks up where heating test ended. The test is conducted by turning all heating elements off and leaving the chamber heating blocks in the engine. As the hot engine dissipates energy to the ambient air in the laboratory at 18°C the cooling characteristics of the engine is recorded. The Cooling curve is presented in Figure 68 shows the first 20 minutes of the cooling curve.

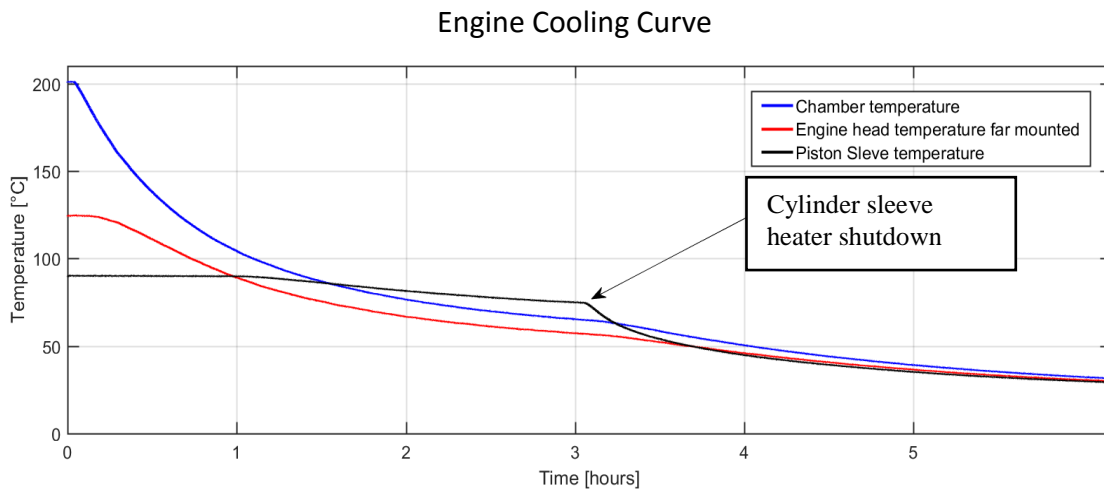


Figure 67 Cooling curve for the engine rig. Blue line represents chamber wall temperature, red line indicates far mounted engine temperature sensor, black line indicates cylinder sleeve temperature.

From linear approximation is found that the temperature in the chamber wall decreases at a rate of $\sim 2.58^{\circ}\text{C}$ per minute for this section of the curve.

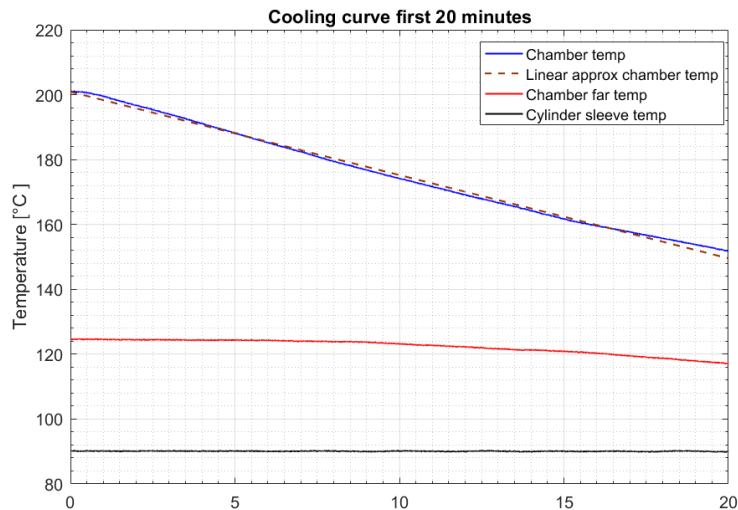


Figure 68 Cooling curve the first 20 minutes after heater shutdown

4.9.3 Thermal Response Running Engine

In this section, the temperature response due to the engine drive by the electrical motor is investigated. Effectively the engine is compressing air in the combustion chamber. Heat is generated from the friction between the cylinder wall and the piston, and the rapid compression of air. The test is done with the engine running for 4 minutes. This process is repeated at three starting temperature. First test is done with the engine cold, then from 60°C and a last from 100°C .

In the two following pages, the result from the engine test with the air heater off is presented in Figure 69 and Figure 70. Figure 69 show three plots marked with A, B and C. These three plots show how the temperature increases with time while the engine is running. Figure 70 consist of four plots. A, B, C and D. In Figure 70 plot A and B is the average pressure curve recorded at the end of the 4 minutes of running the engine. Figure 70, Section C shows a bar plot of the max pressure recorded at each temperature. Figure 70, section D shows a plot of the standard deviation in the average pressure curve created at the three temperature levels.

For the running engine with the air heater turned on the results are presented in Figure 71 and Figure 72. The figures are structured in the same way as mentioned in the section above for Figure 69 and Figure 70. For the running engine test, the data file for the cold engine test was corrupted. As the cold start with the air inlet heater on seen in Figure 71, section A where recorded at a later stage.

Running engine temperature response, cold inlet air

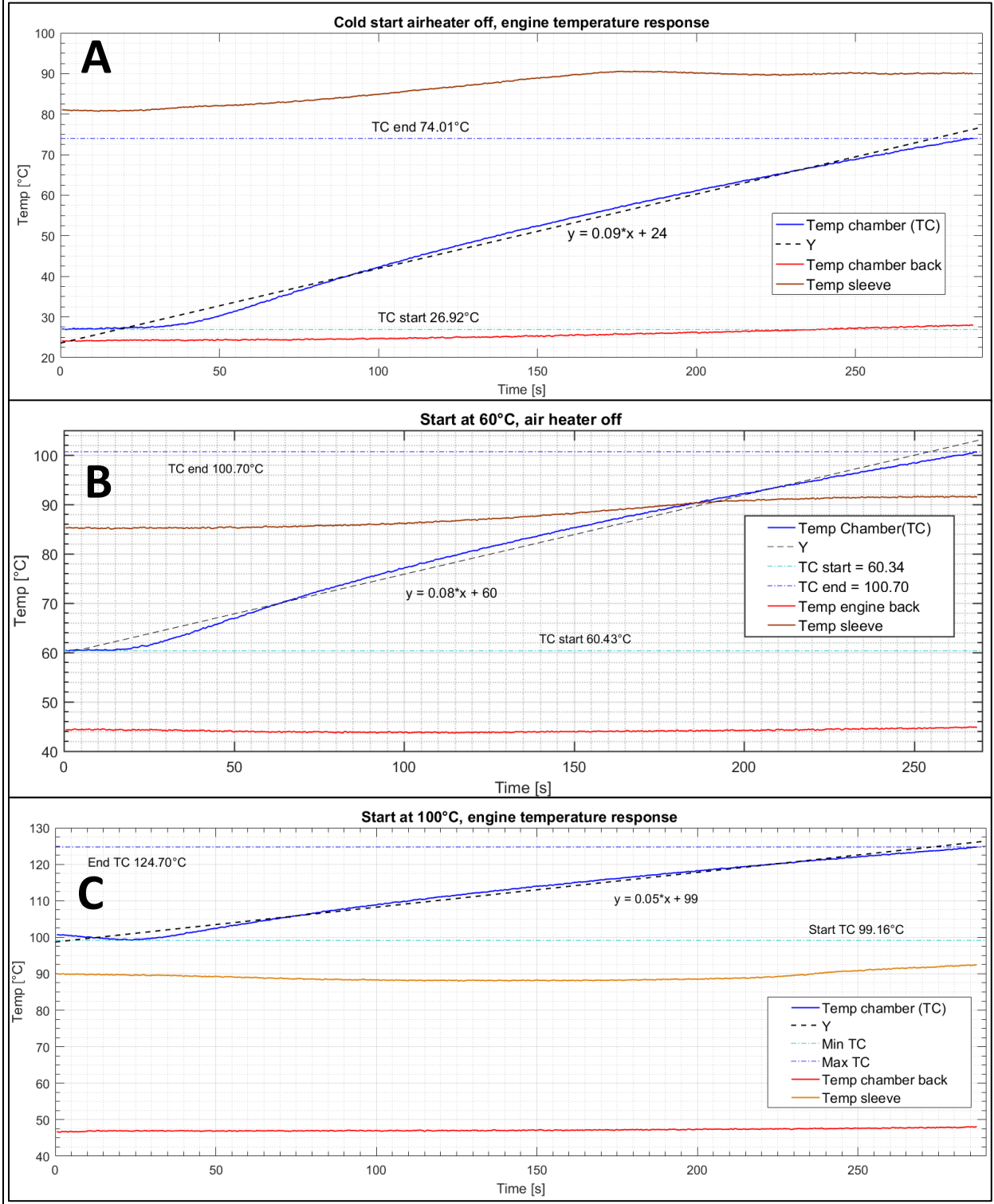


Figure 69, Temperature response running engine, cold inlet air. The three plots in section A, B and C represent respectively the temperature response from. A cold, B 60°C and C 100°C

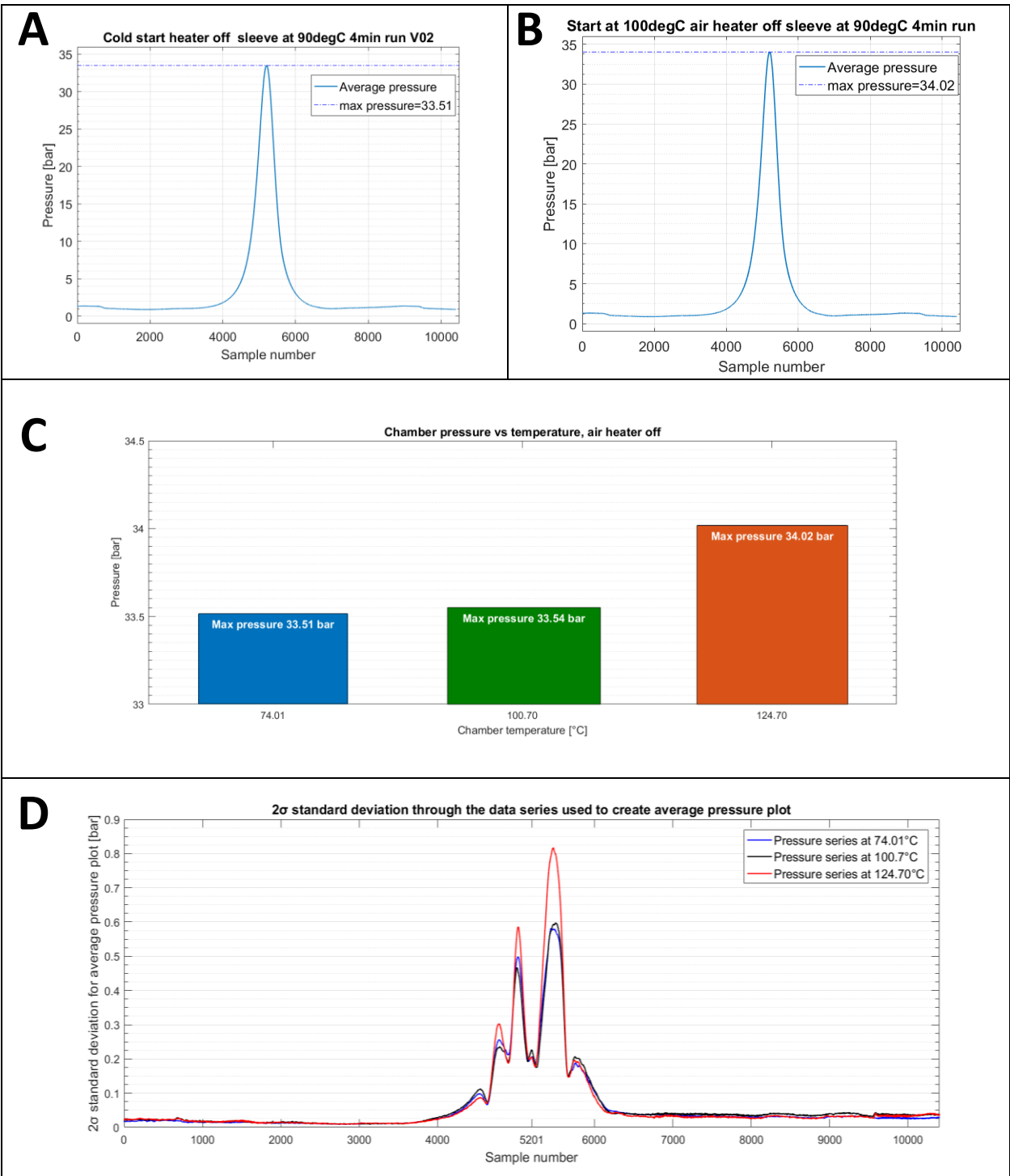


Figure 70 Pressure plot cold run

Running engine temperature response, air heater on

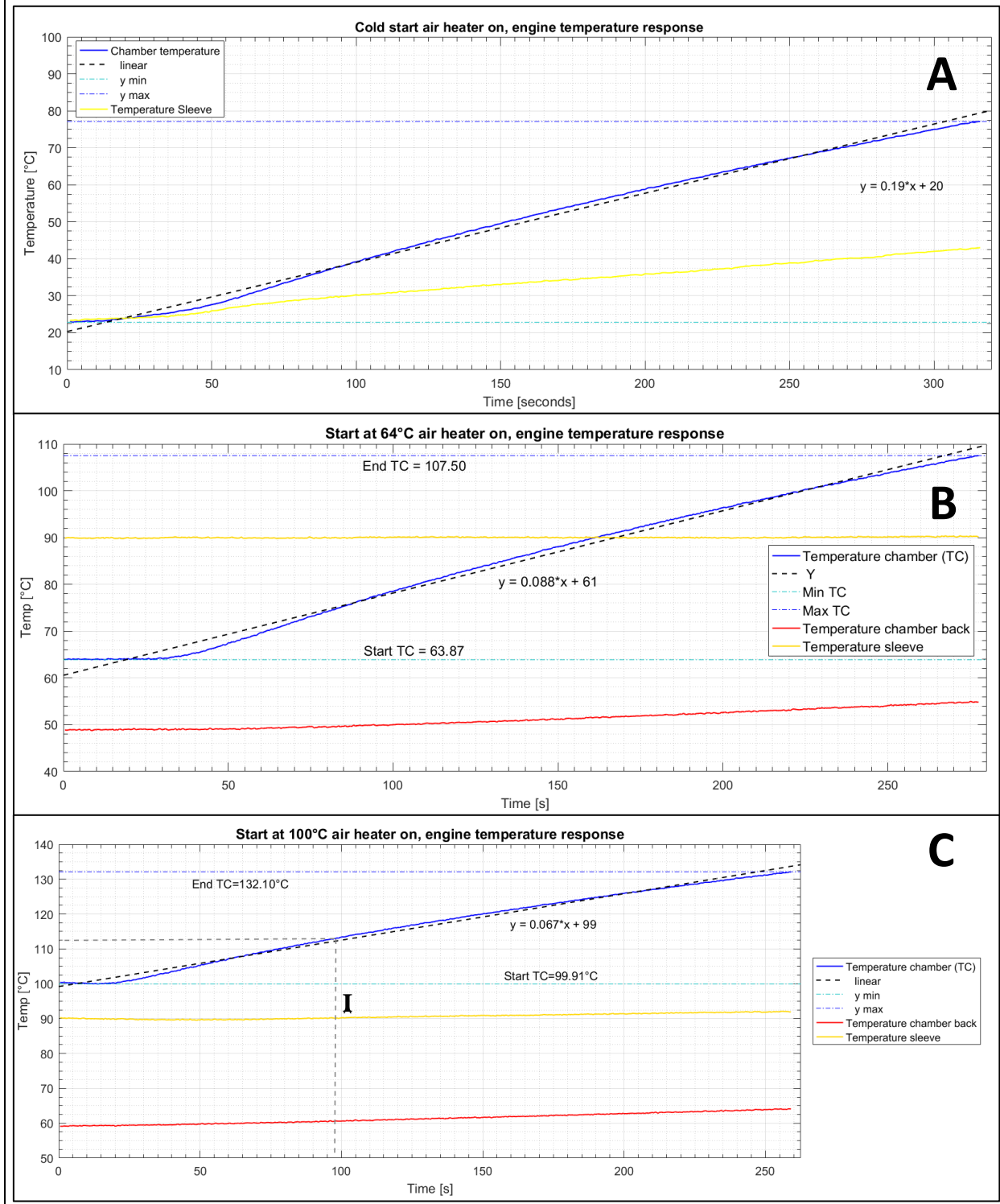


Figure 71 Temperature response running engine test with inlet air heater on.

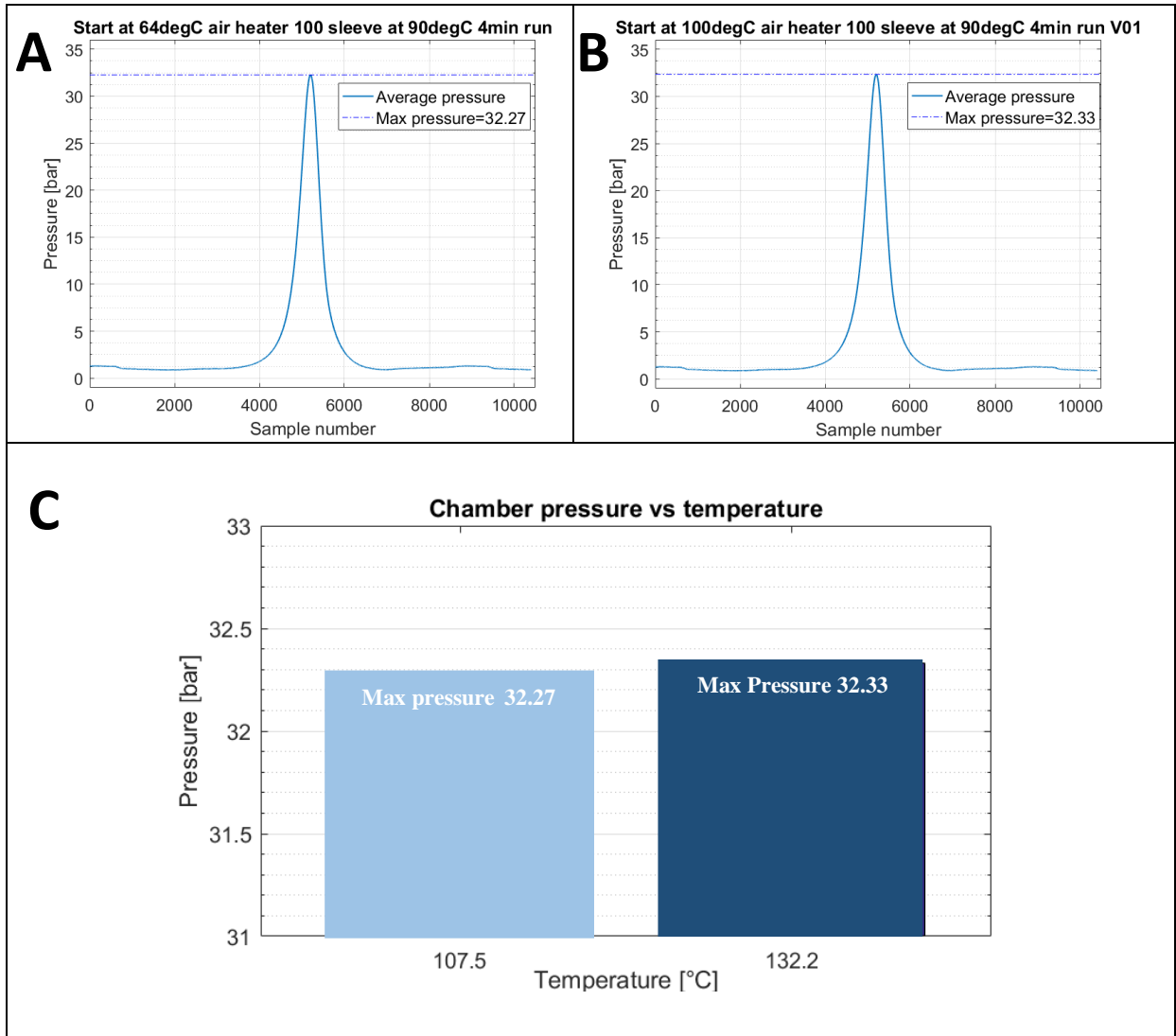


Figure 72 Pressure plots from runs with air inlet heater on 100degC

4.10 Analysis and Conclusion of Thermal Characteristics from Engine Testing

Summary of temperature response, running engine				
	T at start of run [°C]	T at end of run [°C]	ΔT 4 minutes run [°C]	P_{max} [bar]
Air heater off	26	74	47	33.51
	60	100	40	33.54
	99	125	26	34.02
Air heater on	22	78	56	NA
	64	107	43	32.27
	100	132	32	32.33

Table 10 Summary of engine characteristics shown in prior figures

The temperature characteristics from Figure 69 and Figure 71 is summarized in Table 10. It can be seen that at lower temperature the engine temperature increases at a faster rate than when the engine is at a higher temperature. In other words, with greater potential difference the driving forces are larger and temperature change is more rapid. This effect is also seen for the engine test with the inlet heater on. If we compare delta T in Table 10 for the two cases where the inlet air heater is on and off. It can be seen that the engine will be heated faster when the inlet air heater is on, this is logical as more energy is induced into the system.

For the case with the inlet air heater off it can be seen from the pressure plots in Figure 70 and Table 10 there is a slightly increasing trend in the max cylinder pressure when the engine temperature increases. This is an expecting trend as the walls in the combustion chamber is hotter the difference between the temperature of the compressed gas is smaller and less energy is drawn from the compressed air. In theory this should lead to higher pressure in the combustion chamber. After factoring in the uncertainty for the average pressure plot presented in Figure 70, section C the uncertainty at max pressure is ± 0.21 bar at two sigma confidence level, and we can conclude that there is a small but significant increase in pressure when the engine is 125°C than when the engine is cold. For the engine test with inlet air heater on the same trend is not observed. This could partially be due to the fact that less air will enter the engine as the density of air decreases with increasing temperature.

From the running engine test, it can be seen from Figure 69 and Figure 71 section C that the cylinder sleeve temperature is stable at 90°C until the chamber temperature reaches 115-120°C. When the chamber temperature reaches 115-120 the cylinder sleeve temperature rapidly increases. The engine sleeve cooling system is designed for a max cooling liquid temperature 90°C. The cylinder sleeve temperature will need to be higher than 90°C for the rapidly moving cooling water to reach 90°C. However, as the sleeve temperature increases rapidly when the chamber temperature is above 115-120°C is recommended to stop continuous operation of the engine to avoid ceasing the piston in the sleeve.

Chapter 5 Light Distortion, IODBIEI and DBIEI

5.1 Overview

To investigate the effects of light distortion in the experimental system this section contains a comparative study between three configurations of the experimental system. The first method used is a *Schlieren one mirror coincident configuration*. The schlieren method is a visualization technique used to enhance the effects of light distortion due to density gradients in a medium. The second setup is a diffused back-illumination extinction imaging (DBIEI) in the same configuration used for soot imaging earlier in this report. The third setup is a modification of the DBIEI setup, with a new lens configuration aimed toward reducing light distortion.

To quantify the difference between the three setups, three objects are used to induce varying degree of light distortion. The three objects are seen in Figure 73. Object A is created by cutting out the bottom of a chemistry glass beaker. Object A is intended to have a high degree of light distortion. As an additional visualization for the reader object A can be thought of as the bottom of a glass.

Object B in Figure 73 is a disk made from a sheet of clear glass, equivalent to glass used in windows. Object C in Figure 73 is a quart's cylinder. Object C is the window that is used to seal the optical accessible combustion chamber in the engine rig.

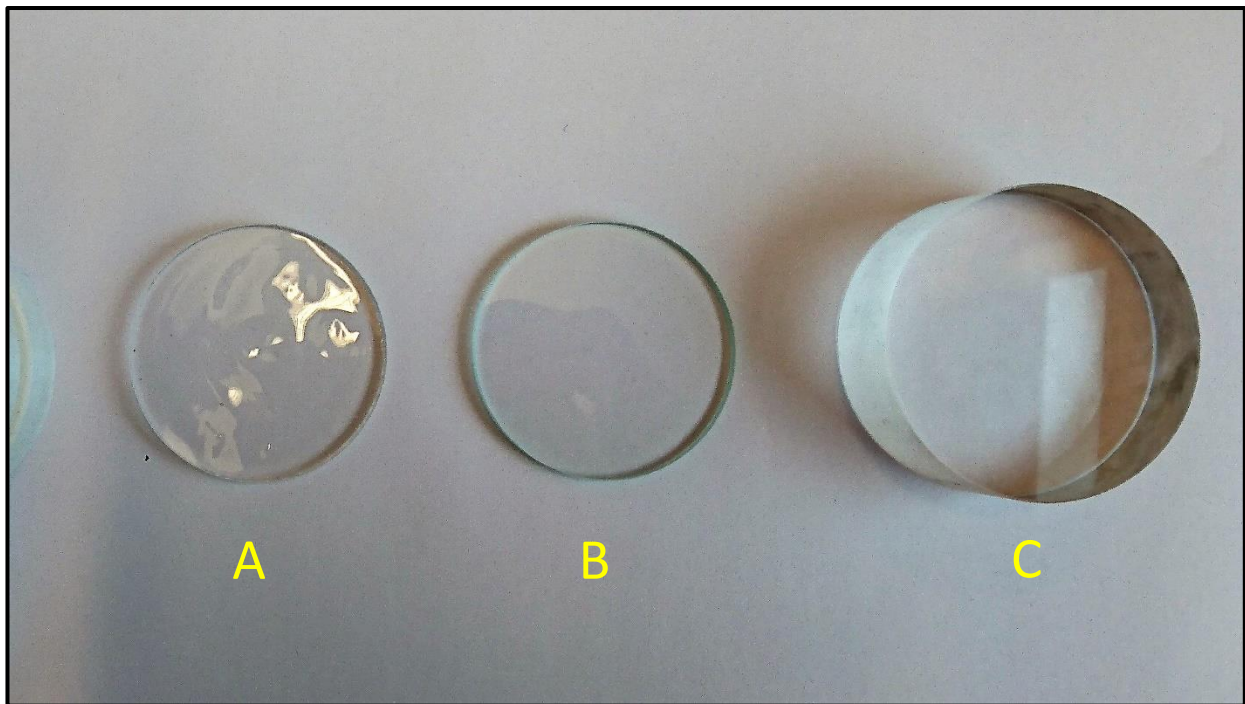


Figure 73 Test objects for light distortion experiments.

5.2 Single-Mirror Coincident Shadowgraph

5.2.1 Setup

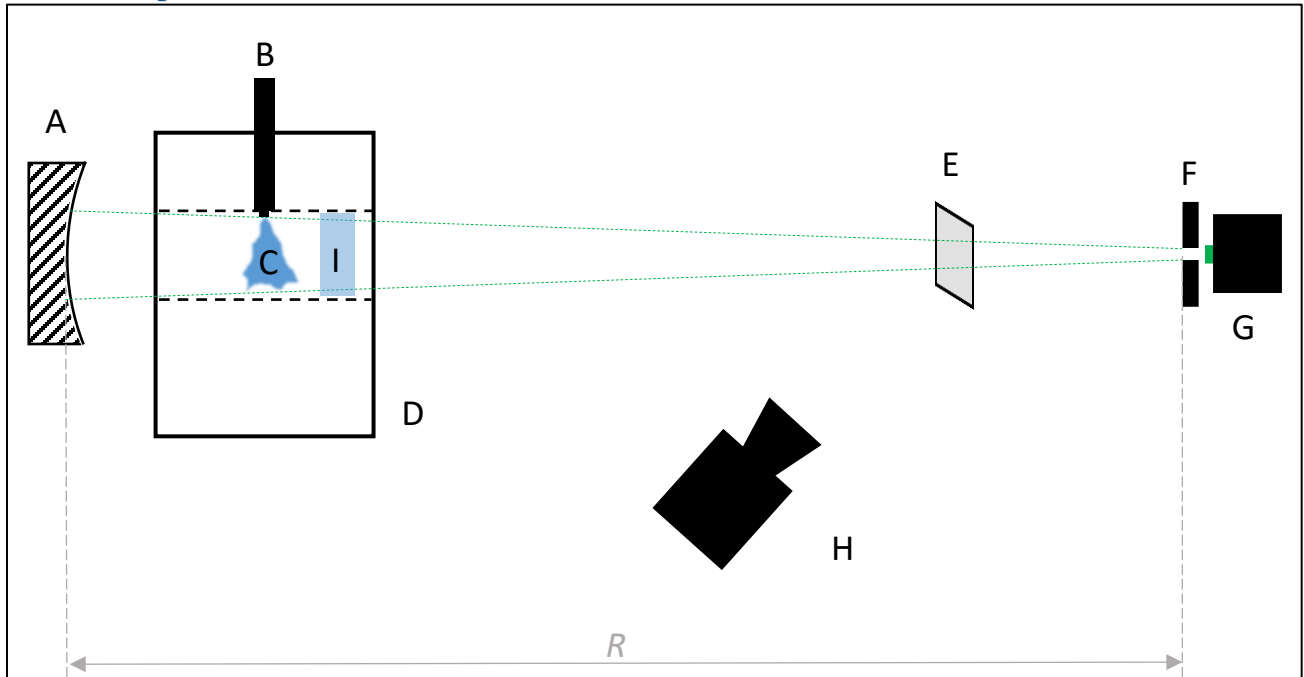


Figure 74 Optical setup for Single-Mirror Coincident Shadowgraph system. Simplified drawing seen from above

A	Spherical mirror, F8, d=150mm, F=1200mm, Research grade, Orion Optics UK.
B	Injector, part of engine rig assembly.
C	Test section
D	Engine head with optical combustion chamber
E	Beam splitter
F	Pinhole d=0.5mm
G	LED
H	High speed camera, with zoom lens (add brand and specs.)
I	Window, illustrated to show placements of windows and glass objects
R	Represents spherical mirror radius of curvature $R=2*F$, $R=2*1200\text{mm}=2400\text{mm}$
Not seen	6" Large Angle Mirror Mount, Edmund optics.
Not seen	Camera mount, various Thor Labs equipment for adjustment.

Table 11 Equipment list for the setup in Figure 74

The optical configuration used in this experiment is illustrated in Figure 74. The system is based on a single-mirror coincident schlieren system, first described by Taylor and Waldram in 1933 [38]. This configuration is widely used due to its high sensitivity, ease of use, and low cost. The setup consists of a high-power LED with a point light source (pinhole $d=0.5\text{mm}$) mounted at the radius of curvature of a spherical mirror (A). Between the light source and the test section a beam splitter is fitted (E). From the beam splitter, the light travels through the test section (C) within the optical combustion chamber. When the light source is placed at the mirrors radius of curvature at

properly aligned, the light that is reflected in the spherical mirror will return through the test section on the same path as it entered. As light passes through the same point in the test section twice this method yields relative high sensitivity to density gradients in the test section.

5.2.2 Alignment Procedure

The following is a suggested procedure based on best practice for alignments of mirror and light source. This procedure will be a lot quicker with two people, as one person should adjust the mirror and an observer can report back the needed adjustment at the light source side.

- Placement:
 - Mount the mirror as close to the test section as possible
 - By visual alignment make sure that center of the mirror and the combustion chamber is aligned.
 - Position the light source at the radius of curvature of the mirror. For the mirror used in this setup: $R=2400\text{mm}$
 - Measure the distance 2400mm with a measuring tape, do not worry about millimeter precision. Have the LED and beam splitter mounted on a rail so that fine adjustment can be properly done later.
 - Strive to mount light source and mirror in approximately the same horizontal and vertical plane, as it will require less fine adjustment.
 - Mount LED and BEAM splitter on adjustable poles for ease of adjustment.
 - Stand directly behind the light source and look towards the mirror through the chamber. Have a partner adjust the three adjustment screws on the mirror mount to tilt/pitch the mirror until a diffuse green mist is seen in the mirror with the naked eye.
- Fine adjustment:
 - Before start:
 - Verify by visual inspection that the setup is roughly aligned and looks straight, verify again that all steps in the above procedure is completed. Otherwise fine adjustment will be useless
 - Goal: Adjust the mirror according to Table 12 Mirror and LED alignment chart.
 - Power up light source to a high intensity, and eliminate ambient room lighting.
 - Locate where the light is reflected from the mirror. This can be done by holding up a white piece of paper behind the source. Once the position of the light reflection is located the goal is to use the adjustment screws on the mirror to align the reflecting light back into the pinhole of the LED where the light is emitted.

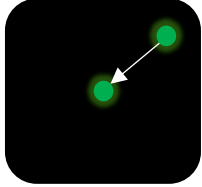
Fine adjustment of LED and mirror matrix				
Illustration				
Problem identification	LED and mirror is placed too close or too far away. Both dots should be the same size and the upper left corner section should be focused.	LED and mirror is placed slightly too close. Increase distance slowly	Distance is correct. Mirror and LED is not properly aligned. By adjusting the mirror tilt/pan aim to center the green dot in the direction of the arrow	Perfect alignment/Far off aligned.
Solution	Adjust distance	Adjust distance	Adjust mirror tilt until green circles are coincident. Be aware that the dot is moved in the correct position.	No adjustment needed if it is verified by proper illumination of the test section in the camera. If not sufficient repeat above procedure.

Table 12 Mirror and LED alignment chart

5.3 Shadowgraph Experiment

Leaving the experimental Single-Mirror Coincident Shadowgraph setup in the exact same configuration as seen in Figure 74, various light distortion objects that is inserted into the “window slot” of the combustion chamber. The placement of the windows slot can be seen as section I in the overview of the experimental setup in Figure 74. For each object, an image sequence is recorded. As introduced earlier the light distortion objects are re-introduced Figure 75 annotated A to C, where C is Quartz, B is Glass, and A is Glass with gradients.

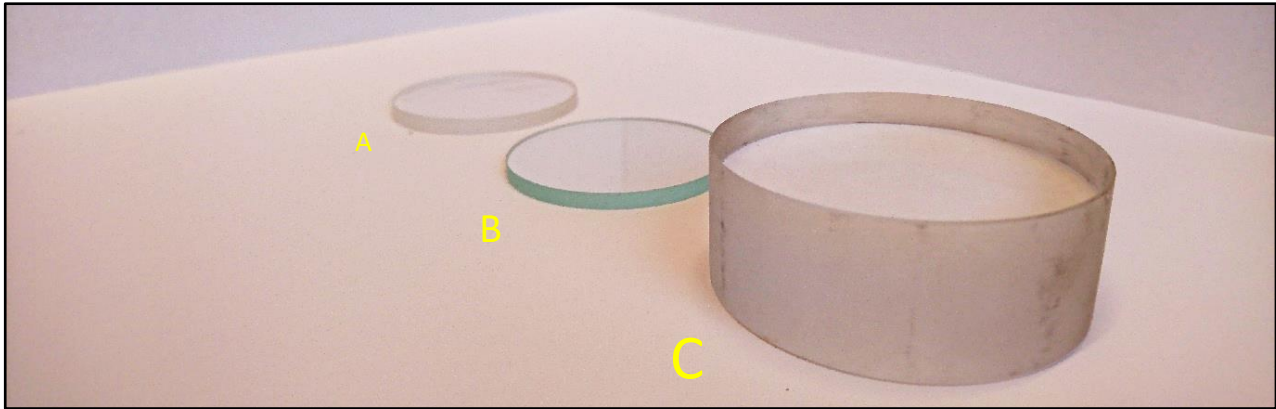


Figure 75 Light distortion objects. C: Quartz, B: Glass, A: Glass with gradients.

5.3.1 Results and Conclusion from Shadowgraph Experiment

5.3.2 Image Background

The background image of the schlieren setup is shown in Figure 76 below. The annotated *section B* of the figure shows artifacts that are reoccurring throughout the images captured with the schlieren setup. The red (I) mark show a concentration of light in the center of the image. The yellow markers (II) indicates dust spots on the camera lens. And the white markers (III) is the shadow of the injector tip in combustion chamber.

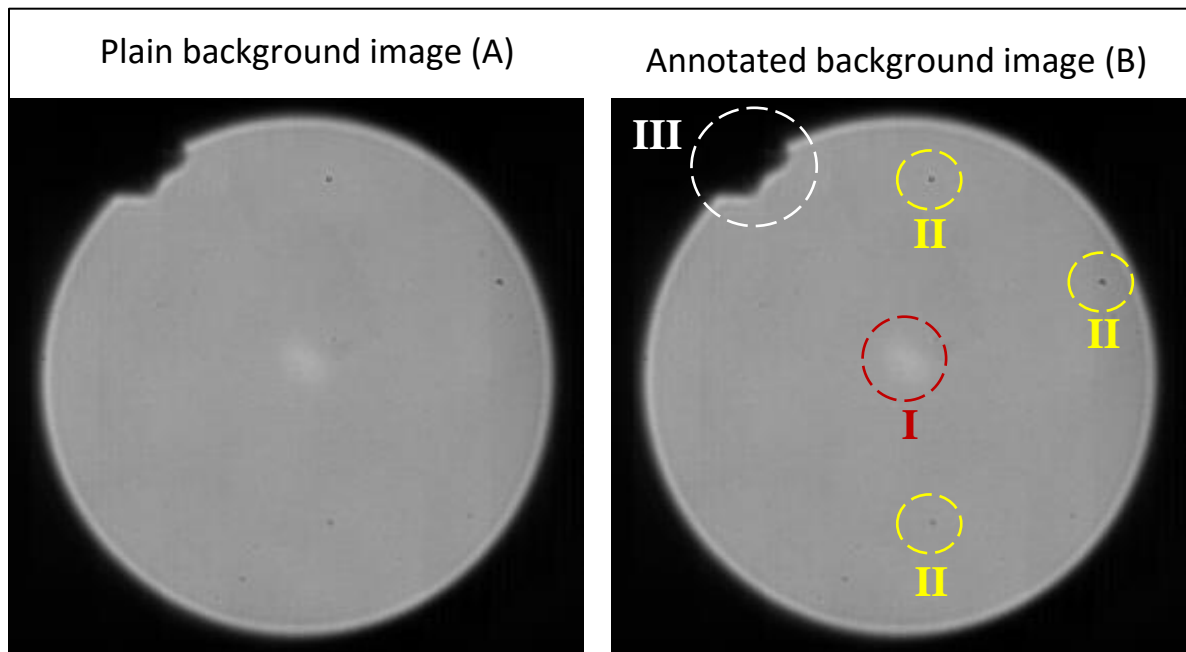


Figure 76 Plain Background image seen in the left section marked with A. The right section marked B annotates the re occurring objects in the image. The yellow (I) mark show a concentration of light in the center of the image. (II) indicates dust spots on the camera lens. (III) is the injector tip in combustion chamber.

Object A

Object A steered the light too much to create any meaningful image of the object. The output image with object A in the chamber is completely black with some tiny brighter spots. In other words, object A deflects all of the light away from the camera. Object A is not useful for this optical method, but it can serve later as a benchmark for maximum light distortion.

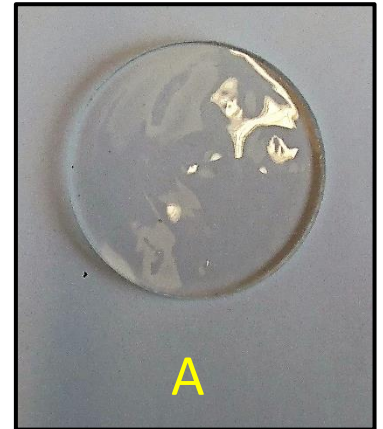


Figure 77 Object A

Object B

With object B in the chamber only a small amount of light is deflected. The recorded image of object B is shown in Figure 78. From Figure 78 it can be seen that there are clear streaks across the glass objects. These streaks are most likely the result of the production method used to create the glass sheet. With the naked eye object B appears uniform, but the disc is not made from optical grade glass. The amount of light distorted seems within a reasonable limit for object B.

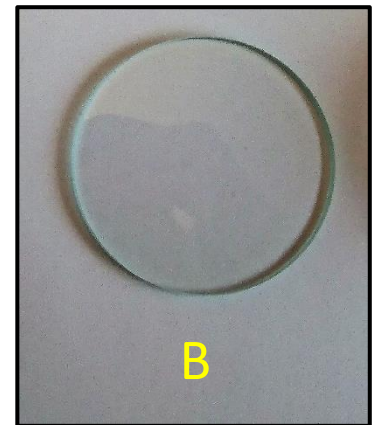


Figure 79 Object B

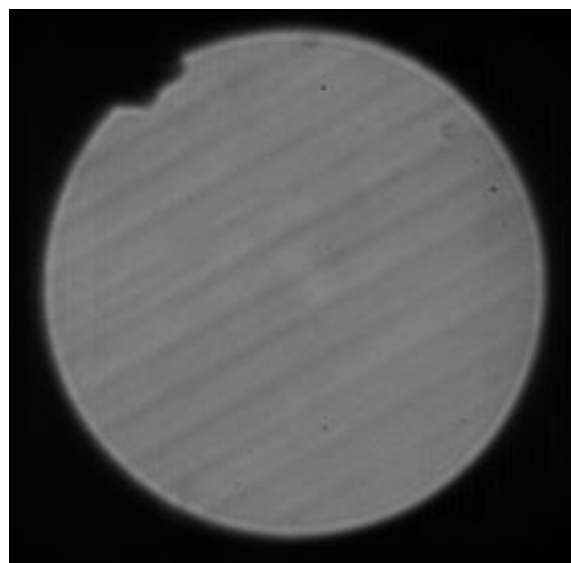


Figure 78 Shadowgraph of object B

Object C

Object C are the quartz windows intended to seal the optically accessible combustion chamber. Figure 81 shows the image captured with object C in position. Compared to object B the quartz window induces way more light distortion. If this Single-Mirror Coincident Shadowgraph setup is desired to be used to visualize flow in the combustion chamber with the engine running new windows with better optical quality needs to be used.

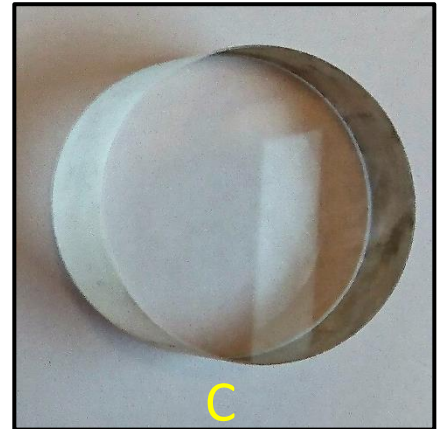


Figure 80

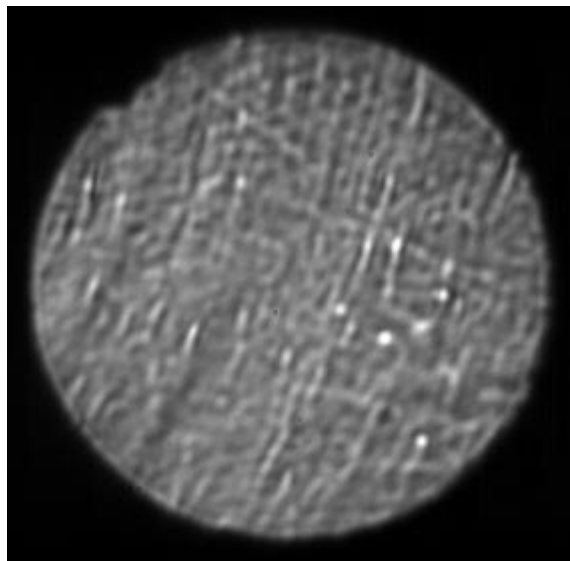


Figure 81 Object C in chamber

5.4 Comparative Investigation IODBIEI and DBIEI

5.4.1 Introduction

In this section, a new configuration of the DBIEI setup is presented. Images of objects with varying refractive index is collected for the two setups. A relative comparison is presented to determinate if the new DBIEI setup reduces the conditions of light distortion in the test section.

5.4.2 Experimental Setup

The *old* experimental setup is the IODBIEI configuration used for the initial soot extinction measurements. The optical configuration of the IODBIEI is shown in Figure 82. To quantify the relative conditions for light distortion in the two optical configurations the three refractive objects A to C used in the shadowgraph experiment is used in this experiment also.

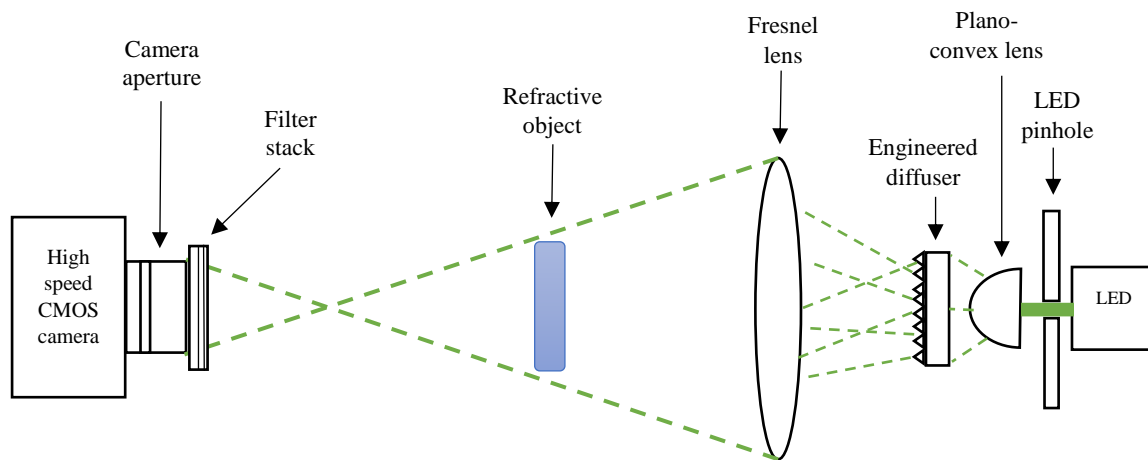


Figure 82 Old IODBIEI setup.

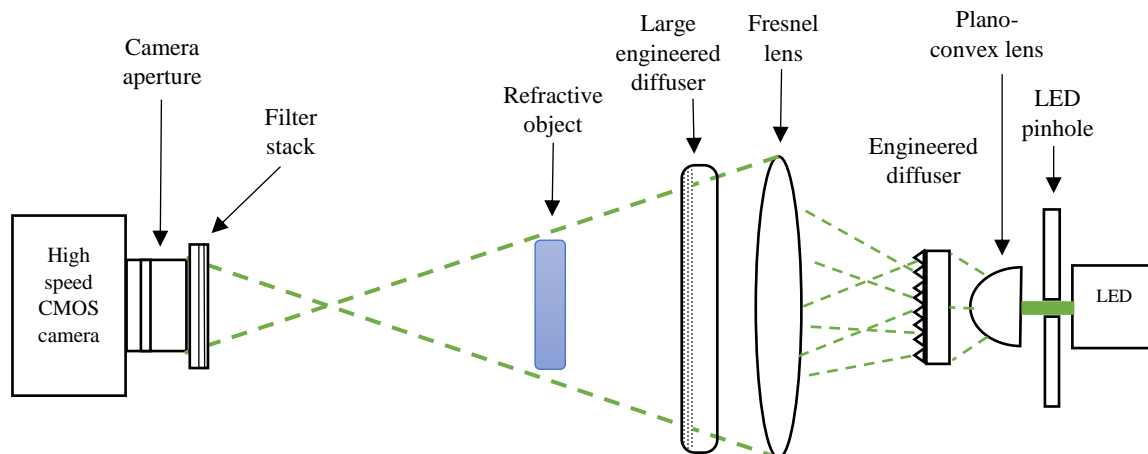


Figure 83 New optical DBIEI setup.

The new DBIEI introduces only one new elements as seen in Figure 83. The new element is a large circular engineering diffuser with diameter of 100mm. Figure 84 shows the diffuser appearance. The grainy side is faced away from the light source. The diffuser consists of a thin polymer substrate on a glass disc. The polymer has a carefully engineered surface that diverge light rays off at a divergence angle 16.4° [39]. The design of the diffuser layup is seen in Figure 85. At the surface of the diffusor the polymer is formed as sphere caps, that will defect light in three directions in the same fashion as a convex lens. These sphere caps on the diffuser surface can be seen in Figure 85.

Experiment matrix	
Optical config	Object in chamber
Old DBIEI	Glass disc
	Quartz window
	Glass beaker bottom
New DBIEI	Glass disc
	Quartz window
	Glass beaker bottom

Table 13 Camera settings

Camera info	
Make and model	
Resolution	512x512 pixels
Color mode	Grayscale
Bit depth	16 bits (2^{16}) pixel values from 0 to 65536
Aperture	
Filter	None

Table 14 Experiment matrix

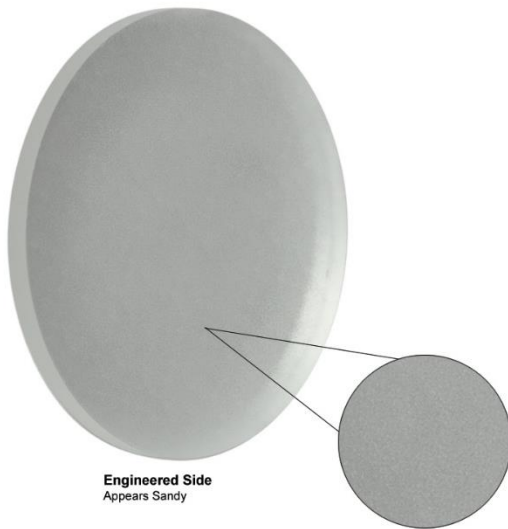


Figure 84 Visual representation of an engineering diffuser. Figure by THORLABS [42]

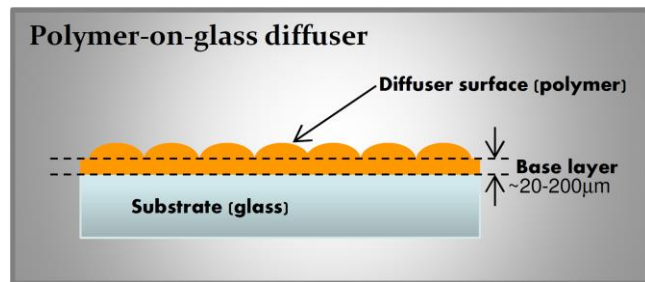


Figure 85 Engineering diffuser layup. Figure from technical product datasheet for "EDC-15-15132" by RPC Photonics, Inc. [39]

5.5 Results and Discussion IODBIEI vs DBIEI

The results from the experiment is presented in Table 15. The three objects with varying refractive index is inserted into the test section of the optical setup. Images are collected with both the new and the old setup. The output images from the old DBIEI setups are seen in the second image column. In the third image column, the images of the same objects with the same setups is presented. Table 15 is indexed with the image columns from A to C, and the rows are indexed by number 1 to 3. As an example, A1 refers to the image in the upper left corner in the table showing an image of a glass disc.

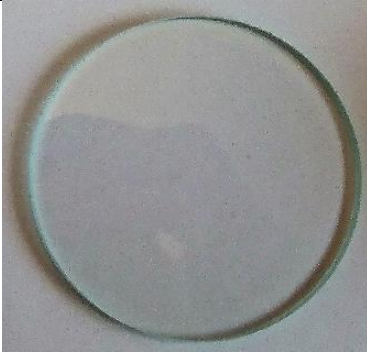
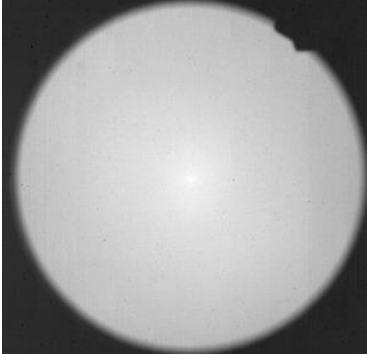
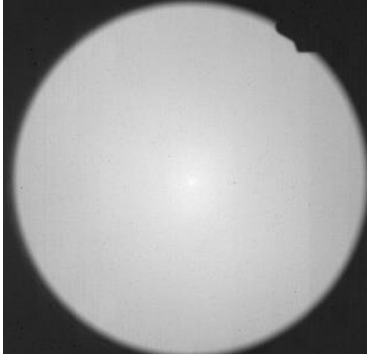
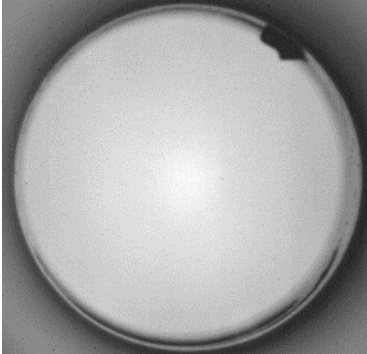
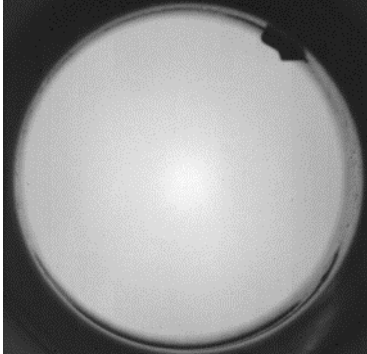
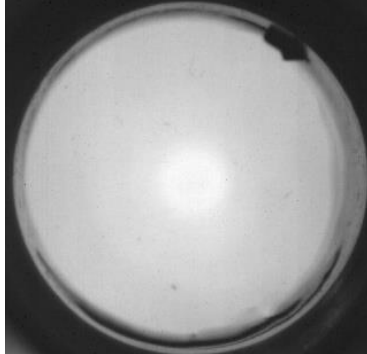
		Output images		
		A	B	C
		Glass disc	Quartz window	Glass beaker bottom
1	Object			
2	Old DBIEI			
3	New DBIEI			

Table 15 Result from light distortion experiments

From Table 15 it can be seen that the glass disc and the quartz windows show no signs of light distortion in the old setup (A2 and B2) or in the new setup (A3 and B3). By comparing image A2 and A3 it can be seen that the background illumination pattern from the two setups are different. The goal is to obtain the most uniform distribution of light across the combustion chamber. By the naked eye the new DBIEI setup (A3) looks to have a more uniform light distribution. In the old DBIEI system there is also a concentrated spot in the center of the image that is more illuminated than the rest. This effect occurs due to a defect in the small engineered diffuser. At some point, an aspheric lens appears to have been jammed with force into the fragile diffuser surface and removed some of the coating in the center of the diffuser. From the image of the new DBIEI setup it appears that this spot of light is diffused to a larger section but it is still visible. To quantify the background illumination differences between the old and the new setup images of both setups with no objects were collected. The images look more identical to the image seen in Table 15 section A2 and A3. To quantify the difference between the horizontal pixel values across the center of each image (row 256) is extracted and presented in Figure 86. In Figure 86 the old DBIEI setup is represented with the blue marker and the new setup with the red marker. The y-axis values in Figure 86 represent the pixel value for each specific pixel index across the x-axis. The pixel values are represented on a 16-bit grayscale, range from 0=black to 65,356=white. In the plot we can see that pixel values increase as the index value approaches #256, which is the center of the image where the bright section is seen in Table 15, image A2. From Figure 86 it can be seen that the new setup has a slightly more uniform illumination profile across the test section, and the spike seen in the old setup is reduced. As the LED is placed in the center of the chamber it is expected to see an intensity gradient in the output image. From Figure 86 we can also see that the new DBIEI setup reduces the background illumination. This is due to the simple fact that the light from the LED has more material to travel through and that some of the light will be scattered, reflected and absorbed.

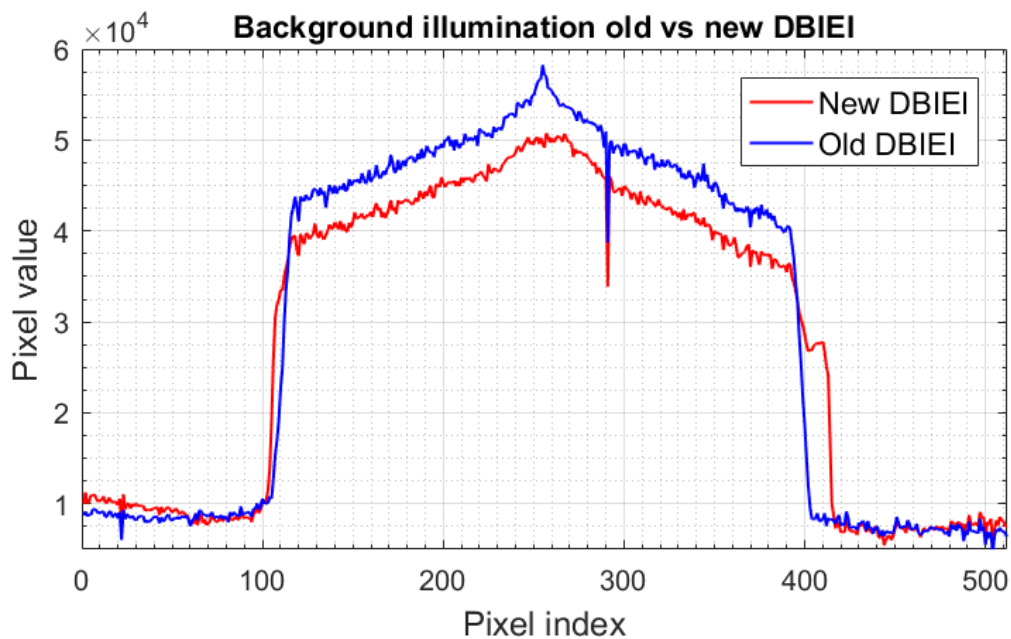


Figure 86 Background illumination old DBIEI vs new DBIEI setup

The most interesting results from the comparison between the old and the new DBIEI setup surfaces from the images of the glass beaker bottom. These images are seen in Table 15 section C2 for the old setup and C3 for the new setup. From the old setup in image C2 it can be seen that the object introduced create a relative large amount of light distortion, resulting in darker sections where light is distorted and the image result is far from uniform.

As the new DBIEI system is used to create an image of the same object it can be seen that the light distortion induced by the glass beaker object is significantly reduced in the new setup. To quantify the reduction of light distortion from the new setup, the pixel values across image C2 and C3 is presented in Figure 87 in the same fashion as done on the prior page for Figure 86. From the red line plot in Figure 87 representing the old image setup. The variation in intensity can clearly be seen as the pixel values fluctuates dramatically between pixel index #120 to #380. It is these variations that makes up the varying intensity seen in Table 15, image C2. For the new setup plotted with the blue line in Figure 87, the light intensity fluctuation is almost eliminated, except for the center region where there is a section of higher intensity. By comparing the plotted values from the old DBIEI and new DBIEI setup it can be seen that the new setup reduces the potential for light distortion by a significant amount.

It is highly recommended that the new DBIEI setup is implemented for high speed imaging of the combustion process in the optical chamber.

Pixel values across center of image with glass beaker old vs new setup

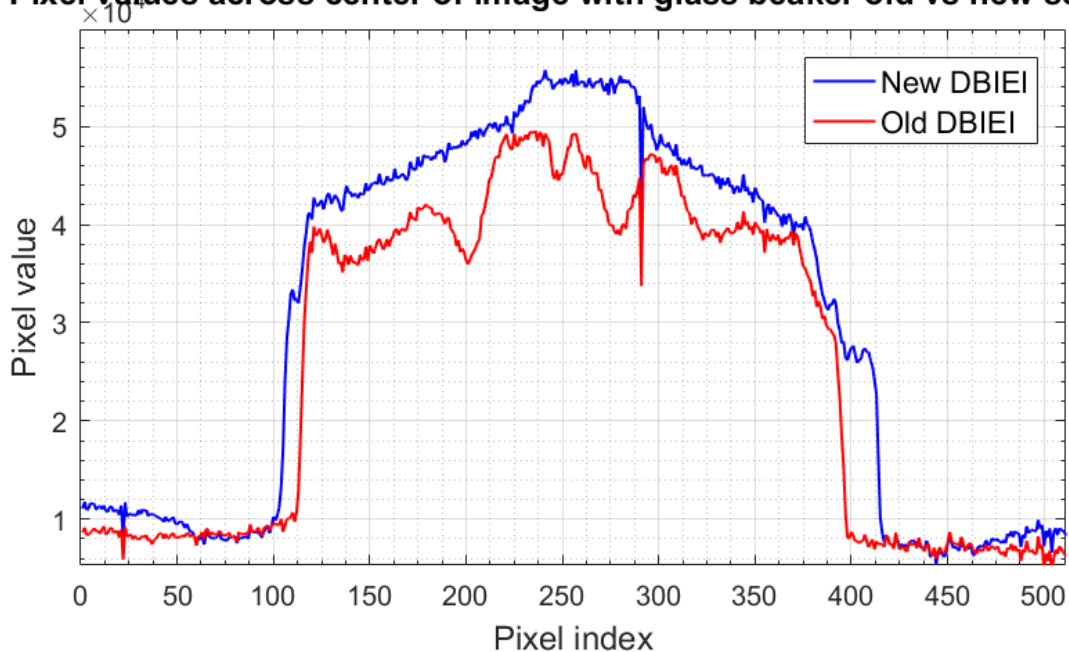


Figure 87 Pixel values for the old and new setup with glass beaker bottom in the combustion chamber

5.5.1 Discussion on Optical Configuration and Light Distortion

The new setup with the large engineered diffuser show a large improvement of reducing the potential for light distortion. Compared to the old setup with the engineering diffuser and the Fresnel lens. The old setup is mainly based on the article; “An optimized optical system for backlit imaging” by Gandhi and Heim [17], and a paper on soot quantification using a small diffuser and Fresnel lens “Quantification of Single-Hole Diesel Sprays by Means of Extinction Imaging” by Pastor et. al [40]. After revising the paper by Gandhi and Heim [17] with the knowledge that the new setup reduces light distortion, it is apparent that the optical configuration by Gandhi and Heim is primarily a method to optimize the back-light imaging mainly used for extinction imaging of the fuel sprays. It can also be used for soot detection but the price to pay for optimized light intensity is some light distortion.

In Gandhi and Heims optical configuration the objective of the engineering diffuser is to spread the collimated light source to cover the whole test section to achieve uniform background illumination. Then the Fresnel lense is used to capture the large light cone created by the diffuser and direct the light towards the test section. The implementation of a Fresnel lens reportedly reduced the requirements of the light source intensity by a large amount, as more light is directed toward the test section [17]. In redirecting the light, the Fresnel lens effectively collimates the incoming light. A ray diagram for a typical Fresnel lens is shown in Figure 88. From the ray diagram, it can be seen that a light source placed at the focal length of the lens will be at least partially collimated and redirected.

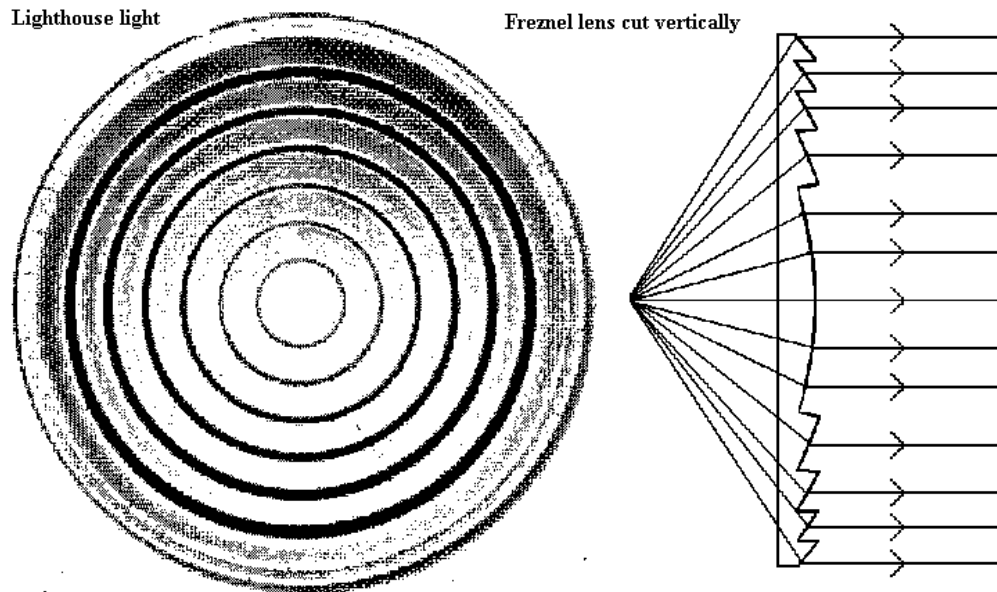


Figure 88 Ray diagram for a typical Fresnel lens.

5.5.2 Further Work

For further investigation of the optical setup a key factor will be to maximize the light intensity while maintain a uniform diffuse background light going through the test section. It is known from the initial test of the optical setup that obtaining sufficient background illumination with high frame rates is challenging. It is suggested that the new setup is tried without the small engineered diffusor and the Fresnel lens. This might increase the light intensity as more light is conserved toward the test section. However, it might also lead to the light from the LED being over expanded or too concentrated.

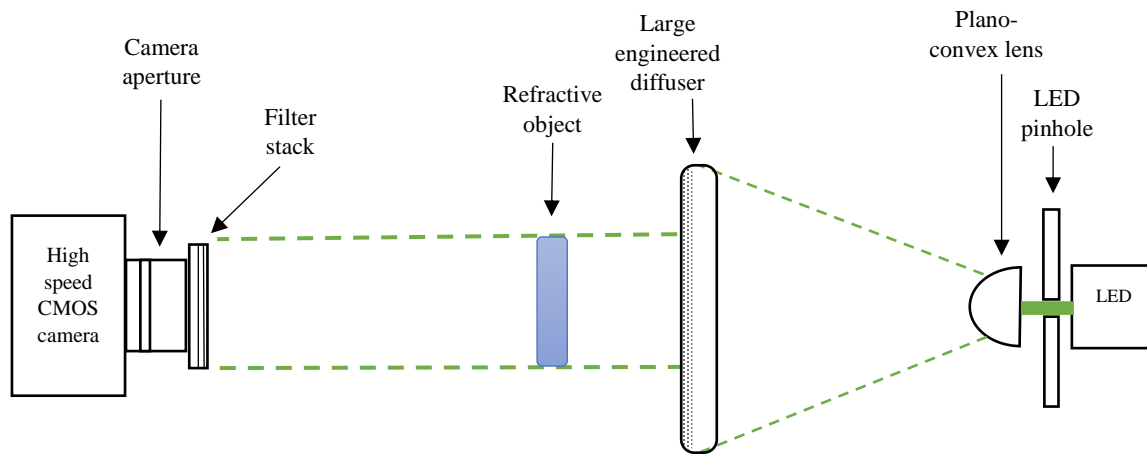


Figure 89 Suggested modification to the DBIEI setup.

Another lens configuration where the small engineered diffuser can be used is by mounting the diffuser between two aspheric condenser lenses. The suggested setup is seen in Figure 90. The figure is found in the application documentation of aspheric lenses by THORLABS [41]. This setup has the potential to achieve a uniform background illumination while reducing the loss of light.

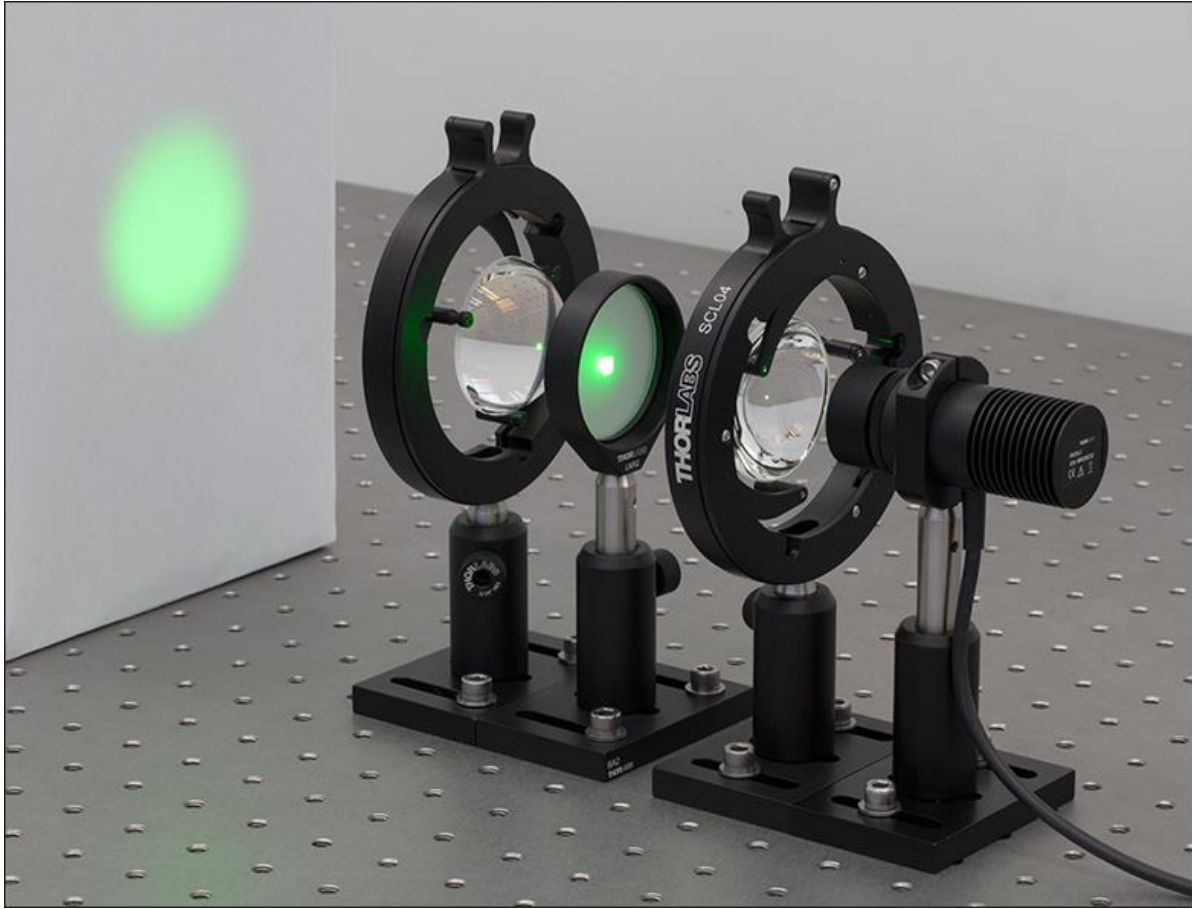


Figure 90 Suggested setup to obtain a diffuse background illumination. The image belongs to Thorlabs Inc, and is found in the documentation for application areas for aspheric condenser lenses [41].

Chapter 6 Summary and Conclusion of Experiments

The experiments in this thesis has added valuable information for further development of the optical engine. To summarize the findings of the experimental sections a short review of the results and conclusions is presented in this section. To remind the reader of the structure of the experimental sections in this thesis Figure 91 gives a visual representation.

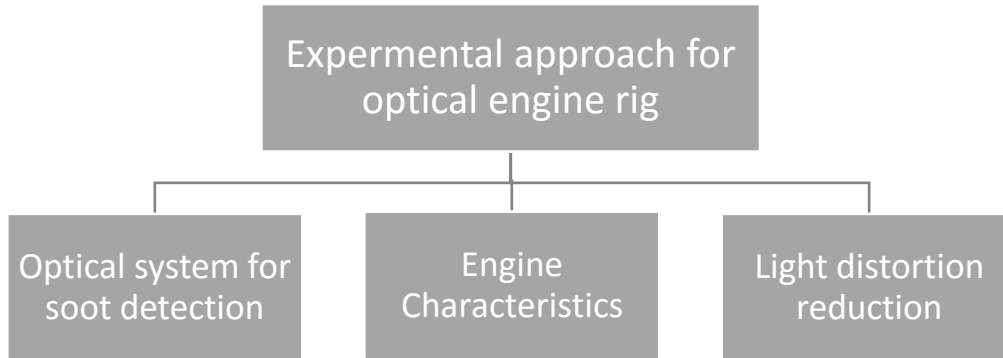


Figure 91 Overview of the three experimental section in this work

6.1 Optical System for Soot Detection

The optical system with the camera and LED used for back illumination is a complex system with many variables. To achieve the best results, it is concluded that the following settings and configurations are used.

- Filter out the first 200 images from each image series collected due to instability in LED.
- ND filters used at the current LED to be OD equal to 1 or below, preferably the lowest number OD number that sufficiently eliminates the flame luminosity.
- One microsecond camera exposure with 17,8 microsecond delay added to the LED trigger signal is suggested to obtain the best image quality.
- MATLAB script is developed to read and analyze the image sequences.

With the settings above the signal to noise ratio for an KL map is approximately 33.6 in an arbitrary soot rich propane flame. The soot rich region of the propane flame used yields a KL factor of 0.15000 ± 0.00617 at 2σ confidence interval. The relative uncertainty in the KL factor at two sigma confidence level is $\pm 4.1\%$. This value seems within a reasonable range. A 2013 study by Manin et al. [26] reported uncertainty in KL factor to be below 10% using a similar method.

6.2 Engine Characteristics

The engine characteristics tests led to various results. A MATLAB script was developed to present the average cylinder pressure in the most accurate way. The script can be found in the digital and printed appendix.

The passive thermal characteristics test showed that if the engine chamber to be heated to 200°C the heating blocks should be set to 231°C and the sleeve heater to 90°C, duty cycle/heat load for all element is recommended to 50% to avoid boiling of oil in the engine sleeve and chock heating of engine head. With these setting 90 minutes is needed to bring the chamber up to 200°C.

Passive cooling tests showed that the chamber cools with a rate of ~2.58°C per minute for the first 20 minutes from 200°C.

From active test with the engine running it is seen that the temperature of the engine increases with approximately 12°C per minute from ambient conditions with the air heater off, and at 14°C per minute with the air heater on. The running test also showed that caution must be applied while running the engine at longer duration when the chamber temperature reaches 115-120°C as the piston sleeve temperature climbs above its design point.

6.3 Light Distortion Experiments

The DBIEI setups show a large improvement over the IOBIEI setup to reduce the potential for light distortion. The IOBIEI setup can be used for soot detection but it is not optimized to reduce light distortion. For images of the injector sprays the IOBIEI is a good optical configuration as this was the original intent of use for this setup by Ghandhi and Heim [17]. Furthermore, suggestion on new optical configurations is given based on the experience from the light distortion experiments. An emphasis is put on conserving the light intensity available and have a sufficiently diffuse light passing through the test section.

Bibliography

- [1] J. E. Cohen, "Population growth and Earth's human carrying capacity," *Science*, pp. 341-346, 21 July 1995.
- [2] E. K. S. K. Kima Ki-Hyun, "A review on the human health impact of airborne particulate matter," *Environment International*, Volume 74, 1 February 2015.
- [3] B. T, D. S, F. D and F. P, "Bounding the role of black carbon in the climate system: a scientific assessment.," *Journal of Geophysical Research: Atmospheres*, p. 5380–5552, 6 June 2013.
- [4] H. Haslenda, N. Menaka, Y. Nor and S. Lim, "A cleaner and greener fuel: Biofuel blend formulation and emission assessment," *Journal of Cleaner Production*, p. TBA, 17 June 2016.
- [5] J. B. Heywood, *Internal Combustion Engine Fundamentals*, Boston: McGraw-Hill, 1988.
- [6] S. R. Turns, *An Introduction to Combustion Concepts and application*, New York: Mc Graw Hill, 2012.
- [7] K. I. S. Dale R. Treea, "Soot processes in compression ignition engines," *Progress in Energy and Combustion Science*, p. 272–309, June 2007.
- [8] A. H. G. M. T. K. M.Y. Choi, "Simultaneous optical measurement of soot volume fraction and temperature in premixed flames," *Combust Flame*, 99, p. pp. 174–186, 1994.
- [9] A. K. Agarwal, T. Gupta and A. Kothari, "Particulate emissions from biodiesel vs diesel fuelled compression ignition engine," *Renewable and Sustainable Energy Reviews*, pp. 3278-3300, 11 January 2011.
- [10] B. Haynes, "Soot Formation," *Prog Energy Combust Sci*, pp. 229-273, 1981.
- [11] A. S. (. W. Bartok, New York: Wiley, 1991.
- [12] Glassman, *Combustion*, San Diego: Academic Press, 1996.
- [13] Sandia Labs, "sandia.gov/about/," 2016. [Online]. Available: <http://www.sandia.gov/about/index.html>. [Accessed 8 10 2016].
- [14] L. M. Pickett, "Introducing the Engine Combustion Network," Sandia National Laboratories, 2008.

- [15] A. K. A. Yeshudas Jiotode, "In-cylinder combustion visualization of Jatropha straight vegetable oil and mineral diesel using high temperature industrial endoscopy for spatial temperature and soot distribution," *Fuel Processing Technology*, pp. 9-18, 1 12 2016.
- [16] N. L. H Zhao, "Optical diagnostics for soot and temperature measurement in diesel engines," *Progress in Energy and Combustion Science*, pp. 221-255, 1998.
- [17] J. B. Ghandhi and D. M. Heim, "An optimized optical system for backlit imaging," *Review of Scientific Instruments*, 2009.
- [18] S. A. Skeen, "A Progress Review on Soot Experiments and Modeling," SAE International, 2016.
- [19] D. L. Andrews, *Photonics, Volume 1: Fundamentals Of Photonics And Physics*, Wiley-Science, 2015.
- [20] G. Settles, *Schlieren And Shadowgraph Techniques*, New York: Springer, 2001.
- [21] J. Gronki and C. Schulz, "Multi-Species Laser-Based Imaging," SAE international, Warrendale, USA, 2004.
- [22] T. Kevin A and e. al., "Diffuse-light two-dimensional line-of-sight attenuation for soot concentration measurments," *APPLIED OPTICS*, FEB 2008.
- [23] M. Musculus and L. Pickett, "Diagnostic considerations for optical laser-extinction," *Combustion and Flame 141*, p. 371–391, 2 March 2005.
- [24] Lambda Research Corperation, "Lambdares.com: rayviz," 2017. [Online]. Available: <https://www.lambdares.com/rayviz/>. [Accessed 8 6 2017].
- [25] E. Hecht, *Optics*, 4th Edition, New York: Pearson , 2003.
- [26] L. M. P. a. S. A. S. Julien Manin, "Two-Color Diffused Back-Illumination Imaging as a Diagnostic," in *SAE/KSAE 2013 International Powertrains, Fuels & Lubricants Meeting*, USA, 2013.
- [27] M. Musculus and L. Pickett, "Diagnostic considerations for optical laser-extinction measurements of soot in high-pressure transient combustion environments," *Combustion and Flame 141*, pp. 371-391, 2 March 2005.
- [28] L. Pickett and D. Siebers, "Soot in diesel fuel jets: effects of ambient temperature, ambient density, and injection pressure," *Combustion and Flame, volume 138*, pp. 114-135, July 2004.
- [29] Photron INC, *FASTCAM SAI.1 Datasheet*, San Diego: Photron INC, 2014.

- [30] W. S, G. G, L. D, M. K and J. C, "Performance evaluation of an overdriven LED for high-speed schlieren imaging," The Visualization Society of Japan 2014, Japan, 2014.
- [31] A. Mazumdar, "PRINCIPLES AND TECHNIQUES OF SCHLIEREN IMAGING," Columbia University, New York, 2013.
- [32] Florida State Univeristy, ".fsu.edu/primer/digitalimaging/cmosimagesensors.html," 13 November 2015. [Online]. Available: <https://micro.magnet.fsu.edu/primer/digitalimaging/cmosimagesensors.html>. [Accessed 18 12 2016].
- [33] H. Titus, "Imaging Sensors," *Sensors*, February 2001.
- [34] A. Rose, "The Visual Process," in *Vision, Human and Electronic*, Springer, 1973, pp. 1-27.
- [35] A. Wheeler J and G. Ahmad R, "Introduction to Engineering Experimentation, Thrid Edition," San Fransisco, Pearson, 2009, pp. 128-186.
- [36] Richard T, Bernett. NASA , Fastner Design Manual, Cleveland, Ohio: NASA, 1990.
- [37] I. Balazs and J. R. Crookes, "Opto-mechanical design for sight windows under high loads," *Material and Design 117*, pp. 430-444, 2017.
- [38] H. G. TAYLOR and J. M. WALDRAM, "Improvements in the Schlieren method," *Journal of Scientific Instruments*, 1933.
- [39] RPC Photonics, Inc., "EDC-15-15132," Rochester NY, USA, 2017.
- [40] P. Jose V, G.-O. Jose M, R. Novella and T. Xuan, "Soot Quantification of Single-Hole Diesel Sprays by Means of Extinction Imaging," SAE International, Valencia, 2015.
- [41] Thorlabs, "Products Home / Optical Elements / Lenses / Aspheric Lenses: Molded & Precision Polished / Aspheric Condenser Lenses," 2017. [Online]. Available: https://www.thorlabs.com/newgrouppage9.cfm?objectgroup_id=3835. [Accessed 3 June 2017].
- [42] THORLABS, "Products Home / Optical Elements / Diffusers / Engineered Diffusers™," [Online]. Available: https://www.thorlabs.com/newgrouppage9.cfm?objectgroup_id=1660. [Accessed 9 June 2017].

Appendix A

Pressure Data Analysis Script

Input: Raw pressure data from chamber pressure.

Output: Average pressure and statistical analysis of pressure data.

Note: Before running this script, pressure data must be imported to the MATLAB workspace with a TDMS reader that is compliant with the current LabVIEW program used for data acquisition.

Structure input data and create a time vector equal to the # values pressure data

```
length=size(pressure,1);  
  
time_vector=(1:length);  
  
time_vector=time_vector(:);
```

polyfit is used to find the coefficients A and B for the falling average of the raw pressure plot, $Y=Ax+B$

```
p = polyfit(time_vector,pressure,1);  
  
% Extract variable A and B from polyfit function: Y=Ax+B  
A=p(1,1);  
B=p(1,2);
```

Offset each data value in pressure vector by A and B

```
for f = 1 : length;  
pressure_adjusted(f,1)=(pressure(f,1))+(-A*f)+(-B+0); %adjusts and equals ut slope  
of pressure data  
end
```

Finding peak value and index

```
[pks,locs]=  
findpeaks(smooth(pressure_adjusted),'MinPeakHeight',25,'MinPeakProminence',2);
```

Remove incomplete pressure curves

```
locs_to_remove = any(locs<5200, 2);
```

```
locs(locs_to_remove,:) = [];
pks(locs_to_remove,:) = [];
```

For 700RPM each pressure series is clipped at 10400 data points

```
nRows_pks = size(pks, 1);

nRows_pa = size(pressure_adjusted, 1);

samples_from_peak = 5200 ; %found from visual inspection of pressure plot, ensures some
overlap
sample_totsize = samples_from_peak*2;
p_accumulated= zeros(sample_totsize,nRows_pks);

top = zeros(nRows_pks,1);

low = zeros(nRows_pks,1);

high = zeros(nRows_pks,1);

for h= 1 : nRows_pks;
    top(h,1) = locs(h,1);
    low(h,1) = top(h,1) - samples_from_peak;
    high(h,1) = top(h,1) + samples_from_peak;
end
```

Remove last peak if vector is incomplete, incomplete vectors will lead to error in script

```
nRows_mod = nRows_pks-1;

for z=1:nRows_mod;
    for u = 1 : 10400 ;
        start=low(z,1)+u-1;
        p_accumulated(u,z) = pressure_adjusted(start,1);
    end
end
```

Remove zero columns

```
p_accumulated(:,all(p_accumulated==0))=[];
```

```
% Create average pressure plot
```

Offset each pressure plot from inlet valve closing = 1ATM

```
for a=1:260;
for b=1:nRows_mod;
p_accumulated_extracted_raw(a,b)=p_accumulated(2599+a,b);
end
end
```

Statistical analysis of pressure data

```
p_accumulated_offset_matrix=mean(p_accumulated_extracted_raw,1);%assigning ",1" takes
mean of each row
p_correction_matrix=(p_accumulated_offset_matrix)-1;
p_correction_matrix_pos=(p_correction_matrix)*-1;
p_size=size(p_accumulated,1);
```

Correction of pressure plot

```
for u=1:nRows_mod;
for s=1:p_size;
p_accumulated_mod(s,u) = (p_accumulated(s,u)) + (p_correction_matrix_pos(1,u));
end
end
```

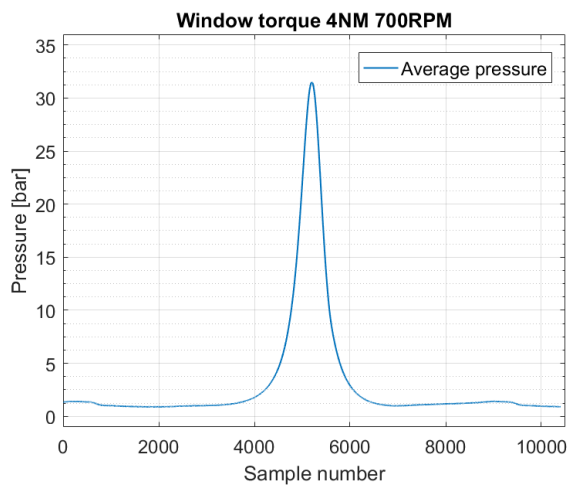
Average of corrected plot

```
p_avg = mean(p_accumulated_mod,2);
```

Plot

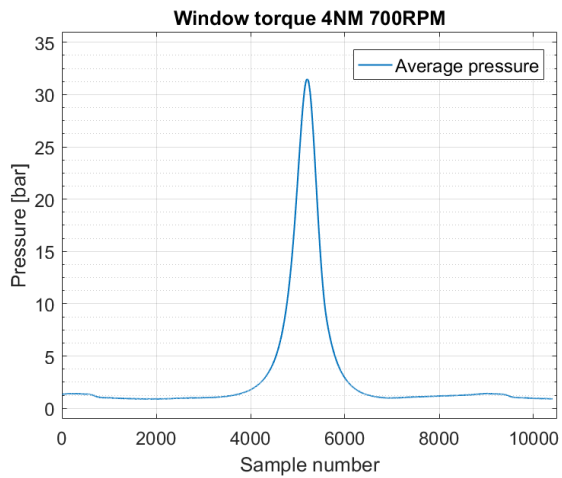
```
[pathstr,name,ext] = fileparts(fileName); %extract only filename
figure1 = figure;
axes1 = axes('Parent',figure1);
hold(axes1,'on');
plot(p_avg,'DisplayName','Average pressure','LineWidth',1);
xlabel('Sample number');
ylabel({'Pressure [bar]'});
title({name});
xlim(axes1,[0 10500]);
ylim(axes1,[-1 36]);
box(axes1,'on');
set(axes1,'FontSize',12,'XGrid','on','YGrid','on','YMinorGrid','on',...
'YMinorTick','on');
legend1 = legend(axes1,'show');
set(legend1,...
'Position',[0.669587071736655 0.825394039760783 0.130989583333333
0.0627962085308061],...
'FontSize',12);
```

```
y_max1 = max(p_avg);
```



Save Pressure plot fig

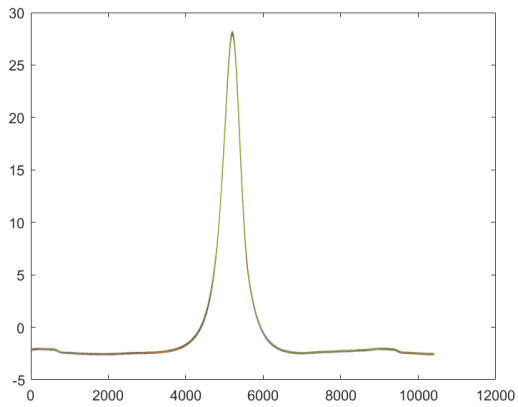
```
print('-f1', name, '-dpng');
```



```
figure(2)
```

```
title('p_accumulated')
```

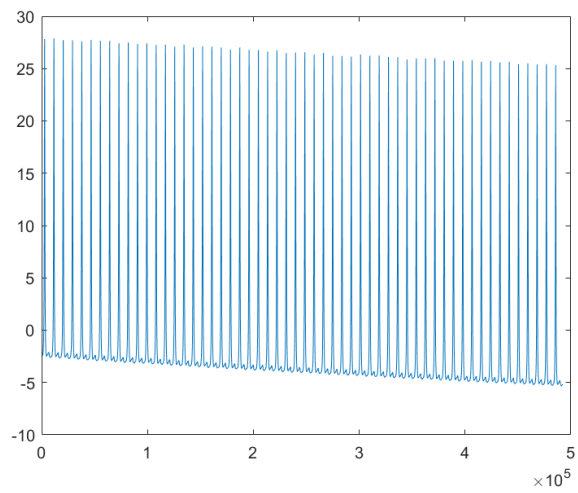
```
plot(p_accumulated)
```



```
figure(3)
```

```
title('Original pressure data')
```

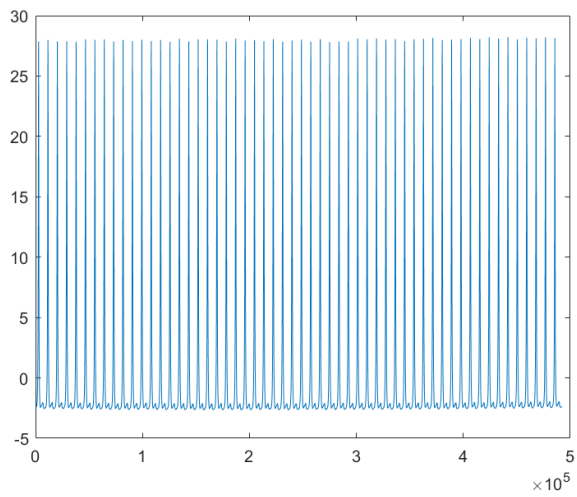
```
plot(pressure);
```



```
figure(4)
```

```
title('adjusted pressure data')
```

```
plot(pressure_adjusted)
```



```
% Statical analysis pressure data
standard_deviation = std(p_accumulated_mod,0,2);
variation = var(p_accumulated_mod,0,2);
```

Save p_avg plot and standard deviation

```
save(name, 'p_avg');
save(name, 'standard_deviation', '-append');
```

Published with MATLAB® R2016a

Soot quantification script

Input: TIFF images sequence from camera

Output: 2D KL map of the flame *SNR through sequence

Notes: Image sequence consist of a total of 1000 images, the first 500 images are recorded with only the background illumination present. From the first 500 images an initial unsteady section is filtered out and background illumination is established.

```
clear;close all;clc;
```

Input data, assign file path. An example TIFF sequence is used here

```
fname = 'C:\Users\mathi\OneDrive - NTNU\Data_prosjektoppgave\08_11_2016\02_KL_map  
images\flame_LED_explus_NDF2_f14_15V_Gate4_8V_flame_in_center.tif'
```

```
fname =C:\Users\mathi\OneDrive - NTNU\Data_prosjektoppgave\08_11_2016\02_KL_map  
images\flame_LED_explus_NDF2_f14_15V_Gate4_8V_flame_in_center.tif
```

Grab image info and number of pictures in TIFF series

```
info = imfinfo(fname);  
num_images = numel(info);
```

Number of elements to skip, due to unsteady LED illumination

```
num_im_skip = 200;
```

Statistical calculations for each frame.

```
num_sel_images = (num_images/2)-num_im_skip;  
frame0 = cell(1,num_sel_images); % initial image, no flame  
frame = cell(1,num_sel_images); % image with flame
```

For loop to read and convert images in TIFF sequence to the MATLAB workspace and store it as array of matrices.

```
for k = 1 : num_sel_images  
    [emp0,map] = imread(fname, k+num_im_skip);  
    [emp,map] = imread(fname,k+(num_images/2)+num_im_skip);  
    frame0{1,k} = double(emp0); %convert to double variable type in order to calculate  
average later  
    frame{1,k} = double(emp);  
  
    temp0 = frame0{1,k}; %Just used at the end of the script to illustrate on image  
    temp = frame{1,k};  
    uavg0(k) = mean(mean(frame0{1,k})); %Average value in each frame  
    uavg(k) = mean(mean(frame{1,k}));  
end
```

Further statistical analysis of frames

```

mean_uavg0 = mean(uavg0);
mean_uavg = mean(uavg);
std_uavg0 = std(uavg0);
std_uavg = std(uavg);
std_filter_limit = 5*std_uavg0;

```

Filter away images with extreme values based on high standard deviation

```

ind_filt = [];
for k = 1 : num_sel_images
    if (uavg0(k) > (mean_uavg0+std_filter_limit)) || (uavg0(k) < (mean_uavg0-
std_filter_limit))
        ind_filt = [ind_filt,k];
        frame0{1,k} = [];
    end
end

```

Summation of elements in matrix to find total intensity

```

sum_elements = zeros(256,256);
count = 0;
for i = 1:num_sel_images
    num_elements = sum(size(frame0{1,i}));
    if num_elements ~= 0
        temp = frame0{1,i};
        sum_elements = sum_elements + temp;
        count = count + 1;
    end
end
frame0_mean = sum_elements/count;
I0= frame0_mean ;

```

Filter out images that deviate more than std_filter_limit from the average intensity value.

```

ind_filt2 = [];
for k = 1 : num_sel_images
    if (uavg(k) > (mean_uavg+std_filter_limit)) || (uavg(k) < (mean_uavg-
std_filter_limit))
        ind_filt2 = [ind_filt2,k];
        frame{1,k} = [];
    end
end

```

Remove the cell array matrices that has been replaced with zero when filtered

```

count2 = 0;
for i = 1:num_sel_images
    num_elements = sum(size(frame{1,i}));
    if num_elements ~= 0
        temp = frame{1,i};
        %sum_elements = sum_elements + temp;
        count2 = count2 + 1;
    end
end

```

Pre-allocate

```

output_kl_image = cell(1,num_sel_images); %pre-allocate empty cell array for kl image
count3 = 0;

```

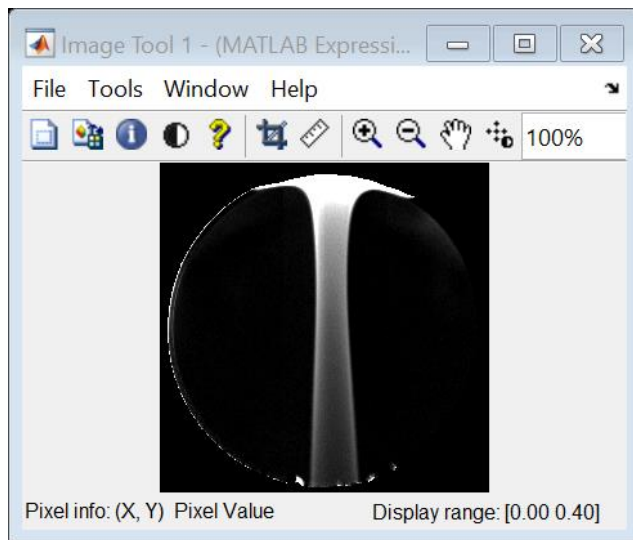
Create 2D KL map

```

for i = 1:num_sel_images
    num_elements2 = sum(size(frame{1,i}));
    if num_elements2 ~= 0
        output_kl_image{1,i} = I0 ./ frame{1,i} ;
        output_kl_image{1,i} = log(output_kl_image{1,i});
        output_kl_image{1,i}(isinf(output_kl_image{1,i})) = 0; %replace inf with 0
        output_kl_image{1,i}(isnan(output_kl_image{1,i})) = 0; %replace nan with 0 ;
        count3 = count3 + i;
    end
end
output_kl_image(:,ind_filt2)=[]; %remove empty columns

% %imadjust(output_kl_image{1,1});
% imwrite(output_kl_image{1,1},'KL_map_output.tif');
%
% for i = 2 : count3
%     %imadjust(output_kl_image{1,i});
%     imwrite(output_kl_image{1,i},'KL_map_output.tif','WriteMode','append')
% end
figure
imtool(output_kl_image{1,36},[0 0.4])
% colorbar
%-----
%create mean frame for soot sample. Do this to determinete soot impact on
%total signal

```



remove zero frames

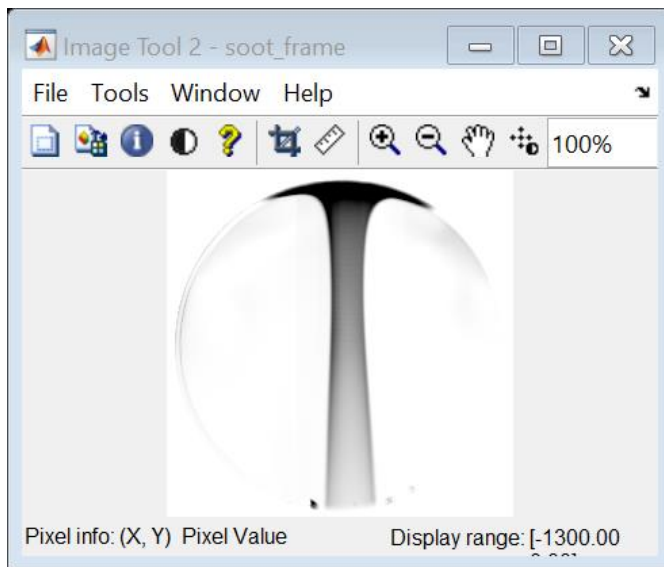
```
sum_elements_3 = zeros(256,256);  
count4 = 0;  
for i = 1:num_sel_images  
    num_elements_3 = sum(size(frame{1,i}));  
    if num_elements_3 ~= 0  
        temp = frame{1,i};  
        sum_elements_3 = sum_elements_3 + temp;  
        count4 = count4 + 1;  
    end  
end
```

Define new variables

```
frame_mean_flame = sum_elements_3/count4;  
I= frame_mean_flame ;  
soot_frame = (frame_mean_flame)-(frame0_mean) ; %take example frame to create soot for  
picture for illustration
```

Plot soot frame = (frame_mean_flame)-(frame0_mean)

```
figure  
imshow(soot_frame, [-1300 0]);
```

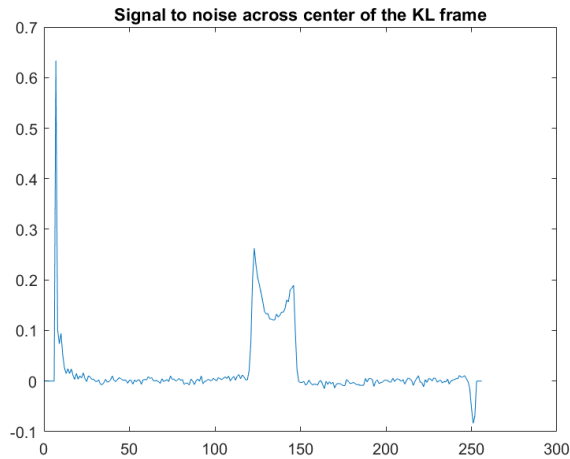


Extract one KL factor frame and define SNR

```
random_kl_frame = (output_kl_image{1,36}) ;  
SNR_across_center_random_kl_frame = random_kl_frame(128,:);
```

Plot SNR

```
figure  
plot(SNR_across_center_random_kl_frame);  
title('Signal to noise across center of the KL frame');
```



Find average value standard deviation in background

```
SNR_background_kl_image = SNR_across_center_random_kl_frame(20:115);
avg_snr_bg_kl_image= mean(SNR_background_kl_image);
std_SNR_bg_kl_image= std(SNR_background_kl_image);
% Noise in the flame/soot region should be the same as in the background region
```

Soot signal impact on KL image presented as SNR_relative

```
SNR_flame_kl_image = SNR_across_center_random_kl_frame(122:147);
avg_SNR_flame_kl_image = mean(SNR_flame_kl_image);
SNR_relative=(abs(avg_SNR_flame_kl_image) / abs(std_SNR_bg_kl_image))
```

SNR_relative = 33.5575

Published with MATLAB® R2016a

Appendix B

HSE Report